DISS. ETH NO. 26988

ACOUSTIC DAMPING AND AEROACOUSTIC INSTABILITIES OF CAVITIES SUBJECT TO BIAS AND GRAZING FLOWS

A thesis submitted to attain the degree of
DOCTOR OF SCIENCES of ETH ZÜRICH
(Dr. Sc. ETH Zürich)

presented by
CLAIRE BOURQUARD

Dipl. Ing. SUPAERO, Institut Supérieur de l'Aéronautique et de l'Espace, Toulouse

born on 01.01.1991
citizen of France

accepted on the recommendation of

Prof. Dr. Nicolas Noiray
Prof. Dr. Aimee Morgans
Prof. Dr. Avraham Hirschberg

2021

Abstract

Thermo- and aeroacoustic instabilities are a critical issue in industry and air transportation. These instabilities can pose a threat to the mechanical integrity of the system in which they occur, with catastrophic consequences. In addition, aeroacoustic instabilities also contributes to environmental noise pollution with adverse effects on human and wildlife health. Thermoacoustic instabilities can occur in heavy-duty gas turbines or aero-engines, when an unsteady flame constructively interacts with an acoustic mode of the combustion chamber. They can be prevented by putting additional acoustic cavities, so-called *dampers*, along the chamber walls. The dampers are usually cooled by a purge flow passing through the damper, called *bias* flow. Aeroacoustic instabilities can occur in any system where, in a pipe traversed by flow, an unsteady shear layer can couple to an acoustic resonator, whether it is a side-branch cavity (in this case, the flow is called *grazing* flow), or an abrupt area change over a section of the pipe in the case of *bias flow*. Under particular circumstances, the shear layer starts amplifying pressure disturbances. If this happens close to the frequency of one of the acoustic resonator modes, self-sustained acoustic oscillations can occur.

In the present work, these complex phenomena are modelled and analysed accurately using the approximate description as systems of coupled harmonic oscillators. In a first part, this modelling approach is applied to the stabilization of an unstable acoustic mode by an acoustic damper. The main dissipation mechanism of the dampers is vortex shedding, occuring periodically at the damper exit. It can be adjusted by adjusting the mean flow purging the dampers (*bias* flow). The modelling of two different types of dampers as damped harmonic oscillators is derived and confirmed experimentally. This model is then coupled to another linearly unstable oscillator representing the instability. The stability analysis of the system is performed, and confirmed experimentally against a chamber with an electro-acoustic feedback loop mimicking a thermoacoustic instability. The best stabilization is shown to occur at the exceptional point of the system.

In the next part the effects of the damper nonlinearity on the limit cycles of the coupled system are investigated. Indeed, in case of very high amplitude in the chamber, the mean flow through a Helmholtz damper can reverse during part of the cycle and produce vortex shedding on the other side of the neck. This is accounted for using a nonlinearity

in the form of an absolute value term. The slow-flow amplitude equations of the system are derived in order to determine the limit cycles and bifurcation diagram of the system. It is shown that the damper nonlinearity induces hysteretic behaviour, which is also demonstrated experimentally on the previous chamber-damper system.

The last part of the thesis deals with the application of the coupled oscillators system to aeroacoustic instabilities, applied on the canonical setup of a rectangular deep cavity attached to a square channel with mean flow (*grazing* flow). The frequency-dependent acoustic response of both the cavity and the shear layer developing at the junction are measured, and fitted using 2nd order transfer functions. The amplitude dependence of the shear layer's acoustic response is also measured. This allows for the analysis of the system linear stability as well as the derivation of a nonlinear system of coupled oscillators. This model can be used for studying the limit cycles of the system using the slow-flow amplitude equations once again. Addition of both multiplicative coloured noise and additive white noise to the model allows for the reproduction of the experimentally-observed intermittency of the instability. In a last part, the influence of the multiplicative coloured noise is studied on a simpler system, the Van der Pol oscillator, in order to derive criteria for the occurrence of intermittency.

Overall, the coupled oscillators approach is successfully applied to two types of problems, namely the deep cavity – shear layer aeroacoustic instability, and the stabilization of an unstable acoustic mode by acoustic dampers. The results of the model, whether in terms of stability, oscillation amplitude, bifurcation diagram and influence of noise, are validated against experiments. The modelling approach, although based on an approximate solution, allows for the reproduction of peculiar dynamical phenomena of the real systems.

Résumé

Les instabilités thermoacoustiques et aéroacoustiques sont un problème d'une importance cruciale dans l'industrie et le transport aérien. Ces instabilités peuvent menacer l'intégrité mécanique du système dans lequel elles se produisent, avec des conséquences catastrophiques. De plus, les instabilités aéroacoustiques contribuent également à la pollution sonore environnementale avec des effets néfastes sur la santé humaine et animale. Les instabilités thermoacoustiques peuvent se produire dans les turbines à gaz de grande puissance ou les moteurs d'avion, lorsqu'une flamme instable interagit de manière constructive avec un mode acoustique de la chambre de combustion. Ils peuvent être évités en installant des cavités acoustiques supplémentaires, appelées amortisseurs acoustiques, le long des parois de la chambre. Ceux-ci sont généralement refroidis par un flux de purge traversant, appelé *flux de biais*. Les instabilités aéroacoustiques, quant à elles, peuvent se produire dans tout système où, dans un conduit traversé par un écoulement, une couche de cisaillement instationnaire peut se coupler à un résonateur acoustique, qu'il s'agisse d'une cavité de branche latérale (dans ce cas, l'écoulement est appelé écoulement rasant), ou un changement brusque de zone sur une section du tuyau en cas de flux de biais. Dans des circonstances particulières, la couche de cisaillement commence à amplifier les perturbations de pression. Si cela se produit près de la fréquence de l'un des modes du résonateur acoustique, des oscillations acoustiques auto-entretenues peuvent se produire.

Dans la présente thèse, ces phénomènes complexes sont modélisés et analysés en détail en utilisant la description approximative d'un système d'oscillateurs harmoniques couplés. Dans une première partie, cette approche de modélisation est appliquée à la stabilisation d'un mode acoustique instable par un amortisseur acoustique. Le principal mécanisme de dissipation des amortisseurs est le détachement de tourbillons, qui se produit périodiquement à la sortie de l'amortisseur. La dissipation peut être ajustée en ajustant le flux de purge des amortisseurs (flux de biais). La modélisation de deux différents types d'amortisseurs en tant qu'oscillateurs harmoniques amortis est dérivée et confirmée expérimentalement. Ce modèle est ensuite couplé à un autre oscillateur linéairement instable représentant l'instabilité. L'analyse de stabilité du système est effectuée et confirmée expérimentalement à l'aide une chambre avec une boucle de rétroaction électro-acoustique imitant une instabilité thermoacoustique. Il est démontré que la meilleure stabilisation du mode se produit au point exceptionnel du système.

Dans la partie suivante, les effets de la non-linéarité de l'amortisseur sur les cycles limites du système couplé sont étudiés. En effet, en cas d'amplitude très élevée dans la chambre, la vitesse moyenne dans le col d'un amortisseur acoustique de type Helmholtz peut s'inverser pendant une partie du cycle et produire le détachement de tourbillons du côté intérieur du col. Ceci est pris en compte en utilisant une non-linéarité sous la forme d'un terme de valeur absolue. Les équations d'amplitude du système sont dérivées afin de déterminer les cycles limites et le diagramme de bifurcation du système. Il est démontré que la non-linéarité de l'amortisseur induit un comportement hystérétique, ce qui est également démontré expérimentalement grâce au système chambre-amortisseur du chapitre précédent.

La dernière partie de la thèse traite de l'application du système d'oscillateurs couplés aux instabilités aéroacoustiques, appliqué sur la configuration canonique d'une cavité profonde rectangulaire attachée à un canal de section carrée traversé par un écoulement moyen (écoulement rasant). Les réponses acoustiques respectives de la cavité et de la couche de cisaillement se développant à la jonction, dépendantes de la fréquence, sont mesurées et ajustées à l'aide de fonctions de transfert du second ordre. La dépendance en amplitude de la réponse acoustique de la couche de cisaillement est également mesurée. Ceci permet l'analyse de la stabilité linéaire du système ainsi que la dérivation d'un système non-linéaire d'oscillateurs couplés. Ce modèle peut être utilisé pour étudier les cycles limites du système en dérivant à nouveau les équations d'amplitude. L'ajout à la fois de bruit coloré multiplicatif et de bruit blanc additif permet de reproduire l'intermittence de l'instabilité observée expérimentalement. Dans une dernière partie, l'influence du bruit multiplicatif coloré est étudiée sur un système plus simple, l'oscillateur Van der Pol, afin de dériver des critères d'occurrence de l'intermittence.

En conclusion, l'approche des oscillateurs couplés est appliquée avec succès à deux types de problèmes, à savoir l'instabilité aéroacoustique cavité profonde - couche de cisaillement et la stabilisation d'un mode acoustique instable par des amortisseurs acoustiques. Les résultats du modèle, que ce soit en termes de stabilité, d'amplitude d'oscillation, de diagramme de bifurcation et d'influence de bruit, sont validés grâce aux expériences. L'approche de modélisation, bien que basée sur une solution approximative, permet la reproduction de phénomènes dynamiques particuliers observés sur les systèmes réels.

Contents

III

Nomenclature

Latin Symbols

a	HH neck cross-section
A	amplitude of p, amplitude of η
$\mathcal{A}$	specific admittance
$A_{H,Q}$	HH volume and QW cross sectional area
B	amplitude of u
c	speed of sound
c_1	linear gain applied to the voltage signal
c_2	cubic saturation coefficient of the voltage signal
d	damping from fit on shear layer specific impedance
d_1	y-intercept of amplitude dependant dW/U
d_2	linear amplitude dependance of dW/U
D	characteristic polynomial of the coupled system
$e_{1,2}$	eigenvectors of the coupled system
f	frequency, forward-travelling Riemann invariant
g	backward-travelling Riemann invariant
g_Q	approximation function for cotangent around $\pi/2$
g_H	vortex shedding nonlinearity function
H	deep cavity height
$\mathcal{H}$	transfer function
K_Q	acoustic stiffness of the QW
K_{ac}	acoustic stiffness of air column under bulk compression
L	deep cavity / QW length
$\mathcal{L}_{\mathrm{bl}}$	acoustic power loss per unit area in the acoustic boundary layer
$\mathcal{L}_{\mathrm{bl,t}}$	total power loss in the acoustic boundary layer
m	dissipative coupling from fit on shear layer specific impedance
m_1	y-intercept of amplitude dependant mWM^3/c
m_3	linear amplitude dependance of mWM^3/c
$\dot{m}$	air mass flow to purge the damper
$\dot{m}_{0,H/Q}$	purge mass flow for which $\mathcal{R}=0$
M	Mach number U/c
n	gain from fit on shear layer specific impedance / source term gain
n_0	normalized constant n/M^2

p	acoustic pressure
$\bar{p}$	ambient pressure
$\mathcal{P}$	probability density function
Pr	Prandtl number
Q	heat release
$Q_{C,N}$	coherent/noisy component of the heat release (acoustic source)
$\mathcal{Q}_N$	normalized noisy component of the acoustic source
r	QW radius
R	Resistance
$\mathcal{R}$	reflection coefficient
Re	Reynolds number
s	Laplace variable
S_d	area of the chamber covered with dampers
S_{IT}	cross sectional area of the impedance tube
S_{xy}	Cross-power spectral density of x and y
$S(x)$	Saturation function
St	Strouhal number
T	oscillation period
$\mathcal{T}$	transmission coefficient
u	acoustic velocity
$\bar{u}$	purge flow velocity through the damper opening
U	mean velocity in the channel
U_f	voltage signal from the feedback microphone
V	volume of the chamber
V_H	back volume of the HH
V_Q	volume of the QW
$\boldsymbol{v}$	velocity field
W	width of the deep cavity
$\boldsymbol{x}_d$	position vector of the damper
Z	impedance
$\mathcal{Z}$	specific impedance

Greek Symbols

α	acoustic linear damping
β	hydrodynamic damping, linear gain of the electro-acoustic feedback loop
β_1	linear hydrodynamic damping term
β_2	quadratic hydrodynamic damping term
γ	acoustic dissipative coupling, heat capacity ratio
Γ_x	factor adjusting the intensity of noise x
δ	detuning: $\delta = (\omega_{H,Q} - \omega_0)/\omega_0$, Dirac distribution
δ_{bl}	acoustic boundary layer thickness ($\delta_{\mathrm{bl}} = \sqrt{2\nu/\omega}$)
$\Delta\omega$	angular frequency difference
ϵ	adimensionnal frequency ramp rate
ϵ_r	dimensionnal frequency ramp rate
ε	area ratio between the deep cavity and its opening
$\varepsilon_{H,Q}$	damping efficiency factor
$\zeta_{H,Q}$	HH or QW pressure drop coefficient
ζ_x	noise forcing on the diff. eq. for variable x
η	pressure dominant mode amplitude, variable of the Van der Pol oscillator
κ	cubic saturation term
λ	eigenvalues of the coupled system
Λ	norm of the dominant acoustic mode
μ	hydrodynamic dissipative coupling
μ_1	linear hydrod. dissipative coupling term
μ_3	cubic hydrod. dissipative coupling term
ν	linear growth rate, kinematic viscosity
ξ	additive white noise
ρ	air density
σ	hydrodynamic reactive coupling
$\sigma_{H,Q}$	porosity ($\sigma_H = a/S_{\mathrm{IT}}$ and $\sigma_Q = A_Q/S_{\mathrm{IT}}$)
σ_x	variance of the variable x
τ	time delay of the source term
τ_χ	multiplicative noise correlation time
φ	phase drift
ϕ	phase difference between p and u : $\phi = \varphi_A - \varphi_B$
χ	multiplicative colored noise
ψ	spatial distribution of the dominant acoustic mode
ψ_d	weighting coefficient (position of damper w.r.t. the mode shape)
Ψ_d	coefficient describing number and location of dampers with respect to mode shape
ω	angular frequency
$\boldsymbol{\omega}$	vorticity field

Superscripts and operators

$\hat{(\cdot)}$	Fourier transform
$\overline{(\cdot)}$	time averaged mean value
$(\cdot)'$	fluctuation around the mean value
$\tilde{(\cdot)}$	zero-mean coherent component
$\langle \cdot \rangle$	phase-averaged component
$\check{(\cdot)}$	zero-mean turbulent component

Subscripts

0	dominant acoustic mode
a	acoustic (deep cavity)
bl	boundary layer
BS	best stabilization
c	chamber
cor	end correction
d	damper
EP	exceptional point
H	Helmholtz damper
l	left shear layer frequency
m	maximum (or with maximum real part)
NL	nonlinear
p	physical (length)
Q	Quarter-wave damper
r	right shear layer frequency
vs	vortex shedding
wd	"with damper", i.e. of the chamber-damper coupled system

Abbreviations

HH	**H**elm**H**oltz damper
MFM	**M**ass **F**low **M**eter
MMM	**M**ulti-**M**icrophone **M**ethod
ODE	**O**rdinary **D**ifferential **E**quation
PDF	**P**roability **D**ensity **F**unction
QW	**Q**uarter-**W**ave damper

RMS	**R**oot **M**ean **S**quare	$\mathrm{RMS}(s) = \sqrt{\dfrac{1}{n}\sum_n |s|^2}$

Chapter 1

Introduction

1.1 Motivation

Noise pollution is considered one of the main three environmental pollution that has adverse effects on human health [31], along with air pollution and toxic chemical exposure. The main culprits are road traffic, railways, air traffic and industry [31]. Even at levels where the human auditory system is not at risk, noise pollution is the source of numerous health issues [173], among which the release of stress hormones [31, 170], sleep disturbances [142], hypertension and heart diseases [67]. The animal kingdom is far from spared, with wildlife highly impacted by anthropogenic noise pollution [89] and suffering similar health issues to those experienced by humans. As such, managing the impact of anthropogenic noise is a critical component of maintaining both healthy ecosystems and a healthy population.

Noise in itself, if within a reasonable level, is not necessarily harmful: low-level white noise exposition has proven to have positive effects on concentration [144, 171] and agitation-soothing properties [26]. The issue in noise pollution is rather that of tonal noise with very narrow frequency content as opposed to broadband noise [139]. Although the "annoyance level" seems to be higher for high frequency noise, compared to low frequency noise, within the human hearing range for similar sound pressure level [12], low-frequency noise represents a higher threat since humans seem to be particularly sensitive to it [9]. In addition, low-frequency noise is by definition particularly difficult to contain and reduce due to the extent of the corresponding wavelength.

From a modelling perspective, tonal noise has the advantage that it arises from systems which exhibit strong response at specific frequencies, i.e. systems that feature separated acoustic modes. In this case, the acoustic field is a superposition of contributions of all modes of the system. Under the assumption that the modes are sufficiently spaced and only one of them drives a high amplitude tonal response, the system response can be modelled using the contribution of that mode only [122], and the mode amplitude

can be modelled using a harmonic oscillator equation, with the potential damping and nonlinearities depending on the specificities of the system.

From a system stability point of view, the high-amplitude tonal noise dynamics can be further divided between acoustic *resonance*, and *instability*, the latter usually involving acoustics coupled to a source term. Both of these instances can not only be the source of noise pollution, but also put the mechanical integrity of the system at risk. A zoology of the different cases for flow-induced vibrations has been performed by Naudascher & Rockwell [125]. Acoustic *resonance* corresponds to a linearly stable system (i.e. a system that, if not excited, would experience exponential decay and converge to noise level zero) excited by a source, whether coming from vibrations or from background noise. In that case, the system, which can be modelled by a lightly-damped harmonic oscillator, experiences *resonance* if the frequency of the excitation is close to the natural frequency of the oscillator, and is thus able to reach very high pressure amplitudes. Those pressure amplitudes can also be reached by a different type of system dynamics, namely an *instability*. In that case, the acoustic system itself still is linearly stable, but is coupled to an active element that can render the full system linearly unstable under certain conditions. Under those conditions, the system experiences exponential growth of pressure amplitude until it stabilizes on a high-amplitude limit cycle due to nonlinearities. There are various examples of this phenomenon, for example thermoacoustic instabilities (where the active element is an unsteady flame), or aeroacoustic instabilities (where the active element is an unsteady shear layer), which are both the focus of this thesis.

Thermoacoustic instabilities are a well-known phenomena that is triggered when constructive feedback is achieved between an unsteady flame and the acoustic field in an enclosed environment (the combustion chamber for instance, which can be modelled as an acoustic resonator). The condition for instability has been established as early as the XIXth century by Lord Rayleigh [145], who noticed a tonal noise was produced by a flame enclosed in a glass tube under the following condition:

$$\oint p'Q'dt > 0 \tag{1.1}$$

This equation, called the *Rayleigh criterion*, can be interpreted as follows: if the pressure fluctuation p' is in phase with the unsteady heat release Q' from the flame, local amplification of disturbances occurs [114]. If the spatial integration of this quantity over the domain is also positive, an unstable feedback loop is created. This leads to high pressure oscillation levels which, in the case of a small flame in a glass tube can be considered an entertaining amusement, however, in the cases of high-power flames, can lead to extreme damage to the system. For this reason, thermo-acoustic instabilities has been the topic of numerous investigation for the safe design of rocket engines [68] and gas turbines [46,104], either aero-engines or land-based for electricity production. A counter-measure to avoid thermoacoustic instabilities is adding some damping to the system, for example by adding passive damping devices [202] such as Helmholtz

resonators [8, 17, 47], usually crossed by a purging mean flow (*bias* flow).

The second type of instability that will be the focus of this thesis is the aeroacoustic instability. The classical setup is the following: a cavity (i.e. acoustic resonator) is mounted perpendicularly to a channel through which there is a constant mean flow (*grazing* flow). An unsteady shear layer develops at the junction between the channel and the resonator. In a similar manner to the thermoacoustic instability, the aeroacoustic instability arises when constructive feedback is achieved between the unsteady shear layer and the acoustic field inside the cavity. Once again, the condition for instability stems from a closed integral from Howe's energy corollary [73]:

$$- \oint \bar{\rho}(\boldsymbol{\omega} \times \boldsymbol{v}) \cdot u'dt > 0, \tag{1.2}$$

with $\bar{\rho}$ the mean air density, $\boldsymbol{\omega}$ the local vorticity, $\boldsymbol{v}$ the local velocity and u' the acoustic velocity, all of those quantities being evaluated close to the junction where the shear layer develops. If this projection of the Lamb vector over the acoustic field is positive over one cycle, acoustic energy is locally produced [73]. If the spatial integration over the domain (around the unsteady shear layer) is positive, the unstable feedback loop is achieved [21]. Aeroacoustic instability has been at the root of numerous issues in industry, ranging from unwanted vibrations to acoustic fatigue failure. Practical examples include slotted-wall tunnels for train transport [91], annular gas seals for compressors and turbines [107], metal bellows [189], or steam dryer of a boiling water reactor [206]. For this reason, the phenomenon of aeroacoustic instability has been the subject of multiple studies since more than 60 years, beginning with wind tunnel experiments [49, 94] and first empirical models [11, 152, 180]. Different measures to counter-act the generation mechanism of disturbances have been studied [154], including numerical simulations on the influence of the cavity edge geometry [42] or addition of spoilers [166]. This remains however a challenging task, since the full description of the different parameters' influence on the aeroacoustic resonance mechanism is still lacking.

The present thesis uses the approximate harmonic oscillator solution in order to describe both the influence of acoustic dampers on the stability and limit cycles of a mimicked unstable thermoacoustic mode, and the aeroacoustic instability in a rectangular T-junction. The aim is to provide an accurate description of the system dynamics without trying to model the actual flow physics or the shear layer oscillations in detail. The frame of the modelling used throughout the thesis and its justification is detailed below.

1.2   Coupled oscillators modelling

This section details the principle of the modelling used throughout the thesis, starting from the acoustic resonator, which is the "base block" of our modelling approach, then moving on to the different possible handling of the source term. The origin of the nonlinearities and the influence of noise are also introduced in this section.

1.2.1 Acoustic resonator

As was mentioned in section 1.1, the acoustic systems considered in this thesis are those that exhibit strong frequency response at specific frequencies, meaning their acoustic field is a superposition of contributions of all modes of the system, and the acoustic variable (usually the pressure) can be projected on an orthogonal basis $\mathbf{\Psi}$ using the Galerkin expansion [117]:

$$p(t, \mathbf{x}) = \sum_{i=1}^{\infty} \eta_i(t)\psi_i(\mathbf{x}), \tag{1.3}$$

with $\psi_i(\mathbf{x})$ the spatial distribution of the natural eigenmodes and $\eta_i(t)$ their time-dependent amplitude. If a certain mode j is dominates the acoustic response in a certain frequency range, one can approximate the pressure field with $p(t, \mathbf{x}) = \eta_j(t)\psi_j(\mathbf{x})$. The dominant mode amplitude $\eta_j(t)$, simplified as $\eta(t)$, can be modelled using a harmonic oscillator equation:

$$\ddot{\eta} + 2\alpha\dot{\eta} + \omega_0^2\eta = F(t), \tag{1.4}$$

With α the damping of the system (which is always positive if there are only acoustics involved), ω_0 the natural frequency of the dominant mode, and $F(t)$ a forcing, which can be either noise or a source-term as will be detailed in the next section. The damping α can be a combination of damping from different sources, the main one being thermo-viscous dissipation in the acoustic boundary layers at the boundaries of the system. The boundary layers are formed when the fluid oscillates back and forth close to the system boundaries due to the pressure oscillation. However, in the case of acoustic resonators used as *dampers* in the attempt of stabilizing thermoacoustic instabilities, the resonators are often purged with a mean flow (known as *bias* flow) in order to cool them, but also to enhance the damping.

It is important to note that in specific cases the periodic vortex shedding caused by the bias flow can lead to sound production [177, 193, 195]. Within the scope of this thesis, however, only cases where the bias flow induces additional damping will be investigated. Indeed, in that case, the damping term from the periodic vortex shedding at the end of the damper mouth is proportional to the mean velocity $\bar{u}$ via the *pressure loss coefficient* $\zeta_{H,Q}$. This coefficient incorporates effects due to the geometry of the damper and to the flow conditions at the damper opening [8, 122]. In this case the principal dissipation mechanism contributing to the damping α is the vortex shedding, and in some cases the visco-thermal losses in the acoustic boundary layers can even be neglected [181].

In the remainder of the thesis, the acoustic resonator equation which does *not* incorporate the source term will be expressed with the acoustic velocity as a variable, and a pressure oscillation as forcing. This will represent our fundamental building block, although it will always be displayed as the second equation in the coupled systems of chapters 2, 3 and 4, for the simple reason that the acoustic velocity cannot be directly compared to the experiments: only the acoustic pressure can be easily experimentally measured with microphones.

1.2.2 Instability modelling

After having established the basis for the modelling of the acoustic resonator, this section deals with the modelling of the instability, and on how to incorporate the effect of the source term in simple harmonic oscillator equations. For systems experiencing thermoacoustic instabilities, the acoustic pressure field, including source term coming from the flame heat release, can be expressed by the Helmholtz equation in frequency domain:

$$
\begin{cases}
\nabla^2 \hat{p}(s,\mathbf{x})) - \left(\dfrac{s}{c}\right)^2 \hat{p}(s,\mathbf{x})) = -s\dfrac{(\gamma-1)}{c^2}\hat{Q}(s,\mathbf{x})) & \text{in the domain,} \\[2mm]
\dfrac{\hat{p}(s,\mathbf{x}))}{\hat{u}(s,\mathbf{x})) \cdot \mathbf{n}} = Z(s,\mathbf{x})) & \text{on boundaries,}
\end{cases}
\tag{1.5}
$$

where $\hat{p}$ and $\hat{u}$ are the pressure and velocity fields in the frequency domain, s is the Laplace variable, c is the speed of sound, γ the specific heat ratio, $\hat{Q}$ the heat release, $\mathbf{n}$ the normal going *out* of the boundary and Z the acoustic impedance. As mentioned in the previous section, in case of a dominant mode the pressure field can be approximated by $p(t,\mathbf{x}) = \eta(t)\psi(\mathbf{x})$, with ψ the mode shape and η the mode amplitude, which can be determined by projecting Eq. (1.5) on ψ:

$$
\hat{\eta}(s) = \frac{s\rho c^2}{s^2 + \omega_0^2}\frac{1}{V\Lambda}\left(\frac{\gamma-1}{\rho c^2}\int_V \hat{Q}\psi^*(\mathbf{x})dV - \int_S \hat{\eta}(s)\frac{|\psi(\mathbf{x})|^2}{Z(\mathbf{x},s)}dS\right).
\tag{1.6}
$$

The second integral in Eq. (1.6) corresponds to the energy flux through the boundaries and can be modelled by a damping term $2\alpha s\hat{\eta}$, with $\alpha > 0$ the natural linear damping of the cavity coming from the visco-thermal losses in the acoustic boundary layers, as was explained in the previous section. The first integral, incorporating the source term, can be modelled by $ne^{-i\omega_0\tau}s\hat{\eta}$ using the sensitive time lag, or $(n-\tau)$ formulation used in [35, 114]. This model, based on a gain (or interaction index) and a time delay (or phase) of the flame heat release response to acoustic velocity, incorporates in a simple form multiple sources of interaction between the acoustic field and the flame, including interaction with the boundaries and flame-vortex interactions [46, 114]. Some studies based on an acoustic field coupled to the $(n-\tau)$ modelled source term even highlight intrinsic combustion instabilities [51, 115, 123], which are not covered in this thesis. The determination of the frequency-dependent n and τ has been tackled in numerous studies. This frequency dependent flame response, is called *flame transfer function* [108, 160, 161], and can be scaled according to the flame Strouhal number ($St = fR/S_L$, with r the pipe diameter and S_L the laminar flame speed) [57].

Going back to the oscillator equation, one can define the linear contribution of the source term to the system damping by defining $2\beta = n\cos(\omega_0\tau)$, corresponding to the real part of the previously defined source term. With this, the complete linear harmonic oscillator equation representing a thermoacoustic instability reads (in time domain):

$$
\ddot{\eta} - 2\nu_0\dot{\eta} + \omega_0^2\eta = 0,
\tag{1.7}
$$

with $\nu_0 = \beta - \alpha$ the linear growth rate of the instability. For $\nu > 0 \Leftrightarrow \beta > \alpha$ (resp. $\nu < 0 \Leftrightarrow \beta < \alpha$), the system experiences exponential growth (resp. decay). This modelling will be used for the electro-acoustic feedback loop that mimics a thermo-acoustic instability in chapters 2 and 3. Note that this oscillator equation models both acoustic resonator and source term at the same time. As mentioned in section 1.1, stabilization of the instability can be achieved by coupling the system to one or multiple other acoustic cavities, providing additional damping. This will be done in chapters 2 and 3.

In the case of aeroacoustic instabilities, the modelling of the shear layer source term can follow the same treatment, which was done in multiple studies. For instance in [50, 93, 112], transfer function modelling of the system is performed. This is based on a feedback loop with the backward transfer function modelling the acoustic resonator including damping. The forward transfer function modelling the shear layer, on the other hand, is based on vortex sound theory with a form similar to the $(n - \tau)$ model. Experimental studies have also been performed, where the experimentally measured shear layer transfer function also resembles a Strouhal number-scaled $(n - \tau)$ model [64, 151], with $St = fW/U$, with W the width of the opening and U the mean flow velocity. The additional step of incorporating the source term inside a single harmonic oscillator equation through its linear contribution has also been done by Boujo *et al.* [21].

In this thesis, a different approach will be used: the results of the shear layer transfer function measurements will be fitted with a second-order transfer function which, transformed back into the time domain, will give us the second oscillator equation, to be coupled with that of the acoustic resonator. This approach for the aeroacoustic source term modelling has also been used in the work of Debut *et al.* [41].

As mentioned earlier, for the acoustic resonators acting as *dampers* mentioned in section 1.2.1, even in pure bias flow cases the effect of the vortex shedding can lead to sound production [177, 193, 195]. This ultimately shows that even within the modelling of the damper used in this thesis, there is another layer of modelling hidden inside the *pressure loss coefficient* $\zeta_{H,Q}$, which accounts for the dissipation. It is not impossible to imagine a mapping of this coefficient similar to the one of β mentioned above, where the actual value of the pressure loss coefficient results from contribution from the dissipation in the acoustic boundary layers α_{bl} and the contribution from the shear layer/vortex sheet with a gain and a phase, which depending on the conditions either further stabilizes (chapters 2 and 3) or destabilizes (chapter 4) the system.

1.2.3 Nonlinearities and influence of noise

In the previous section, modelling of the *linear* contribution of the source term to the system stability has been shown. In practice, this is only useful to determine whether the system converges to or diverges from the origin: indeed the *linear* system, if not otherwise specified, is a linearized version of the complete system around the origin,
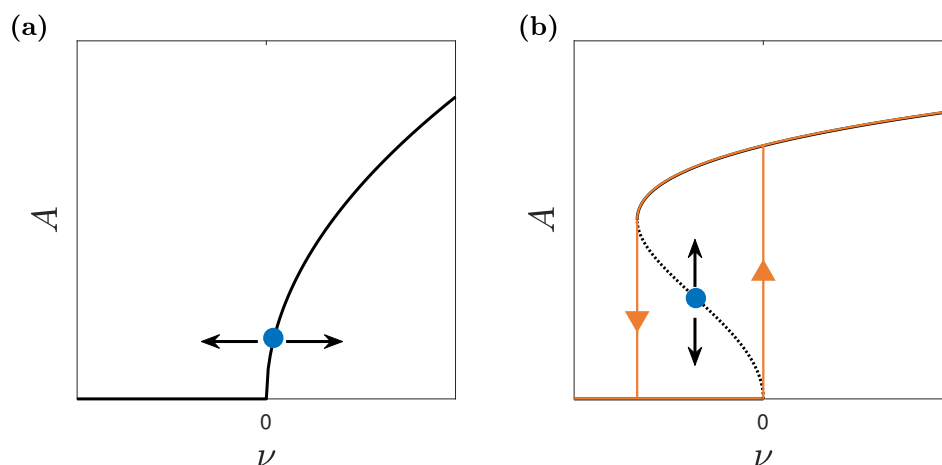
Figure 1.1: **(a)** Supercritical bifurcation, with arrow symbolizing multiplicative noise (i.e. $\nu = \nu(t)$), and **(b)** Subcritical bifurcation, with arrow symbolizing additive noise

meaning for very low values of the acoustic pressure and velocity. If the system is unstable, in this linear approximation, it would experience indefinite exponential growth. In the real world, this does not happen and some saturation mechanism occurs, allowing the system to stabilize on a limit cycle. The saturation mechanisms are modelled in the form of nonlinear terms in the oscillator equations, i.e. terms that are not proportional to the acoustic variables or their derivatives.

In the case of thermoacoustic instabilities, the nonlinear response from the flame can be measured in a similar way to the flame transfer function, but with varying excitation amplitude, the so-called *flame describing function* [48,131]. The behaviour of the flame heat release as function of excitation amplitude was measured experimentally in [4,90]. The flame response can then be approximated by its Taylor expansion [106]. This was done in [129] with a superposition of linear and cubic term, and with an arctan function. A superposition of linear, cubic and quintic term was even used in [14]. For the purpose of this thesis, which is not to describe the flame saturation mechanism accurately, a simple cubic saturation term will be added to the damping term, thus making the equation modelling the instability similar to that of a Van der Pol oscillator. In the electro-acoustic feedback loop used to mimic the instability in chapters 2 and 3, the saturation term can be freely chosen, so there a cubic saturation was also implemented.

In the case of aeroacoustic instabilities a slightly different approach was used, since the literature on shear layer saturation is scarce. In chapter 4, a describing function approach was used, meaning the shear layer acoustic response was measured for different excitation amplitudes, and the fitting parameters of the linear 2$^{\text{nd}}$ order transfer function were determined in each case. The evolution of these parameters with amplitude was then fitted with constant, linear or quadratic functions, giving a superposition of linear and quadratic term for the damping, and a superposition of linear and cubic term for the dissipative coupling.

Up until now only the nonlinearities stemming from the source term acoustic response were covered. However, another nonlinearity needs to be taken into account: in the case of Helmholtz resonators used as *dampers* and purged by a mean flow, if the damper is excited beyond a certain amplitude, the flow in the damper neck reverses during part of the cycle, and the dissipation is proportional to the reverse flow velocity during this part of the cycle. Because of this, an "absolute value" nonlinearity is used for the acoustic damper in chapter 3 [8, 86, 208].

In the deterministic case, the nonlinearities determine the structure of the coupled system bifurcation diagram. The simplest case between a stable system and a system experiencing instability is the Hopf bifurcation (displayed Fig. 1.1(a), black line). In this type of bifurcation where the system is stable while the growth rate of the coupled system $\nu < 0$ (the origin is the only fixed point of the system). At $\nu = 0$, the Hopf bifurcation occurs, and for $\nu > 0$ the system has an unstable fixed point at the origin and a stabe limit cycle, with the limit cycle amplitude A following a monotonous increase as function of ν. This is the typical bifurcation diagram of a simple Van der Pol oscillator. Is this case, for all values of ν the system has either only one stable fixed point, or one stable periodic solution and an unstable fixed point.

Other types of nonlinearities can lead to a very different bifurcation diagram. For instance, the flame nonlinear response modelling using up to the quintic term in [14] allows to model an experimentally observed subcritical bifurcation, whose shape is shown in Fig. 1.1(b) (black line). For this type of system, there is a range of ν where the system has both a stable fixed point (at the origin) and a stable limit cycle that coexist. This means that depending on the initial value, in this range the system can stabilize on either one of those, which leads to a *hysteretic* behaviour (orange curve). This type of behaviour will be shown for a combination of cubic and absolute value nonlinearities in chapter 3. It has also been shown in the context of aeroacoustic instabilities [205], although this is not reproduced in this thesis.

Now in reality, the systems considered are far from deterministic, since there is always a stochastic noise coming from the turbulence directly (in the case of aeroacoustic instability), or indirectly, through the noisy component of the heat release in the case of thermoacoustic instabilities [13]. One effect of the noise can be that the oscillation amplitude oscillates around its theoretical value. But it can also lead to more extreme effects, for instance intermittency (bursts). This should not be confused with chaotic behaviour, which has also been demonstrated in the case of thermoacoustic instabilities [65, 99, 128].

In the case of stochastic bursts, one must distinguish between two possible causes: (i) the system jumps between coexisting stable states, which typically arises from some subcritical type of bifurcation with *additive* noise [14], shown in Fig. 1.1(b) (arrows) (ii) the system moves back and forth around the bifurcation point under the effect of *multiplicative* noise [29, 103, 118], shown in Fig. 1.1(a) (arrows). The focus of the stochastic study in this thesis (section 4.5) will be on the latter.

1.3 Structure of the thesis

The structure of the thesis is the following: chapter 2 investigates the stabilization capabilities of acoustic damper on a linearly unstable acoustic mode. To this end, the modelling of the acoustic dampers as linear damped harmonic oscillators is detailed, both for the Helmholtz as well as for the Quarter-wave geometry. The electro-acoustic mimicking of a thermoacoustic instability, which allows for the fine-tuning of the unstable acoustic mode parameters, is also detailed. A linear stability analysis follows, culminating in the derivation of the best stabilization parameters which correspond to an exceptional point of the coupled system.

Chapter 3 builds upon the model of chapter 2 with the addition of nonlinearities: the chamber nonlinearity is modelled as a cubic nonlinearity, corresponding to the electro-acoustic mimicking experiment. The nonlinearity of the acoustic damper is measured separately and modelled using a function, named g_Q in the present thesis, that has already been used multiple times in the literature [8, 86, 208]. With this, the number of fixed points and limit cycles in the system can be determined for all sets of parameters using the averaged "slow-flow" equations, allowing for the derivation of bifurcation diagrams, involving not only "simple" Hopf bifurcations, but also fold bifurcations. The bifurcation diagrams are successfully compared to the experimental pressure amplitude while quasi-steady ramping the growth rate of the unstable mode, and the hysteretic behaviour of the system is underlined.

Chapter 4 deals with the second type of instability, namely the aeroacoustic instability. In this chapter, the modelling of the shear layer "source term" is performed by fitting linear and nonlinear acoustic responses with a second order transfer function. In that way, the shear layer coupled to a deep cavity of varying depth (modelled as a quarter-wave damper as in chapter 2) can be modelled as a system of coupled oscillators. Again, linear stability analysis is performed, as well as the derivation of the averaged "slow-flow" equation in order to determine the stability limits and the limit cycle amplitudes. There it is demonstrated that the deterministic system exhibits only Hopf bifurcations. Since the experiments showed evidence of intermittency, the last part of chapter 4 deals with the effect of multiplicative noise and draws necessary conditions for this type of noise to lead to intermittency.

The appendix demonstrates a condition on the frequency ramp rate for the valid use of sweep experiments, as was extensively used in chapter 2. A visual summary of the thesis can be seen in Fig. 1.2.
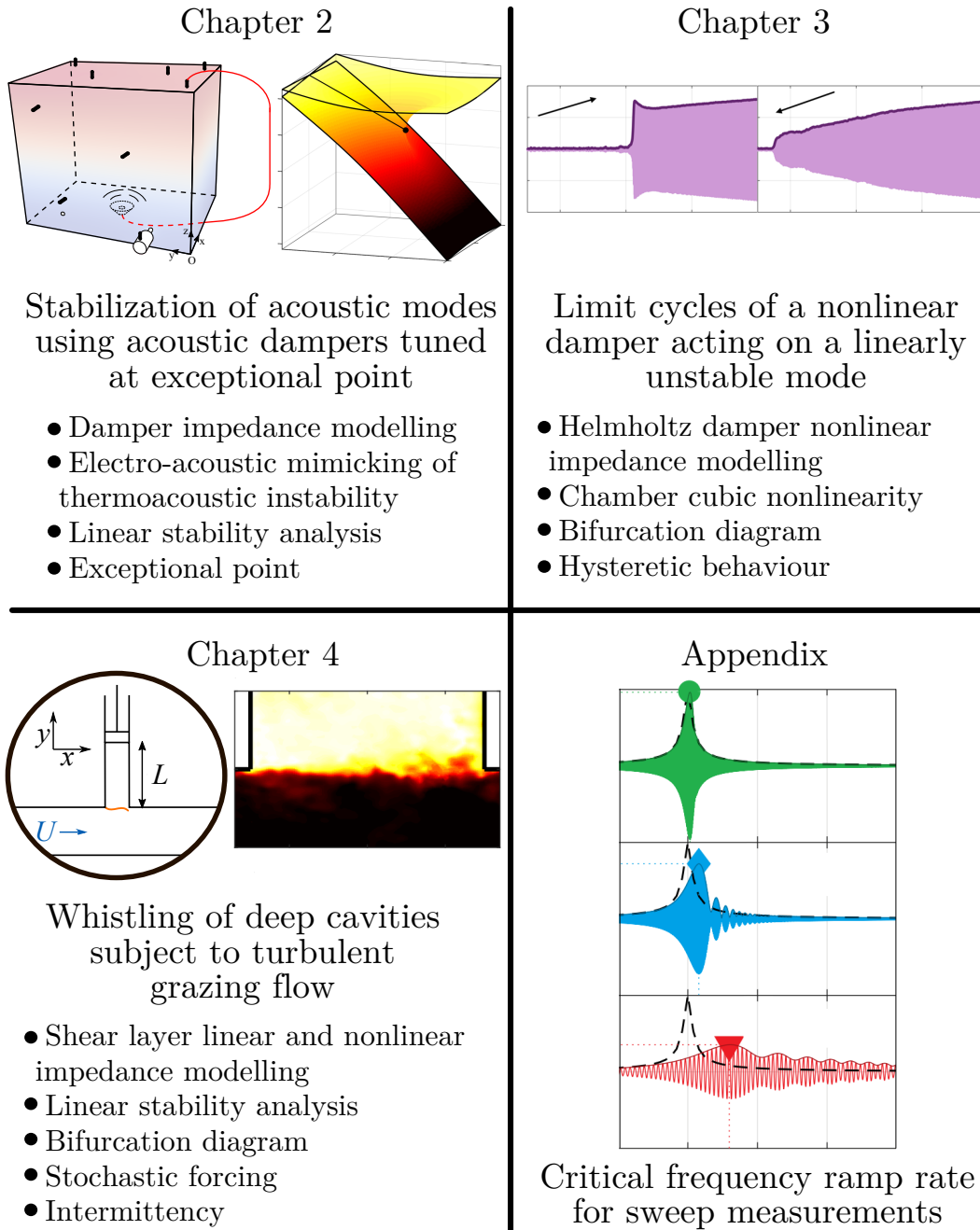
Chapter 2

Stabilization of acoustic modes using acoustic dampers tuned at exceptional point

- Damper impedance modelling
- Electro-acoustic mimicking of thermoacoustic instability
- Linear stability analysis
- Exceptional point

Chapter 3

Limit cycles of a nonlinear damper acting on a linearly unstable mode

- Helmholtz damper nonlinear impedance modelling
- Chamber cubic nonlinearity
- Bifurcation diagram
- Hysteretic behaviour

Chapter 4

Whistling of deep cavities subject to turbulent grazing flow

- Shear layer linear and nonlinear impedance modelling
- Linear stability analysis
- Bifurcation diagram
- Stochastic forcing
- Intermittency

Appendix

Critical frequency ramp rate for sweep measurements

Figure 1.2: Visual summary of the topics addressed in subsequent chapters

Chapter 2

Stabilization of acoustic modes using Helmholtz and Quarter-Wave resonators tuned at exceptional points

In the present chapter, an experimental and theoretical study is conducted, considering both Helmholtz (HH) and Quarter-Wave (QW) acoustic cavities as potential passive damping systems in order to stabilize a thermoacoustic unstable mode. Since the resonators are simply added to the system in order to achieve additional damping, they will be called *dampers* in all of Chapter 2 and 3. A model for their acoustic impedance is derived and experimentally validated. In a second part, a thermoacoustic instability is mimicked by an electro-acoustic feedback loop in a parallelepipedic cavity, thereafter called *chamber*, to which the dampers are added. The length of the dampers can be adjusted, so that the system can be studied for tuned and detuned conditions. The linear stability of the coupled system is investigated experimentally and then analytically, which shows that for tuned dampers, the best stabilization is achieved at the exceptional point. The stabilization capabilities of HH and QW dampers are compared for given damper volume and purge mass flow.

2.1 Introduction

In order to achieve efficient and clean combustion, there is a dire need for robust control strategies to prevent thermoacoustic instabilities. The use of passive damping devices such as Helmholtz (HH) or Quarter-Wave (QW) dampers is a cost-effective option to prevent these combustion instabilities [96, 202].

In the seventies, thermoacoustic instabilities in rocket engines were the topic of several studies, where different acoustic damping enhancement strategies were compared: for example baffles, HH and cylindrical liners in [36], HH, QW and Quincke resonator in [68]. A more recent study dealing with the comparison of absorption coefficients of half-wave, QW and HH is proposed in [172]. Keller [87] stated that the QW has a narrower bandwidth than the HH, but it is less influenced by nonlinearities [98]. Although up until two decades ago, the studies on damping device design for rocket engine combustion instabilities still dealt with QW as well as HH [2], nowadays most of the available literature concentrates on QW resonator rings [134]: in [135], the influence of the resonator length on the frequency of the engine acoustic modes is studied and [28] presents a graphical method based on a low-order network model to determine the stability of the system. The influence of such a QW resonator ring on the shape of the longitudinal and transversal [162] as well as azimuthal [200] modes, and on the stability margin of the engine [199] has also been studied. On the contrary, the literature on QW applications in aeroengines is sparse (e.g. [80] and [120] with QW tubes installed upstream of the premixers), whereas one can find many papers about acoustic liners, behaving as matrices of HH resonators [25, 61, 75]. HH and QW are also used to hinder thermoacoustic instabilities in the combustors of land-based gas turbines for power generation [148]. Over the last two decades most publications deal with the use of HH dampers, either conventional [158] (with a detailed model derived in [8] and design principles given in [47]), or featuring multiple volumes, i.e. having several interconnected inner cavities [17,18]. Overall, the choice of using HH or QW dampers to suppress thermoaocustic instabilities in combustion chambers is often guided by field-specific trends or past experience of the manufacturers. The present chapter provides a detailed comparison of the damping capabilities of HH and QW resonators.

Another aspect of the present work is to investigate the stabilizing capabilities of flow-purged dampers on self-sustained oscillations. A large number of investigations dealing with modal damping enhancement using acoustic dampers generally focus on linearly stable configurations where there is no through-flow in the damper: for instance, in [52, 141], the optimal damping is determined for a configuration where acoustic and structural modes are coupled; In [92, 198], the authors underline that the optimal damping depends on whether one wants to achieve minimum narrow-band or broad-band response or minimum reverberation time. The influence of the detuning of the damper has been studied in [34,66] while the effect of multiple dampers is scrutinized in [137]. Several experimental and analytical studies deal with methods to find the optimum number of dampers and their best positioning in the combustion chamber,

e.g. [197, 201]. A recent work proposes to automatize the damper design process by using computationally-cheap adjoint-based optimization [116].

In the specific case of gas turbine combustors, dampers and perforated liners are connected to the combustion chamber. Their neck interfaces the hot combustion products, and the dampers are usually air-purged (e.g. [47, 203]), in order to adjust their acoustic resistance, and to prevent hot gas ingestion, which could not only damage them, but also detune them. A few studies deal with the influence of the associated density discontinuity on the impedance of Helmholtz dampers [19, 194]. Another recent work [32] investigates how the impedance of a HH damper nonlinearly depends on the amplitude of the acoustic level in the combustion chamber, which induces, beyond a certain threshold, *periodic* hot gas ingestion.

In this context, the goal of the experimental and analytical study in this chapter is to build on the work proposed in [132] and investigate the potential of air-purged HH and QW dampers to increase modal damping in combustion chambers. This investigation focuses on the linear stability of the coupled system "dampers-combustion chamber". The complementary study dealing with the associated nonlinear dynamics will be presented in chapter 3.

In the first section, the impedance of stand-alone HH and QW dampers is modeled and experimentally validated for a range of purge mass flows and damper volumes. In practice, the available ranges for these two parameters are bounded by technical constraints: i) the available volume for damper implementation is usually limited and the size of the dampers must be adjusted accordingly; ii) the amount of purge air must be as low as possible, but sufficiently large to provide required damping performance. In fact, regarding ii), the following conflicting constraints must be satisfied: bypassing compressed air from the combustion process to supply the dampers has a negative impact on the performance and emissions of the combustor and it should therefore be minimized; however, it should be large enough such that the risk of hot gas ingestion is properly mitigated.

In the second section of this chapter, the dampers are connected to a chamber in order to stabilize self-sustained acoustic oscillations. For the experimental investigation, one uses an electro-acoustic feedback in an enclosure in order to mimic thermoacoustic instabilities in combustion chambers. This experimental set-up is more flexible than a combustion experiment and gives full control on the parameters governing the self-sustained acoustic oscillations. A theoretical model of the coupled system "chamber-damper" is derived and successfully compared against experimental data.

In the last part of this work, one investigates the existence of acoustic *exceptional points* in chambers which are equipped with dissipative resonators. Exceptional points (EP) pertain to systems exhibiting a special eigenvalue degeneracy, for which not only the eigenvalues, but also the eigenvectors coalesce when one of the governing parameters is adjusted. Investigation of EPs in quantum mechanics, optics, electronics, mechanics or
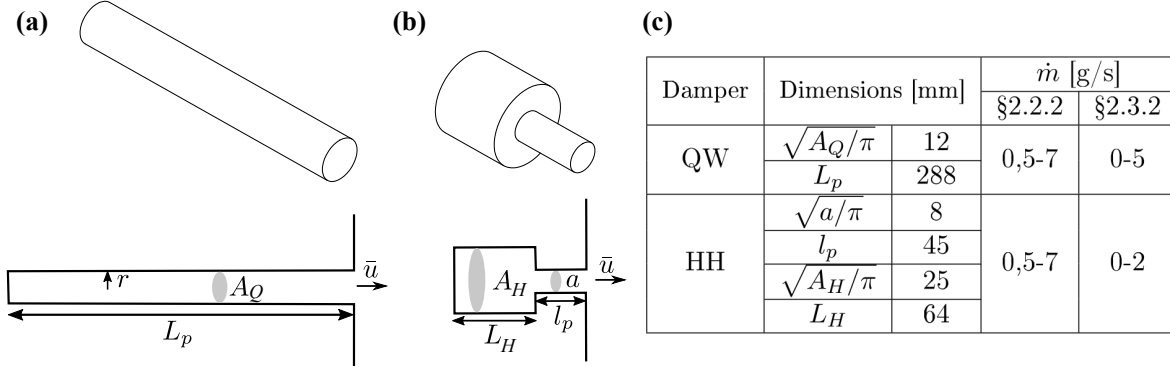
Figure 2.1: Resonator geometry for **(a)** QW, **(b)** HH. **(c)** Table summarizing the dimensions of the dampers and the mass flows used throughout this chapter.

acoustics is the subject of intense ongoing research [167], e.g. [70] for damping of friction-induced instabilities, [204] for unidirectional invisibility in an acoustic waveguide, [60] for exciton-polaritons in semiconductor microcavities, [23] for coupled lasers, [1, 191] for the design of acoustic metamaterials, [155] for the transient dynamics in the vicinity of EPs, or [43] for the intriguing acoustical properties of coupled cavities. Their importance in the understanding of thermoacoustic instabilities has been highlighted in [115].

In the present chapter, it will be shown that the best stabilization of the acoustic mode is achieved when the resonance frequency and the damping of the HH or QW resonators are fine-tuned at the EP of the coupled system.

2.2 Damper modelling

2.2.1 Impedance model

In this section second order harmonic oscillator models are introduced for the impedance of HH and QW dampers. In the remainder of the thesis, $(\cdot)_H$ refers to quantities related to the HH resonator, while $(\cdot)_Q$ refers to those related to the QW resonator. Both resonators considered in this chapter are axisymmetric.

Helmholtz resonator (H)

The HH resonator is sketched in Figure 2.1**(b)** and Figure 2.3**(b)**. Assuming plane wave propagation in the back volume of length L_H and in the neck of effective length $l = l_p + l_{\text{cor}}$ (with end corrections on both sides), one can write the following expression for the damper reactance at the neck:

$$\Im(Z_H) = -\rho c \, \frac{a - A_H \tan(\omega l/c)\tan(\omega L_H/c)}{a \tan(\omega l/c) + A_H \tan(\omega L_H/c)}, \tag{2.1}$$

14

with Z_H the damper impedance, ρ and c the air density and the speed of sound in the damper, ω the angular frequency, a the neck cross-section and A the back-volume cross-section. Considering compact neck and compact volume length with respect to the resonance wavelength ($\tan \omega l/c \simeq \omega l/c$ and $\tan \omega L/c \simeq \omega L/c$), and the fact that the area ratio between neck and volume is small ($a \ll A_H$), Eq. (2.1) can be simplified to:

$$\Im(Z_H) = \rho l \frac{\omega^2 - \omega_H^2}{\omega}, \tag{2.2}$$

where $\omega_H = c\sqrt{a/V_H l}$ the damper's resonance frequency, with $V_H = A_H L_H$ the damper back volume. In the present work, it is assumed that coherent vortex shedding at the HH resonator mouth is the main dissipation mechanism [181] and that the resistance of the damper can be written as:

$$\Re(Z_H) = R_H = \zeta_H \rho \bar{u} = \zeta_H \frac{\dot{m}}{a}, \tag{2.3}$$

with ζ_H a pressure loss coefficient depending on the neck geometry and position, $\bar{u}$ the mean velocity through the HH neck, and $\dot{m}$ the mean mass flow through the neck, which is a critical parameter in real turbomachinery applications. This expression is obtained by linearizing the Bernoulli equation across the neck (e.g. [149]). Please note that should the acoustic amplitude become high, the resistance would not be proportional to $\bar{u}$ but to $|\bar{u} + u'|$, with u' the acoustic velocity in the neck. Using a purely linear dissipation term is justified for the present study, which focuses on the linear stability limits. The reader can refer to chapter 3 where the nonlinear problem is investigated. Eq. (2.3) does not depend on the resonance frequency, and the pressure loss coefficient ζ_H gives the energy transfer from the acoustically-driven incompressible potential flow through the neck to the vortices that are periodically shed from the rim of the neck outlet. One can refer to [193] for a detailed investigation on the modeling of orifice impedance for a broad range of geometries and Strouhal numbers. Combining (2.2) and (2.3), one obtains the HH resonator impedance:

$$Z_H = \rho l \frac{s^2 + \omega_H^2}{s} + R_H, \tag{2.4}$$

with $s = i\omega$ the Laplace variable, which is the classical $(l - \zeta)$ model, where l stands for the effective length of the inertial mass of air in the orifice and ζ for the pressure loss coefficient defining the acoustic resistance against the oscillation of air in the orifice. It was discussed for example by Morse and Ingard [122] at page 760, or in [8, 149].

Quarter-wave resonator (Q)

The QW resonator is sketched in Figure 2.1(**a**) and Figure 2.3(**c**). Assuming plane wave propagation in the resonator with an effective length $L = L_p + L_{\text{cor}}$ (including an end correction at the outlet), one gets the following expression for the damper reactance:

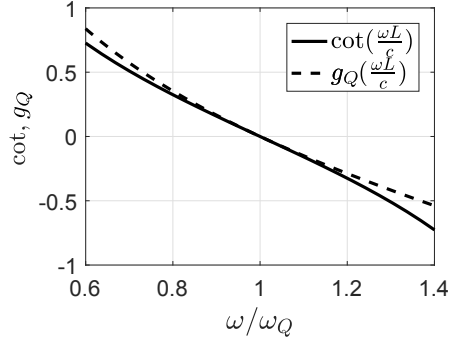$$\Im(Z_Q) = -\rho c \frac{1}{\tan(\omega L/c)}. \tag{2.5}$$

Figure 2.2: Comparison between actual reactance with cotangent and simplified function. $\omega_Q = \pi c/2L$ so that when $\omega = \omega_Q$, $\omega L/c = \pi/2$

At resonance frequency, $\omega_Q L/c = \pi/2$. For angular frequencies ω that are close to the resonance frequency, one can use the following approximation:

$$\frac{1}{\tan x} \simeq g_Q(x) = -\frac{1}{2}\left(x - \frac{\pi^2}{4x}\right),\qquad(2.6)$$

which is illustrated in Figure 2.2 and leads to:

$$\Im(Z_Q) = \rho\frac{L}{2}\frac{\omega^2 - \omega_Q^2}{\omega},\qquad(2.7)$$

with $\omega_Q = \pi c/2L$ the QW resonance frequency. Using this approximation is quite uncommon in the literature, although it provides an explicit formulation of the QW resonator impedance as a second order harmonic oscillator. Regarding dissipation, the resistive term in the QW case is composed of two contributions: one of them is the vortex shedding at the damper mouth as for the HH resonator:

$$R_{\mathrm{vs}} = \rho\zeta_Q\bar{u} = \zeta_Q\frac{\dot{m}}{A_Q}.\qquad(2.8)$$

The second contribution comes from the losses in the acoustic boundary layer [122,163], with the following expression for the viscous and thermal power loss per wall unit area:

$$\mathcal{L}_{\mathrm{bl}} = \frac{\rho\,\omega\,\delta_{\mathrm{bl}}}{2}\left|\hat{u}_{\mathrm{rms}}\right|^2 + \frac{(\gamma - 1)\,\rho\,\omega\,\delta_{\mathrm{bl}}}{2\sqrt{Pr}}\left|\frac{\hat{p}_{\mathrm{rms}}}{\rho c}\right|^2,\qquad(2.9)$$

where $\hat{u}_{\mathrm{rms}}$ and $\hat{p}_{\mathrm{rms}}$ are the root mean square amplitude of the acoustic velocity and pressure in the tube, $\delta_{\mathrm{bl}} = \sqrt{2\nu/\omega}$ the acoustic boundary layer thickness with ν the kinematic viscosity equal to $1.5 \cdot 10^{-5}$ m^2/s in air at ambient condition. γ is the specific heat ratio and Pr is the Prandtl number equal to 0.71 for air. Using the acoustic velocity and pressure distribution along the tube:

$$\hat{u}_{\mathrm{rms}}(x) = \frac{|\hat{u}_{\mathrm{max}}|}{\sqrt{2}}\sin\left(\frac{x\pi}{2L}\right)\quad\text{and}\quad\hat{p}_{\mathrm{rms}}(x) = \frac{|\hat{p}_{\mathrm{max}}|}{\sqrt{2}}\cos\left(\frac{x\pi}{2L}\right),\qquad(2.10)$$

	Resistance [kg.s^{-1}]	Mass [kg]	Stiffness [kg.s^{-2}]
QW	$\rho \dfrac{A_Q L_p}{2r} \sqrt{2\nu\omega_Q} \left(1 + \dfrac{\gamma-1}{\sqrt{Pr}}\right) + \zeta_Q \dot{m}$	$\dfrac{\rho L A_Q}{2}$	$\dfrac{\pi^2}{8} \dfrac{\rho c^2 A_Q}{L}$
HH	$\zeta_H \dot{m}$	$\rho l a$	$\dfrac{\rho c^2 a^2}{V_H}$

Table 2.1: Equivalent resistance, mass and stiffness of HH and QW resonators.

using $|\hat{p}_{\max}| = \rho c |\hat{u}_{\max}|$, multiplying by the perimeter $2\pi r$ and integrating over the physical length L_p with respect to x gives the total boundary layer power losses for the QW damper:

$$\mathcal{L}_{\text{bl,t}} = \rho \frac{\pi r L_p}{4} \omega \delta_{\text{bl}} \left(1 + \frac{\gamma-1}{\sqrt{Pr}}\right) |\hat{u}_{\max}|^2. \tag{2.11}$$

Note that the viscous losses are about twice as high as the thermal losses. Hence, in the absence of mean flow, the acoustic resistance per unit area associated with the above power loss is:

$$R_{\text{bl}} = \frac{\mathcal{L}_{\text{bl,t}}}{\pi r^2} \frac{2}{|\hat{u}_{\max}|^2} = \rho \frac{L_p}{2r} \sqrt{2\nu\omega} \left(1 + \frac{\gamma-1}{\sqrt{Pr}}\right). \tag{2.12}$$

Since R_{bl} is proportional to $\sqrt{\omega}$ one can approximate a constant value around the resonance frequency of the damper. The total resistive term is then:

$$R_Q = R_{\text{bl}} + R_{\text{vs}} = \rho \frac{L_p}{2r} \sqrt{2\nu\omega_Q} \left(1 + \frac{\gamma-1}{\sqrt{Pr}}\right) + \zeta_Q \frac{\dot{m}}{A_Q}, \tag{2.13}$$

and the QW damper impedance:

$$Z_Q = \rho \frac{L}{2} \cdot \frac{s^2 + \omega_Q^2}{s} + R_Q. \tag{2.14}$$

Using the impedance equations and accounting for the interface area (a for HH, A_Q for QW), one can get the resistance, mass and stiffness of the equivalent mechanical oscillators given in Table 2.1.

Note that the equivalent stiffness of the QW K_Q is slightly higher than the one K_{ac} associated with the bulk compression of an air column of length L, using $\gamma \bar{p} = \rho c^2$:

$$K_Q = \frac{\pi^2}{8} \frac{\rho c^2 A_Q}{L} = \frac{\pi^2}{8} \frac{\gamma \bar{p} A_Q}{L} = \frac{\pi^2}{8} K_{\text{ac}}, \tag{2.15}$$

with $\bar{p}$ is the ambient pressure.

2.2.2 Reflection coefficient measurements and model tuning

A HH damper and a QW damper were used for the experimental investigations. A piston allows variation of their volume such that their resonance frequency can be adjusted between 200 and 500 Hz. The HH damper neck has a diameter of 16 mm and a length of 45 mm. At the frequency of interest in the second part of this chapter (287 Hz), the back-volume of the HH is 64 mm long, with a diameter of 50 mm (see Figure 2.3(b)), and the length of the QW is 288 mm with a diameter of 24 mm (see Figure 2.3(c)). The edges of both the HH neck and the QW outlet are sharp. For the reflection coefficients measurements, the mass flow $\dot{m}$ is varied between 0.5 and 7 g/s.
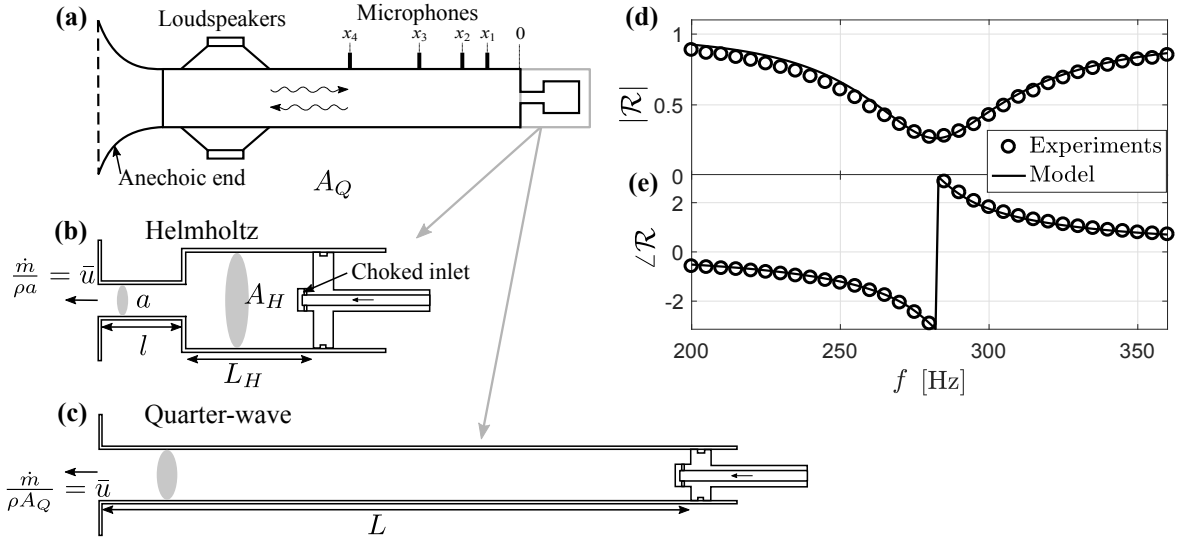

Figure 2.3: (a) Schematic of the impedance tube used for the reflection coefficient measurements. (b) Sketch of the Helmholtz resonator with variable back volume length. (c) Sketch of the Quarter-Wave resonator with variable length. (d) Magnitude and (e) phase of the reflection coefficient for the HH damper with $\dot{m} = 1.5$ g/s. The model (plain line) is fitted to the experimental results (circles) by adjusting R_H.

The impedances of the HH and QW dampers given in Eqs (2.4) and (2.14) feature two parameters that are empirically estimated in the present work: the length corrections (l_{cor} and L_{cor} respectively) and the pressure loss terms (ζ_H and ζ_Q respectively).

The end corrections are determined using the Helmholtz solver AVSP for a configuration where the dampers are connected to an impedance tube with a 62×62 mm^2 cross-section. AVSP solves the Helmholtz equation as an eigenvalue problem in quiescent domains with possible non-uniform temperature distribution [127]. The solver gives the first eigenfrequency and the end corrections are obtained using the expressions $\omega_H = c\sqrt{a/V_H l}$ and $\omega_Q = \pi c/2L$. This gives $l_{\text{cor}} = 13.2$ mm and $L_{\text{cor}} = 4.2$ mm.

For the determination of the pressure loss coefficients ζ_H and ζ_Q, reflection coefficients measurements were performed with an impedance tube of section $S_{\text{IT}} = 62 \times 62$ mm^2

(see Figure 2.3(**a**)) using the Multi-Microphone-Method (MMM) [159]. For each mass flow, the value of the acoustic resistance is empirically adjusted so that the best fit between experimental and theoretical reflection coefficient $\mathcal{R} = (Z - \rho c)/(Z + \rho c)$ is achieved. Here, the analytical expression for the impedance Z is obtained by dividing Eq. (2.4) for the HH (resp. Eq. (2.14) for the QW) by the area ratio $\sigma_H = a/S_{\mathrm{IT}}$ (resp. $\sigma_Q = A_Q/S_{\mathrm{IT}}$), such that it can be quantitatively compared to the experiments. An example of comparison between the HH damper model with tuned parameter R_H and the measurements for a selected mass flow $\dot{m} = 1.5$ g/s is given in Figure 2.3(**d**) and 2.3(**e**). Figure 2.4(**a-d**) shows the comparison between the model and the experiments for a range of mass flows. The comparison is also made for the QW damper in Figure 2.4(**e-h**). Overall, there is good agreement between model and experiments. One can note that there is a small drift of the eigenfrequency of the HH damper as a function of the purge mass flow, which means that the latter has an influence on the end correction, and that the HH damper is more prone to detuning than the QW damper when the velocity in the neck changes.

A linear regression is then used in both cases to determine the optimum values of ζ_H and ζ_Q from the fitted resistive terms. This is shown in Figure 2.5 and one obtains $\zeta_H = 1.78$ and $\zeta_Q = 1.64$. The mass flow $\dot{m}_0$ for which the reflection coefficient vanishes, which corresponds to an anechoic condition in the impedance tube, can be easily determined by matching the impedance at the plane where the damper is connected to the characteristic impedance of air. This mass flow depends on the cross-section of the impedance tube used for the measurement and is not an intrinsic property of the damper. At the resonance frequency, the reactive part of Z_H and Z_Q is zero. The condition giving no reflection is then: $R_H/\sigma_H = \rho c$ and $R_Q/\sigma_Q = \rho c$. Using $c = 343$ m/s and $\rho = 1.14$ kg.m^{-3} (the measurements were done at 500m above sea level) gives $\dot{m}_{0,H} = 2.6$ g/s which is in good agreement with the experiments, and $\dot{m}_{0,Q} = 11.3$ g/s.

For the HH damper this is also consistent with the findings of Scarpato et al. [157] who state that, at the anechoic condition, the Mach number divided by the porosity increases monotonically from 0.5 for low Strouhal number to $2/\pi$ for high Strouhal number. In the present work, the Strouhal number based on the opening diameter ($St = \omega_H \sqrt{4a/\pi}/\bar{u}$) ranges from 3 to 15, which correspond to a "high Strouhal" regime. Therefore, applying the condition proposed in [157]:

$$\frac{\bar{u}}{c}\frac{1}{\sigma_H} = \frac{\dot{m}_{0,H}}{\rho\,a\,c}\frac{1}{\sigma_H} = \frac{2}{\pi} \tag{2.16}$$

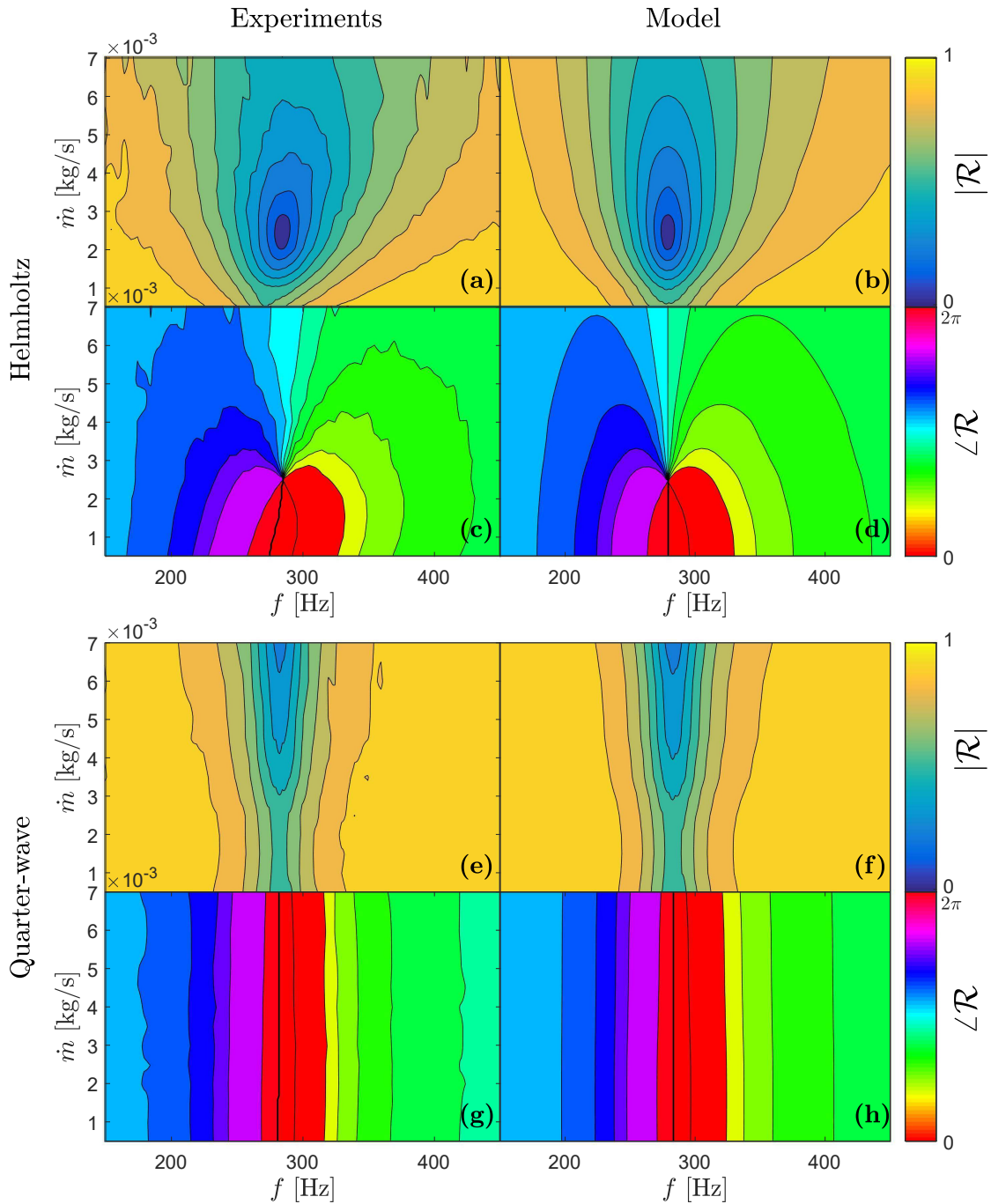gives $\dot{m}_{0,H} = 2.9$ g/s, which is in good agreement with the experimental value.

Figure 2.4: Results of the reflection coefficient measurements (left) and the tuned model (right). For the Helmholtz resonator: magnitude (**(a)**, **(b)**) and phase (**(c)**, **(d)**). For the Quarter-Wave resonator: magnitude (**(e)**, **(f)**) and phase (**(g)**, **(h)**).
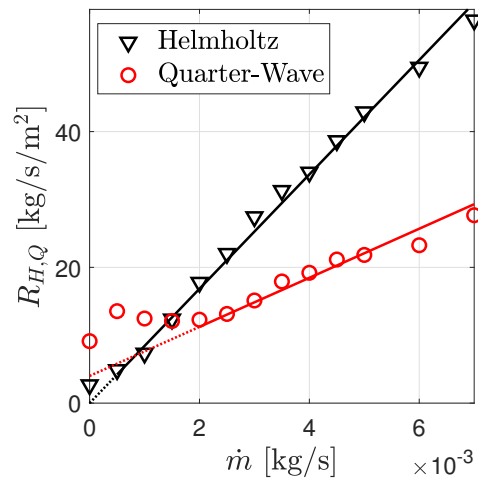
Figure 2.5: Acoustic resistance deduced from the measurement of the reflection coefficient as function of mass flow for the HH (triangles) and the QW (circles). Plain lines correspond to the linear regression on the value of ζ_H and ζ_Q using the analytical expressions from Eqs. (2.3) and (2.13): $R_H = \zeta_H \dfrac{\dot{m}}{a}$ and $R_Q = R_{bl} + \zeta_Q \dfrac{\dot{m}}{A}$. For the QW damper, the acoustic boundary layer losses do not depend on the mass flow, which is why the red line does not cross the origin.

2.3 Coupled damper-cavity experiments

The problem of dampers that are connected to a combustion chamber is now considered. This is a classical acoustic problem of coupled cavities (e.g. [122], Chap. 10.4), in the specific situation where one of the cavities, the combustion chamber, has a volume that is much larger than the one of the secondary cavities, namely the dampers. In that particular situation, the shapes of the first eigenmodes in the main cavity are usually not significantly altered by the implementation of the dampers, but the latter can strongly impact the stability of these modes.

In the present work, an electroacoustic feedback in a 0.2 m^3 chamber is used to mimic the thermoacoustic coupling occurring in combustion chambers. This experimental set-up allows for a precise control of the linear stability of one of the eigenmodes, with and without dampers. It is sketched in Figure 2.6.

2.3.1 Stand-alone cavity characterization

The experimental setup is composed of: 1) a rectangular metal box (500×700×600 mm^3) with stiffening ribs on the outer side of the walls to prevent strong vibro-acoustic feedback; 2) a set of eight G.R.A.S. 46BD 1/4" CCP microphones distributed on 2 of the faces of the cavity; 3) two Pioneer TS-1001I loudspeakers baffled in a rectangular polystyrene structure placed inside the cavity; 4) an electro-acoustic feedback loop, which consists of band-pass filtering, delaying and amplifying the signal from one of the microphones and delivering the output signal to one of the loudspeakers. By varying the amplification and the delay in the feedback loop, it is possible to vary the linear stability of one of the acoustic modes of the main cavity. The second loudspeaker serves as external excitation for forced experiments. The coordinates of the different elements are given in Figure 2.6. The microphones are calibrated using the Norsonic Nor1251 calibrator, giving an output of 114dB at 1000Hz.

The acoustic eigenmode considered in the following sections of this chapter is the first transversal mode (see Figure 2.6). The natural damping α of this mode, without damper and without electro-acoustic feedback, is obtained by imposing a ten-second linear sweep excitation from 200 to 400Hz using the second loudspeaker. Based on the critical ramp rates determine in the Appendix. A 2nd order transfer function is then fitted to the experimental transfer function between one of the microphone signals and the excitation signal in order to determine the eigenfrequency and the corresponding damping rate. This procedure is illustrated in Figure 2.7(c) and 2.7(d) and it provides the natural damping $\alpha = 4.8$ rad/s, which is also indicated as the central black dot in Figure 2.7(a). The main contribution to the damping of the eigenmode is attributed in the present situation to one-way acoustic-structure interaction.

In the following part of this work, a QW or HH damper is mounted on the cavity and a small hole in one of the walls of the cavity serves as exhaust for the damper purge air that is injected into the cavity (see Figure 2.6). Damping rate measurements were

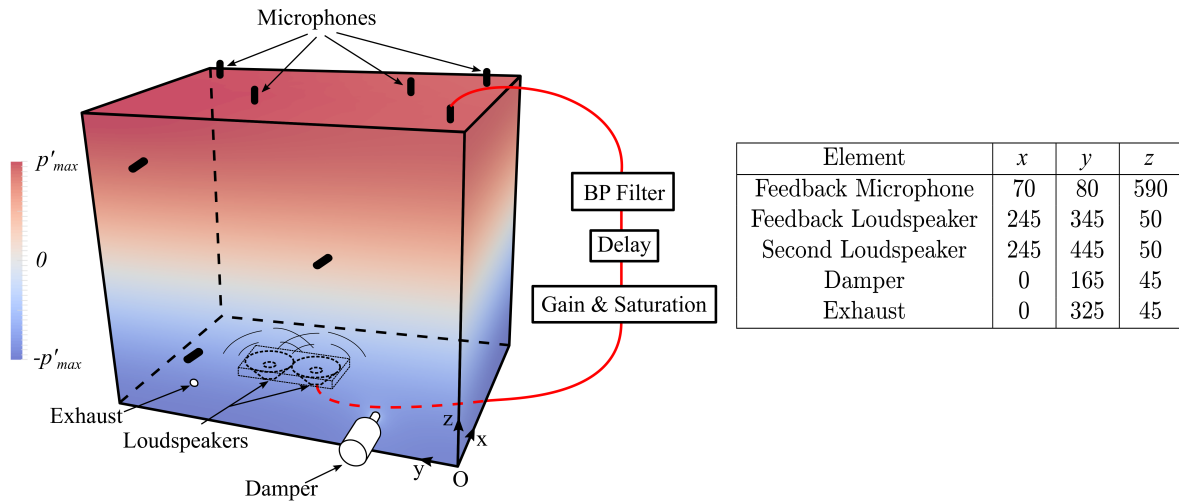| Element	x	y	z
Feedback Microphone	70	80	590
Feedback Loudspeaker	245	345	50
Second Loudspeaker	245	445	50
Damper	0	165	45
Exhaust	0	325	45

Figure 2.6: Sketch of the experimental setup and coordinates of the elements in mm

performed in order to identify the effect of an air flow through this exhaust orifice on the natural damping of this eigenmode. These tests showed that the corresponding additional damping does not exceeds 0.4 rad/s (α comprised between 4.8 and 5.2 rad/s) over the entire range of purge mass flows considered, which is negligible compared to the damping rate variations induced by the electro-acoustic feedback loop and/or the HH and QW dampers.

The signal of the microphone used in the feedback loop is filtered, delayed, amplified to supply the loudspeaker as was done in e.g. [132, 133]. This real-time signal processing is done using a NI cRIO-9066 board. The filter is necessary to ensure that the feedback loop only acts on the first transversal acoustic mode of the cavity at a frequency of about 287 Hz. The filter is a bandpass with cut-off frequencies at 260 and 320 Hz. When the gain and the time delay in the feedback loop lead to a linearly unstable situation, there is an exponential growth of the amplitude of the first transversal mode. A nonlinear cubic term is implemented in the feedback loop such that the exponentially growing oscillations saturate on a limit cycle, with the dynamics of a Van der Pol oscillator. One can therefore express the amplitude η of the first transversal mode of the electro-acoustic system as:

$$\ddot{\eta} - (2\nu_0 + \kappa\eta^2)\dot{\eta} + \omega_0^2\eta = 0, \tag{2.17}$$

with ν_0 its linear growth/decay rate without damper, ω_0 its natural angular frequency and κ the saturation coefficient. The linear growth rate ν_0 results from the contribution of the linear damping α and the linear gain of the electro-acoustic feedback loop β, such that $\nu_0 = \beta - \alpha$. The input of the loudspeaker is proportional to $c_1 U_f(t - \tau) + c_2 U_f^3(t - \tau)$, where U_f is the output voltage of the band-pass filtered signal from the feedback microphone, c_1 and c_2 are the linear amplification and the saturation coefficients, and τ the feedback delay. The latter three parameters can be specified in the real-time feedback algorithm. As a first approximation, $\beta \propto c_1 \cos(\omega_0 \tau)$ and the linear growth
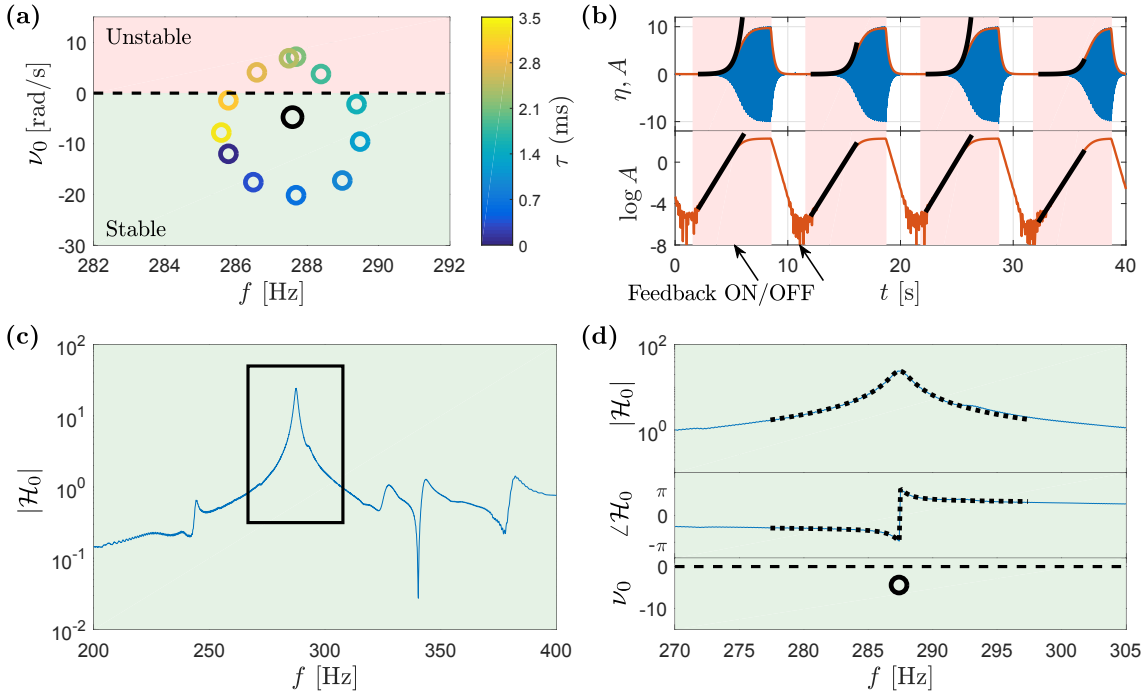
Figure 2.7: **(a)** Measured eigenfrequencies of the first transversal mode, without and with electroacoustic feedback (resp. black and colored circles), for a range of feedback loop delays, and for the cavity without dampers. **(b)** For feedback loop delays τ leading to linearly unstable situations, the linear growth rate (real part of the eigenfrequency) is obtained by fitting an exponential on the transient. **(c)** For feedback loop delays τ leading to linearly stable situations, the second loudspeaker is used to force the system with a frequency sweep. The associated transfer function $\mathcal{H}_0 f$ shown in **(c)** and **(d)** is fitted with a second-order low-pass filter, which provides the eigenfrequency of the electro-acoustic system.

rate ν_0 is positive when $\beta > \alpha$, which can be achieved for a range of delays τ and amplification factor c_1.

Figure 2.7**(a)** shows the measurements of the eigenfrequency and growth/decay rate of the first transversal mode when the electroacoustic feedback is active, for different feedback delays τ and for fixed c_1 and c_2. When the electroacoustic system is linearly unstable (red background), growth rate measurements were performed by fitting exponential curves on the transient growth of the acoustic amplitude (Figure 2.7**(b)**) and taking the average over 10 realizations. The standard deviation to mean ratio of such growth rate measurements can be seen Figure 2.8**(b)** for different values of c_1, which shows very good accuracy. For the linearly stable cases (green background), the measurement technique is the same as for measuring the natural damping of the mode (Figure 2.7**(c)** and 2.7**(d)**), namely performing sweep measurements. In addition to having checked that the frequency ramp rate used during the sweeps were compli-

ant with the limits defined in the Appendix, the accuracy of the sweep measurements was checked using decay rate measurements: the second loudspeaker is used to excite the system at its resonance frequency, and when the excitation is stopped the transient decay of the acoustic amplitude is fitted with an exponential curve. These decay rate measurements are averaged over 10 realizations and gives similar accuracy as the growth rate measurements. The decay rates ν_0 obtained from the sweep measurement was always within one standard deviation compared to the one obtained from decay rate measurement.

In the remainder of this chapter, the delay $\tau = 2.2$ ms, which gives the most constructive feedback, and the saturation coefficient c_2 are kept constant. The linear growth rate ν_0 of the system without dampers is varied by adjusting c_1, according to the linear regression shown in Figure 2.8(**a**). The effective saturation constant κ can be deduced from the square root evolution of the oscillation amplitude when ν_0 is varied. Indeed, the theoretical limit cycle amplitude of Eq. (2.17) is $A = \sqrt{-8\nu_0/\kappa}$ (see [133]), and $\kappa = -0.08$ s^{-1}Pa^{-2} was deduced from these measurements.
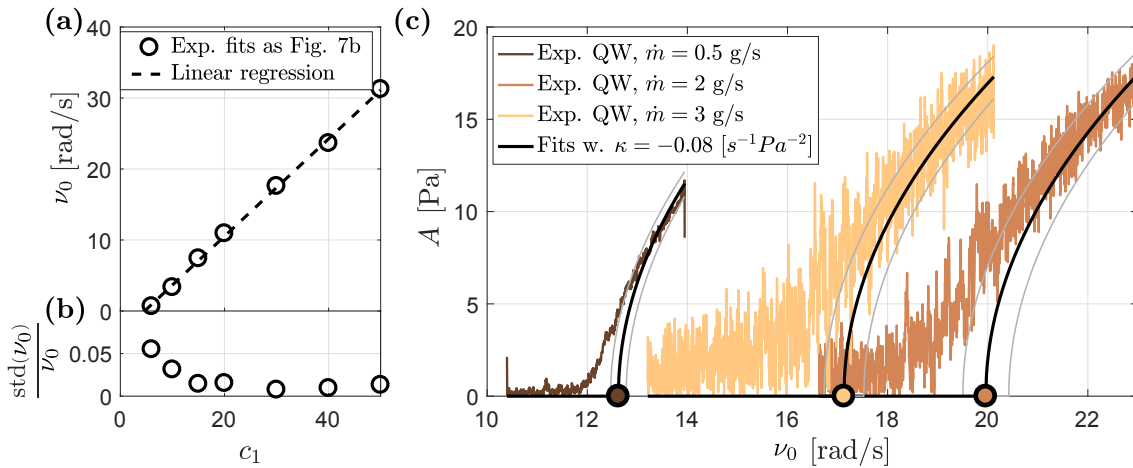
2.3.2 Addition of dampers

Figure 2.8: (**a**) Relation between c_1 and ν_0 for several growth rate measurements, and linear regression verifying proportionality. (**b**) Standard deviation to mean ratio for the previous growth rate measurements, showing very good accuracy. (**c**) Example of the stability limit measurements for the tuned QW for 3 different mass flows. ν_0 is slowly ramped down and the resulting pressure envelope is fitted using $\kappa = 0.08$ [s^{-1}.Pa^{-2}].

A HH or QW damper can be connected to the cavity and fed with a purge flow as shown in Figure 2.6. For the stability measurements, the mass flow $\dot{m}$ is varied between 0 and 2 g/s for the HH, and between 0 and 5 g/s for the QW. Without damper, the stability of the first transversal mode depends on the sign of ν_0: if it is positive, the mode is linearly unstable, if it is negative, the mode is linearly stable. With damper, the
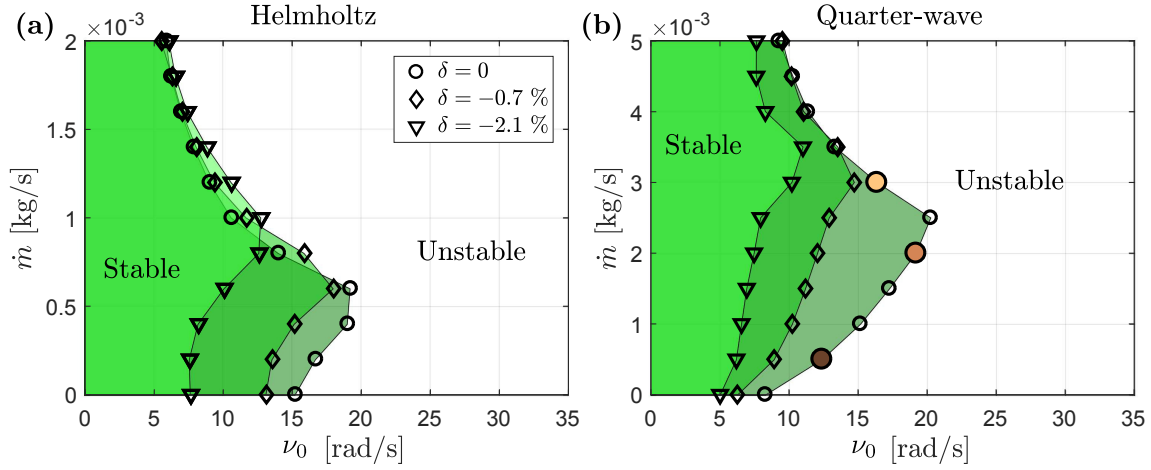
Figure 2.9: Experimental stability limits as function of purge mass flow $\dot{m}$ and mode growth rate ν_0 for the perfectly tuned case and two detuned cases with $\delta = (\omega_{H,Q} - \omega_0)/\omega_0 = -0.7$ and -2.1 %. **(a)** HH, **(b)** QW. The three colored points correspond to the fits in Figure 2.8**(c)**.

damping of the system is increased, and the stability limits change. These stability limits depend on the feedback loop gain c_1 and on the mass flow of the purge air going through the damper. The determination of these new limits is done as follows: for each tuned damper (HH and QW) and each mass flow, the gain c_1 is slowly ramped down, starting from a value where the system with dampers is linearly unstable and is on a limit cycle. The linear growth rate ν_0 is a linear function of c_1 as shown in Figure 2.8**(a)**, and the ramping down of c_1 is equivalent to a 1 rad/s decrease of ν_0 in 30 second. The decrease of the bifurcation parameter ν_0 is therefore quasi-steady and one can fit the corresponding acoustic envelope using a function that is proportional to $\sqrt{\nu_0}$. The origin of that fit is the bifurcation point, which defines the stability limit. The results of three of those measurements and the respective fits can be seen in Figure 2.8**(c)**. The error was estimated by doing a fit on the truncated acoustic envelope curve, starting from the part with the highest amplitude. As shown in Figure 2.8**(c)**, the confidence intervals are very small compared to the variation caused by mass flow variation.

The length of the back-volume of the HH and the length of the QW are then lengthened to obtain a detuning $\delta = (\omega_{H,Q} - \omega_0)/\omega_0 = -0.7$ and -2.1 %, and the measurements are repeated. The stability limits obtained by employing this procedure, for tuned and detuned dampers, are presented in Figure 2.9. As expected the zone of stability shrinks when the damper is detuned. Those results will be compared with the model later on.

The feedback gain c_1 is now fixed such that $\nu_0 = 7$ rad/s. The eigenvalues of the first transversal mode of the chamber-damper coupled system are determined as function of the purge mass flow going through the damper. Since all of those measurements take place inside the stable zone, the eigenvalues are obtained using sweep measurements as

26

done in Figure 2.7**(c)** and **(d)**.

When a damper with low damping is added to the cavity, mode splitting occurs. This was demonstrated experimentally in e.g. [102, 137, 141, 198]. In the detuned case, one mode is much closer to the stability limit than the other one, and dominates the frequency response of the transfer function. In that case, a 2nd order transfer function fit yields satisfactory results. In the tuned case however, both modes should have equal decay rates but different frequencies for low purge mass flow. This means that the experimental transfer function should be fitted by a 4th order transfer function to capture both modes correctly. In practice, however, since the mass flow through the damper also influences the end correction and thus the detuning of the damper, symmetric mode splitting can only be achieved at one particular mass flow as one can see in Figure 2.10 for the tuned QW. This is even worse for the HH, since it is much more prone to mass flow-induced detuning (see Figure 2.4**(a)**). Therefore, only a 2nd order transfer function is used to determine the poles of the transfer function in a systematic manner, accepting that this technique might lead to small errors around the mass flow for which symmetric mode splitting occurs.
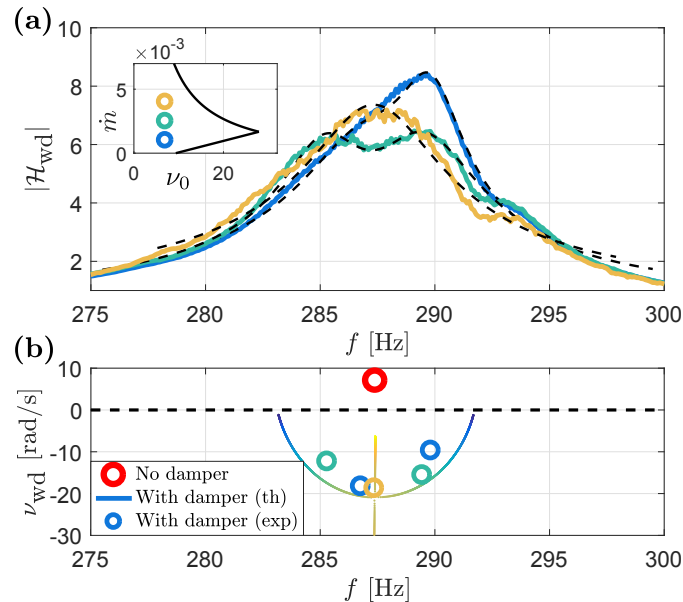

Figure 2.10: Evolution of the experimental spectrum **(a)** and of the corresponding roots **(b)** of the cavity with $\nu_0 = 7$ rad/s by addition of a tuned QW. Increasing the mass flow also influences the detuning (through the length correction) and the damper can only be tuned for a certain mass flow ($\dot{m} = 2.5$ g/s in this case).

The results of this fit compared with the predictions from the analytical model (which will be described in the next section) are shown in Fig 2.11 for both dampers, either tuned or slightly detuned ($\delta = -0.7$ %). As expected, the model is not accurate for the HH damper at low mass flows: a nonlinear dissipation term would be needed to

capture its behavior at low mass flow. The agreement between theory and experiments is otherwise good. Comparing HH and QW resonator, the HH damper achieves better stabilization for low mass flow than the QW for similar damper volume. The mass flow needed to achieve best stabilization is higher for the QW than for the HH. Even if both are used at their best mass flow condition, the HH damper achieves slightly better stabilization than the QW (which is also predicted by the model).
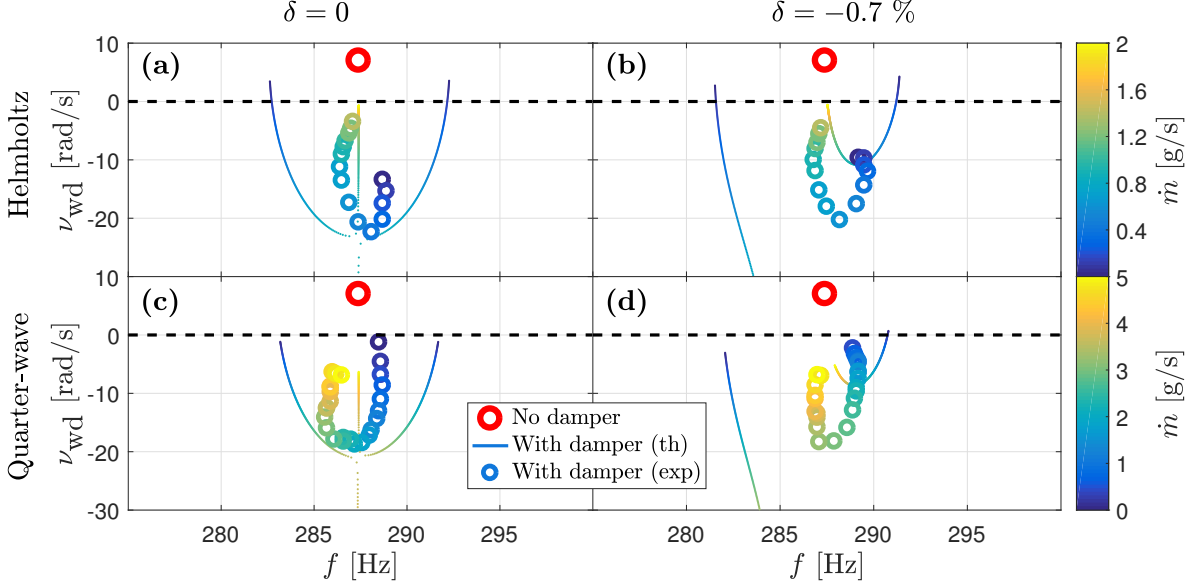

Figure 2.11: Evolution of an unstable eigenmode (red circle) of the cavity with $\nu_0 = 7$ rad/s by addition of dampers according to the model (continuous curve) and to the experiments (circles) for different mass flows (color scale) for the tuned **(a)** and detuned **(b)** Helmholtz resonator and for the tuned **(c)** and detuned **(d)** Quarter-Wave resonator.

2.4 Analytical model and optimal damping

2.4.1 Analytical model

The derivation of the model used for comparison with the experiments in Figs. 2.10 and 2.11 can be found in 2.6 based on the work of [132]. With a single dominant mode, the pressure in the chamber can be approximated by $p(t, \mathbf{x}) = \eta(t)\psi(\mathbf{x})$ with $\psi(\mathbf{x})$ the acoustic eigenmode and $\eta(t)$ its amplitude. The transfer function of the chamber-damper coupled system (Figure 2.12**(b)**) can be written in the HH case as follows:

$$\mathcal{H}_{\mathrm{wd}}(s) = \frac{\hat{\eta}(s)}{\hat{\mathcal{Q}}_N(s)} = \frac{-2\nu_0 s \left(s^2 + 2\alpha_H s + \omega_H^2\right)}{\left(s^2 - 2\nu_0 s + \omega_0^2\right)\left(s^2 + 2\alpha_H s + \omega_H^2\right) + s^2 \omega_H^2 \varepsilon_H^2}, \tag{2.18}$$

with $\hat{\mathcal{Q}}_N(s)$ the noise component of the acoustic source in the chamber volume, ω_0 the natural angular frequency of the dominant mode, ν_0 its growth/decay rate, ω_H the
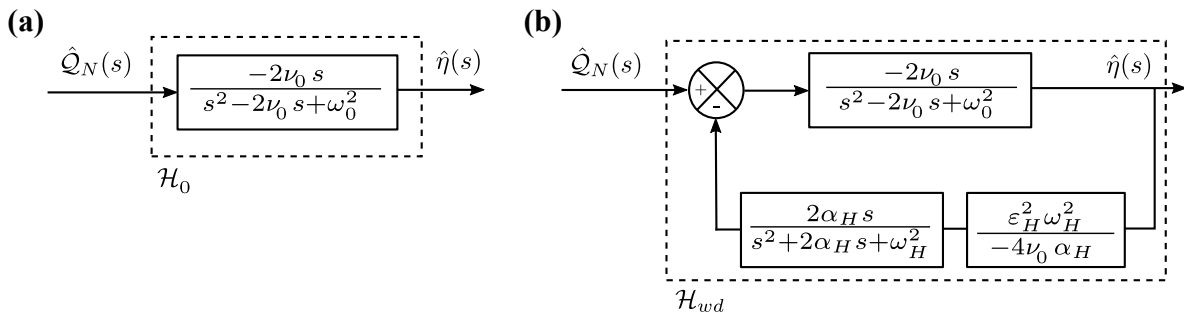
(a)

(b)

Figure 2.12: Block diagram representation of the system **(a)** without and **(b)** with HH dampers as in [132].

angular frequency of the damper and its damping $\alpha_H = R_H/2\rho_d l$ and R_H the resistive term from Eq. (2.3). ε_H is the damping efficiency factor defined as:

$$\varepsilon_H^2 = \frac{V_H}{V}\frac{\Psi_d}{\Lambda}, \qquad (2.19)$$

with V_H the back volume of one damper, V the chamber volume, Λ the norm of the mode and $\Psi_d = \sum_{k=1}^{n} \psi^2(\mathbf{x}_k)$ a non-dimensional number describing the number and location of the dampers with respect to the pressure antinode of the mode. If $\varepsilon_H = 0$, then $\mathcal{H}_{\text{wd}} = \mathcal{H}_0$ shown in Figure 2.12**(a)**. The equivalent expressions for the QW case ε_Q can be found in the Appendix. With one damper, Ψ_d simplifies to $\psi^2(\mathbf{x}_d) = \psi_d^2$. The previous description is equivalent to the following time domain formulation:

$$\begin{cases} \ddot{\eta} - 2\nu_0\dot{\eta} + \omega_0^2\eta = -\dfrac{\varepsilon_H^2\omega_H^2\rho l}{\psi_d}\dot{u} \\[3mm] \ddot{u} + 2\alpha_H\dot{u} + \omega_H^2 u = \dfrac{\psi_d}{\rho l}\dot{\eta}, \end{cases} \qquad (2.20)$$

with u the acoustic velocity in the damper neck. This system of two coupled ODEs can be expressed as:

$$\dot{X} = MX \quad \text{with} \quad M = \begin{bmatrix} 2\nu_0 & -\omega_0^2 & -\dfrac{\varepsilon_H^2\omega_H^2\rho l}{\psi_d} & 0 \\[3mm] 1 & 0 & 0 & 0 \\[3mm] \dfrac{\psi_d}{\rho l} & 0 & -2\alpha_H & -\omega_H^2 \\[3mm] 0 & 0 & 1 & 0 \end{bmatrix} \quad \text{and} \quad X = \begin{bmatrix} \dot{\eta} \\ \eta \\ \dot{u} \\ u \end{bmatrix}. \qquad (2.21)$$

2.4.2 Optimal damping and exceptional points

The analytical model presented in section 2.4.1 is now used to determine the linear stability of the coupled system "chamber-damper", which was experimentally investigated

in section 2.3. To that end, one uses the geometrical and flow parameters which characterize the acoustic mode, the dampers and the coupling efficiency in this experimental configuration:

- The first transversal mode of the cavity is considered, with $\omega_0 \simeq 1803$ rad/s, $f_0 = \omega_0/2\pi \simeq 287$ Hz. The electro-acoustic feedback allows to set ν_0 up to 35 rad/s.

- The experimentally-identified linear relationships $R_H(\dot{m})$ and $R_Q(\dot{m})$ presented in Figure 2.5 are used for the evaluation of the damping $2\alpha_H(\dot{m}) = R_H/\rho l$ and $2\alpha_Q(\dot{m}) = R_Q/\rho L$. The effective lengths $l = l_p + l_{\text{cor}}$ and $L = L_p + L_{\text{cor}}$, for dampers connected to the large chamber, are not the same as in section 2.2.2 where they were connected to a duct. Therefore, the end corrections are determined again using the Helmholtz solver AVSP, for the "chamber-damper" arrangement, which gives $l_{\text{cor}} = 15.9$ mm and $L_{\text{cor}} = 10.3$ mm. The physical length L (resp. L_p) is used for the tuning of the natural resonance frequency of the dampers ω_H (resp. ω_Q).

- The damping efficiency factors ε_H and ε_Q depend on the damper-to-chamber volume ratio, on the modal amplitude at the damper location and on the mode normalization factor. In the present configuration, $\Lambda = 1/2$ and $\psi = 0.95$ (see Figure 2.6).

The stability of the coupled system is obtained from Eq. (2.18) for the range of purge mass flow $\dot{m}$ and linear growth rate ν_0 which were used in the experiments. In the perfectly tuned case with $\omega_0 = \omega_H$, the stability limits of the coupled system for the HH damper case are explicitly obtained from the Routh-Hurwitz criterion:

$$
\begin{cases}
\alpha_H \geq \nu_0 & \text{RH1} \\[2mm]
\omega_0^2 \varepsilon_H^2 \geq 4\nu_0 \alpha_H & \text{RH2}
\end{cases}
\tag{2.22}
$$

The Routh-Hurwitz criterion can be easily translated as follows: the damping of the damper needs to be higher than the growth rate of the unstable mode, and the ratio weighting the feedback in the block diagram (Figure 2.12(b)) needs to be greater than 1. For the QW damper case, the Routh-Hurwitz criterion is the same, replacing α_H by α_Q and ε_H by ε_Q. For the detuned case, there is no analytical expression giving the linear stability boundaries. The stability limit is numerically determined by computing the poles of Eq. (2.18), and searching the change of sign of the real part of the least stable of these poles. The theoretical stability limits for tuned and detuned Helmholtz and Quarter-Wave dampers are presented in Figure 2.13 and are in good agreement with the ones measured experimentally (see Figure 2.9). The comparison between the theoretical stability limits of the tuned HH and tuned QW (having quasi-identical volume) are shown in Figure 2.14.
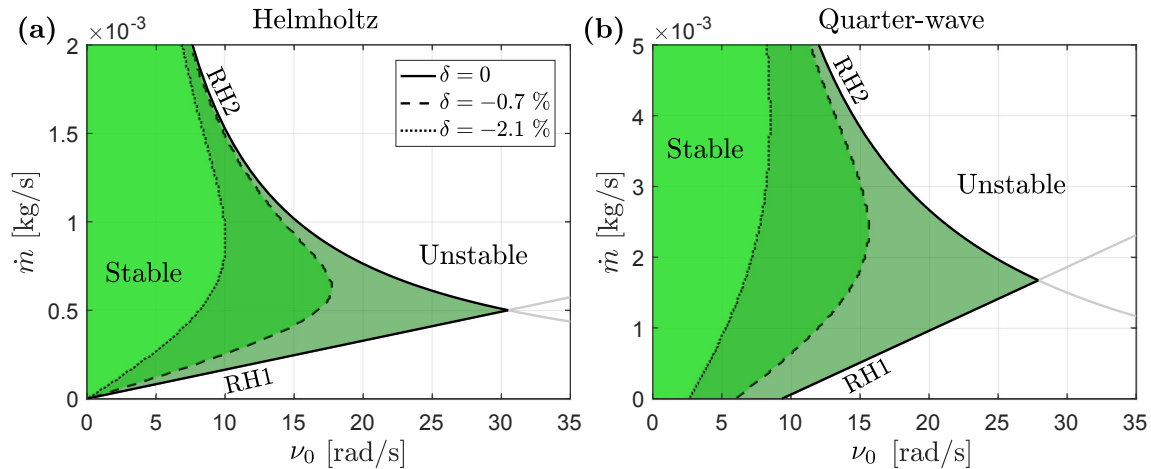
Figure 2.13: Theoretical stability limits as function of purge mass flow $\dot{m}$ and growth rate ν_0 for the perfectly tuned case (Routh-Hurwitz criterion, analytical) and two detuned cases (numerical) with $\delta = -0.7$ and -2.1 %. **(a)** HH, **(b)** QW.

Figure 2.15 shows the influence of increasing purge mass flow $\dot{m}$ on the magnitude and on the poles of the transfer function characterizing the coupled system "chamber-damper" for fixed $\nu_0 = 7$ rad/s. In both cases, the inset shows the coordinates $(\nu_0; \dot{m})$ in the stability diagram, which are considered for this analysis. For situations where the damper is tuned to the eigenfrequency of the system without dampers ($\omega_0 = \omega_H$ or $\omega_0 = \omega_Q$), the pair of eigenvalues of the system with damper merge at a so-called *exceptional point* (EP) [165], when a critical purge mass flow $\dot{m}_{EP}$ through the damper is reached. For $\dot{m} < \dot{m}_{EP}$, the poles of the system with the damper symmetrically split, with identical linear growth rate ν_{wd} and different frequencies $f_{wd} = f_0 \pm \Delta f$. The associated transient dynamics is a decay of the oscillation amplitude with time constant $1/\nu_{wd}$, which is accompanied with a low-frequency amplitude beating of period $1/\Delta f$ [155]. For $\dot{m} > \dot{m}_{EP}$, the pair of eigenvalues originating from the exceptional point exhibit the same frequency as the natural eigenfrequency of the system without damper ($\omega_{wd} = \omega_0$), but one of these eigenvalues has a larger linear growth rate ν_{wd} than the other and than the one at the EP, i.e. the associated eigenmode is less stable.

By increasing the purge mass flow, the best stabilization of the mode is therefore achieved when the eigenvalues and associated eigenmodes of the coupled system coalesce at the EP. This can be verified by computing the eigenvalues and eigenvectors of M in Eq. (2.21): the scalar product between the normalized eigenvectors e_1 and e_2 corresponding to positive frequency can be seen in Figure 2.16**(e)**. At the EP, the scalar product is 1, meaning that they coalesce. If one further increases the purge mass flow, the eigenvalues split into two separate modes at same frequency but different decay rates, one of them being stabilized and the other one destabilized by a further increase of the mass flow. Note that the mass flow giving the best mode stabilization is higher than the one minimizing the infinite norm of the frequency response. In the
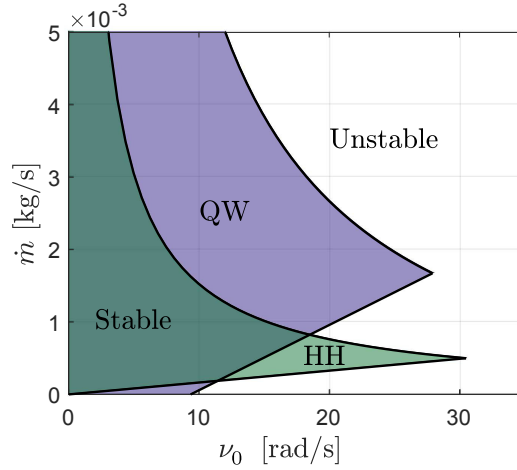
Figure 2.14: Comparison of the theoretical stability limits as function of purge mass flow $\dot{m}$ and growth rate ν_0 for the perfectly tuned case between HH and QW.

situation where the dampers are not well tuned (Figure 2.15(**b**) and 2.15(**d**)), there is an avoided crossing of the eigenvalues and the system does not exhibit any EP when the purge mass flow is varied. In the present configuration, a detuning of 0.7 % leads to a substantial root loci deviation and to an avoided crossing compared to the tuned damper scenario. The theoretical behavior presented in Figure 2.15 is again in good agreement with the experimental measurements shown in Figure 2.10 and Figure 2.11.

To complement this analysis, the eigenvalues $\lambda = \nu_{\text{wd}} + i\omega_{\text{wd}}$ of the coupled system "chamber-damper" are presented in the form of Riemann sheets as function of the damper detuning δ and of the damper purge mass flow $\dot{m}$ in Figure 2.16 for $\nu_0 = 7$ rad/s. In Figure 2.16(**c**), one can see that the EP is the point where the real part of the double root of the quartic polynomial [147] (denominator of Eq. (2.18)) is minimum. When $\omega_H = \omega_0$ (tuned damper), one can explicitly deduce the associated HH resonator damping:

$$\alpha_{H,\text{EP}} = \omega_0 \varepsilon_H - \nu_0. \tag{2.23}$$

Klaus and co-workers [92] recently drawn a similar result in the context of room acoustics. In that study, dissipative resonators are employed to minimize reverberation time, which means that, in contrast with the present work, the acoustic enclosure is already linearly stable before the implementation of the damper, which are used to further stabilize it. Here, the damping coefficient is linearly related to the mass flow through the damper and Eq. (2.23) corresponds to

$$\dot{m}_{\text{EP}}(\nu_0) = \frac{\rho a l}{\zeta_H}(2\omega_0 \varepsilon_H - 2\nu_0). \tag{2.24}$$

A similar expression can be derived for the QW damper and includes the acoustic boundary layer losses. The location of the EP in the linear stability diagram is shown
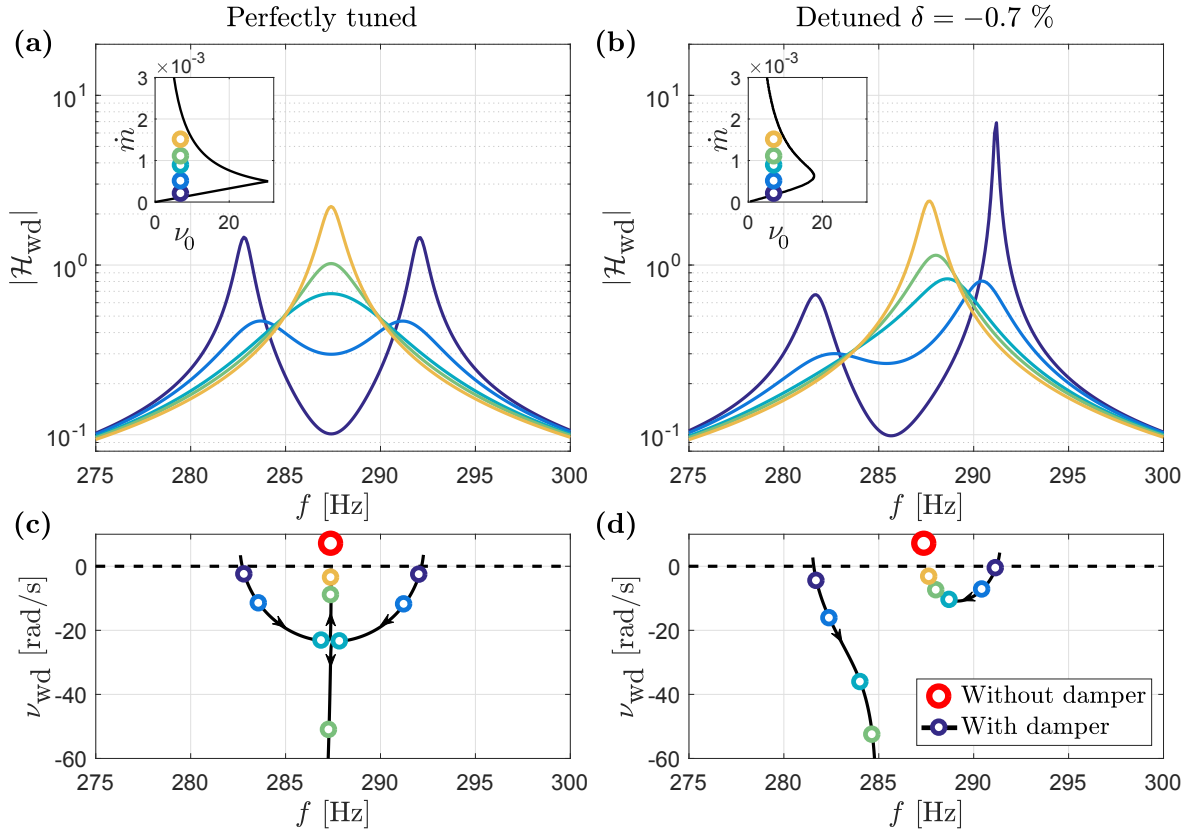
Figure 2.15: Influence of increasing mass flow on the magnitude (top) and on the poles (bottom) of the transfer function describing the coupled system "chamber-damper" for an unstable mode with $\nu_0 = 7$ rad/s and HH resonator. **(a)** and **(c)** tuned, **(b)** and **(d)** detuned. For the tuned case, the pair of eigenvalues coalesce at the exceptional point for a specific mass flow $\dot{m}$, which corresponds to the most linearly stable coupled system.

in Figure 2.17 as a dashed red line. The mass flow giving the best stabilization for detuned dampers is obtained numerically, and the results are shown in Figure 2.18. One can see that the slope of the lines indicating the maximum damping does not depend on the detuning.

For configurations with only one type of dampers, which can be a practical requirement in order to avoid having to manufacture, test and validate several geometries of dampers, the present work shows that the optimum damping is reached when the purge mass flow is adjusted close to the EP of the coupled system "chamber–dampers".

Combining dampers of different geometries, which address the same dominant acoustic mode, is also possible. In that case, the number of parameters in the system increases and the simple analytical expression given in Eq. (2.24) for the optimum damper mass flow cannot be used. Still, a numerical optimization could be performed to find the

mass flows for each of the dampers, which lead to the optimum modal damping.

Note that exceptional points exhibit an extreme sensitivity to parameter variation, which can be showed analytically. Let us note $D(s, \delta, \alpha_H)$ the polynomial corresponding to the denominator of Eq. (2.18), whose roots λ are the eigenvalues of the chamber-damper coupled system.

$$D(s, \delta, \alpha_H) = \left(s^2 - 2\nu_0 s + \omega_0^2\right)\left(s^2 + 2\alpha_H s + \omega_0^2(1 + \delta)^2\right) + s^2\omega_0^2(1 + \delta)^2\varepsilon_H^2. \quad (2.25)$$

At the EP, the eigenvalues are 2 complex conjugate double roots $\lambda_{\mathrm{EP}} = \nu_{\mathrm{wd,EP}} \pm i\,\omega_{\mathrm{wd,EP}}$. One can identify $D(s, 0, \alpha_{H,\mathrm{EP}}) = (s - \lambda_{\mathrm{EP}})^2(s - \lambda_{\mathrm{EP}}^*)^2$, with $\alpha_{H,\mathrm{EP}}$ from Eq. (2.23), giving

$$\nu_{\mathrm{wd,EP}} = \nu_0 - \frac{\omega_0\varepsilon_H}{2}, \qquad \omega_{\mathrm{wd,EP}} = \sqrt{\omega_0^2 - \nu_{\mathrm{wd,EP}}^2}. \quad (2.26)$$

Using Eqs. (2.25) and (2.26), one can show that the partial derivative of D with respect to s vanishes at the EP, i.e. $\partial_s D = 0$ for $s = \lambda_{\mathrm{EP}}$, $\delta = 0$, $\alpha_H = \alpha_{H,\mathrm{EP}}$. One can also get analytical expressions of the other partial derivatives around the EP as function of ω_0, ν_0 and ε_H. This gives the following Taylor expansion for a root λ of the polynomial D around the EP:

$$0 = D(\lambda, \delta, \alpha_H) = \frac{1}{2}(\lambda - \lambda_{\mathrm{EP}})^2 \left.\frac{\partial^2 D}{\partial s^2}\right|_{\mathrm{EP}} + \delta \left.\frac{\partial D}{\partial \delta}\right|_{\mathrm{EP}} + (\alpha_H - \alpha_{H,\mathrm{EP}}) \left.\frac{\partial D}{\partial \alpha_H}\right|_{\mathrm{EP}} + ... \quad (2.27)$$

With $\delta = 0$ the following approximation can be derived for a root λ around the EP:

$$\lambda \simeq \lambda_{\mathrm{EP}} + \left(2\frac{\partial_{\alpha_H} D(\lambda_{\mathrm{EP}}, 0, \alpha_{H,\mathrm{EP}})}{\partial_{ss} D(\lambda_{\mathrm{EP}}, 0, \alpha_{H,\mathrm{EP}})}\right)^{1/2} \sqrt{\alpha_H - \alpha_{H,\mathrm{EP}}} \quad (2.28)$$

Similarly, if $\alpha_H = \alpha_{H,\mathrm{EP}}$ the following approximation can be derived for a root λ around the EP:

$$\lambda \simeq \lambda_{\mathrm{EP}} + \left(2\frac{\partial_{\delta} D(\lambda_{\mathrm{EP}}, 0, \alpha_{H,\mathrm{EP}})}{\partial_{ss} D(\lambda_{\mathrm{EP}}, 0, \alpha_{H,\mathrm{EP}})}\right)^{1/2} \sqrt{\delta} \quad (2.29)$$

Eqs. (2.28) and (2.29) are Puiseux series [84, 164]. For Eq. (2.29), the sensitivity $d\lambda/d\delta \propto 1/\sqrt{\delta}$, which tends to infinity when $\delta \to 0$. A similar dependency can be found when $\alpha_H \to \alpha_{H,\mathrm{EP}}$, thus showing the infinite sensitivity to parameter variation around the EP.
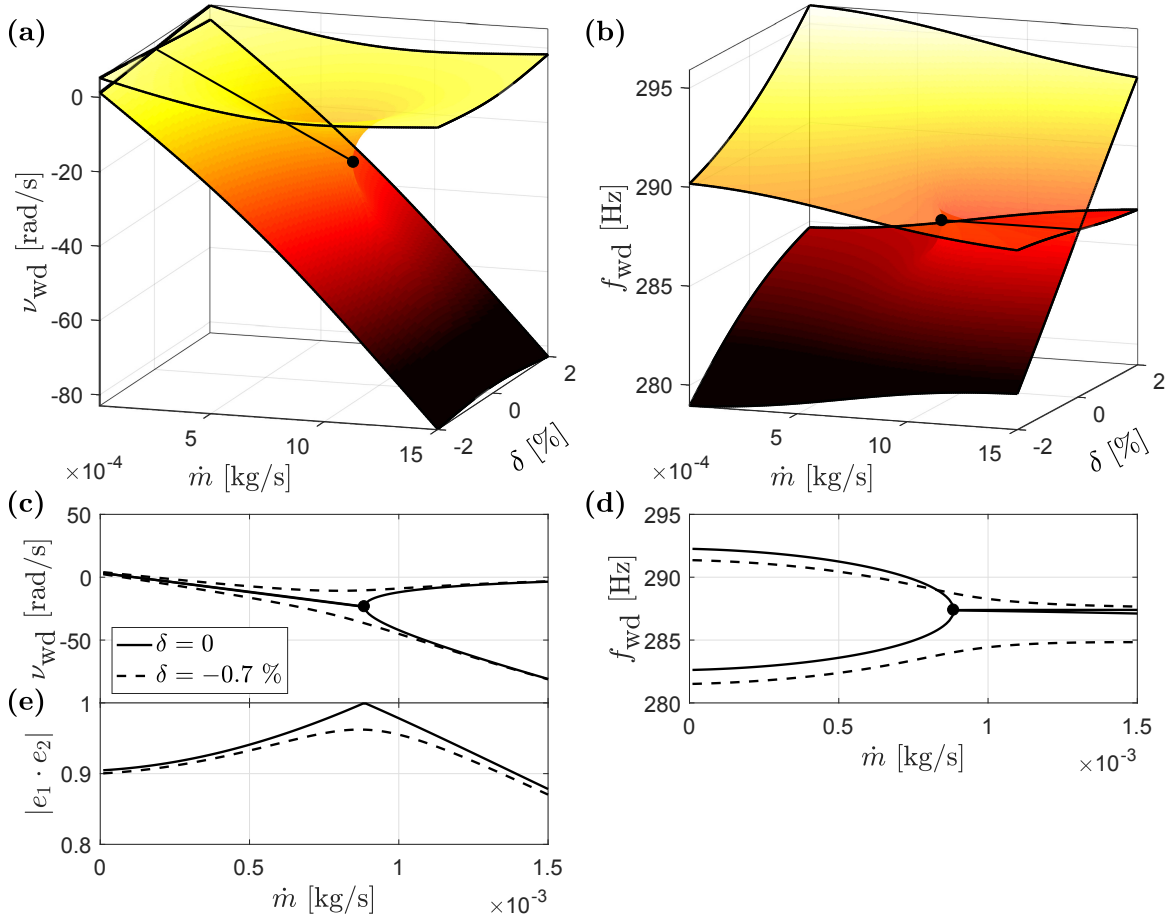
Figure 2.16: Loci of the coupled system eigenvalues around the EP for $\nu_0 = 7$ rad/s. **(a)** $\Re(\lambda) = \nu_{\mathrm{wd}}$ [rad/s] as function of purge mass flow $\dot{m}$ and detuning δ and **(c)** cuts of the surface for $\delta = 0$ and -2 Hz, **(b)** $\Im(\lambda)/2\pi = f_{\mathrm{wd}}$ [Hz] as function of purge mass flow $\dot{m}$ and detuning δ, **(d)** cuts of the surface for $\delta = 0$ and -0.7%. The EP is represented by the black dot. **(e)** Scalar product of the coupled system normalized eigenvectors e_1 and e_2, showing their coalescence at the EP.
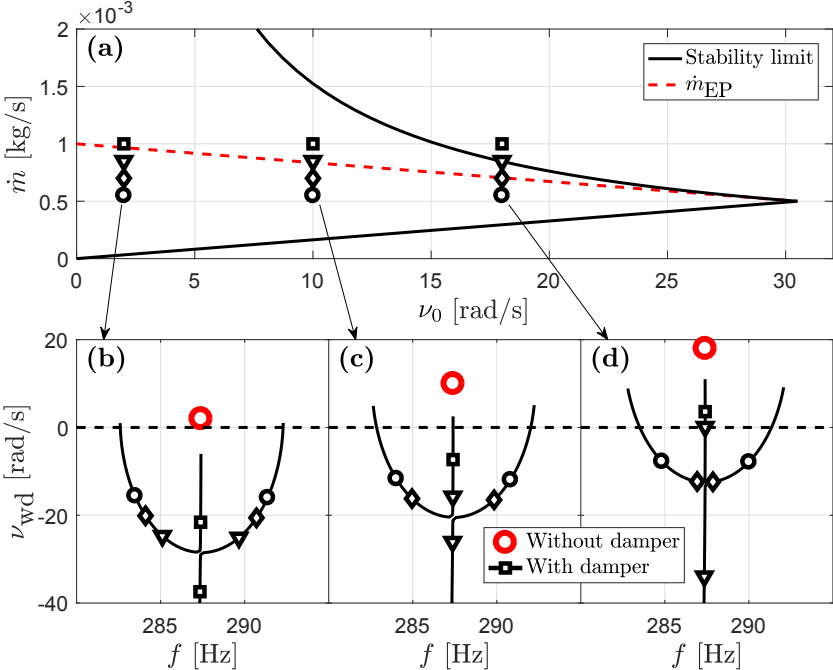
Figure 2.17: Influence of growth rate ν_0 on the mass flow $\dot{m}_{\text{EP}}$ at which the exceptional point (and thus the best stabilization) is achieved. The dashed red line corresponds to Eq. (2.24)
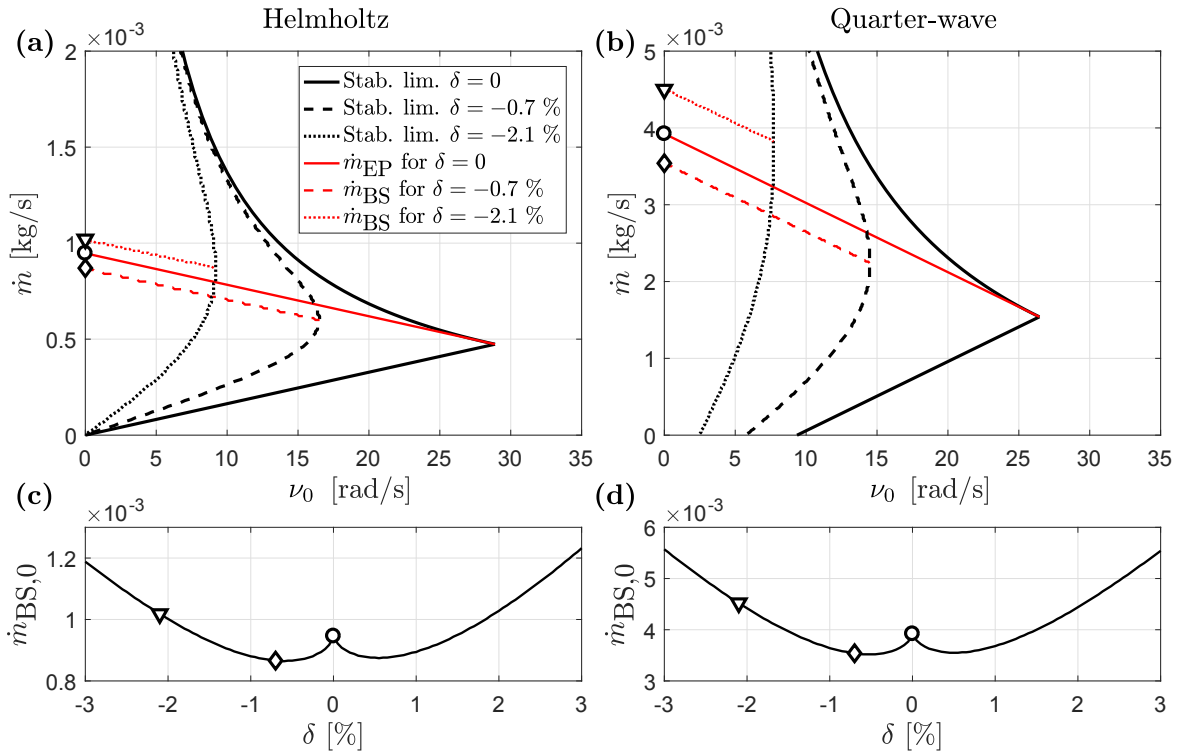
Figure 2.18: Influence of detuning on the mass flow giving best stabilization. **(a)** $\dot{m}_{BS}$ as a function of ν_0 within stability limit for 3 different detuning values. The plain red curve corresponds to $\dot{m}_{EP}$ (Eq. (2.24)) whereas the dashed and dotted red curves were obtained numerically. The slope stays the same but the y-intercept varies. **(c)** y-intercept of $\dot{m}_{BS}$ as a function of the detuning δ. **(b)** and **(d)**: same for the QW damper.

Pb A: Absorption maximization over surface   Pb B: Eigenmode stabilization in volume

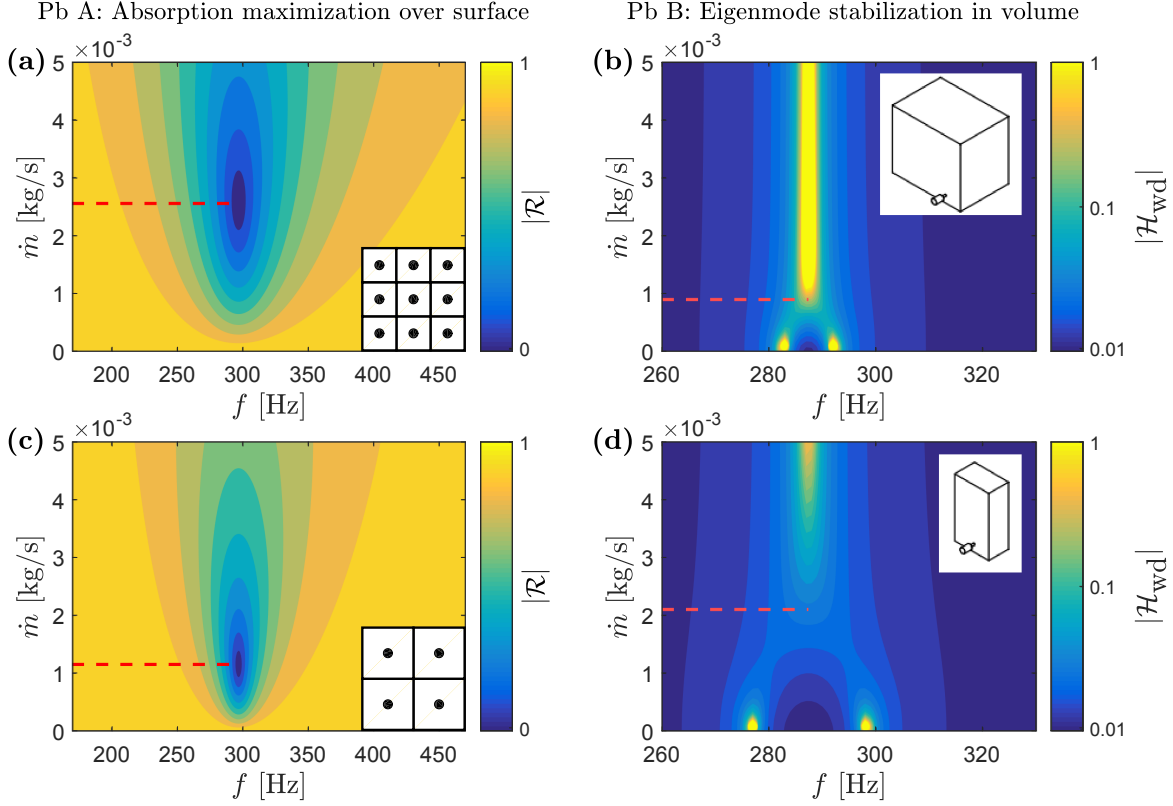Figure 2.19: For the exact same damper, comparison between reflection coefficient absolute value **(a)** for porosity $\sigma = 0.055$ and **(c)** for porosity $\sigma = 0.024$, and coupled damper-cavity spectrum **(b)** for efficiency factor $\varepsilon_H^2 = 0.0011$ ($V_c = 0.2$ m^3) and **(d)** for efficiency factor $\varepsilon_H^2 = 0.0056$ ($V_c = 0.041$ m^3)

2.5 Conclusion

The optimization of the damper purge mass flow has been done in two different setups throughout this chapter: either for minimizing the reflection coefficient at resonance in an impedance tube (section 2.2.2) or for achieving the best stabilization of an unstable eigenmode when the damper is coupled to a chamber (section 2.4.2). These two problems are very different as illustrated in Figure 2.19: Problem A consists of maximizing acoustic absorption per unit area, as was done in [75, 143, 156]. When identical dampers are distributed over a surface, the ideal purge mass flow per damper for best normal-incidence absorption depends on the number of dampers per unit area. When this purge mass flow is set, the acoustic resistance of the surface matches the characteristic impedance of the medium. In Figure 2.19**(a)** and 2.19**(c)**, which give the absolute value of the normal incidence reflection coefficient as in Figure 2.4, one can see that the optimum mass flow that leads to anechoic condition, is not the same whether 4 or 9 geometrically identical dampers are distributed over the same surface.

Problem B deals with the stabilization of an unstable mode in a chamber using damped resonators. The ideal mass flow for achieving the best stability margin does not depend on the density of dampers over the surface enclosing the cavity, but on the volume ratio between the cavity and the dampers. In 2.19**(b)** and 2.19**(d)**, the EP obtained by the connection of a tuned HH resonator to a cavity is not obtained at the same mass flow, when the cavity-to-damper volume ratio is changed. Note also that, although the HH dampers considered for this illustration feature the same geometry as the ones used to clarify Problem A, these mass flow differ from the ones giving anechoic condition in 2.19**(a)** and 2.19**(c)**. This is due to the fact that the optimization problem is not the same in the two cases: in the first one, one tries to minimize the reflection coefficient of a surface; in the second one, one tries to minimize the real part of the eigenvalues of the coupled system "chamber-damper".

In this chapter, the damping properties of HH and QW resonators have been investigated. A new linear model for the QW damper impedance has been derived and validated using reflection coefficient measurements. A coupled chamber-damper experiment was set up in order to measure the stability limits of the coupled system for both types of dampers. The damping capabilities of these dampers have been compared theoretically and experimentally: for comparable volume, the QW damper requires a higher mass flow both for minimizing the reflection coefficient (for which it provides damping in a narrower frequency band as the HH) and for optimizing the stabilization of an acoustic eigenmode. The HH damper is more prone to detuning but also provides better stabilization at very low purge mass flow than a QW damper featuring the same volume. The experiments also allowed the validation of the analytical model describing the coupled system. It was demonstrated that the best damping is achieved at the exceptional point of the coupled system, obtained for tuned dampers and for a critical mass flow whose expression is given as function of the key parameters of the system.

2.6 Appendix: Derivation of the analytical model

The problem of coupled cavities has been the topic of numerous studies, which are based on the model given in chapter 10.4 of the book of Morse and Ingard [122]. In the present case, one of the cavities (the chamber) is much larger than the others (the dissipative resonators). One can for instance refer to the work of Fahy and Schofield [55], who derived a model to predict the increase of modal damping induced by a single damper. Cummings [38] and Li and Cheng [101] adapted the model to a dissipative resonator array. Doria [45] studied the effect of the damper on the mode shape and the influence of different volume ratios between chamber and damper. Subsequent studies extended the use of the model to cavities exhibiting linearly unstable thermoacoustic modes [7,132]. Following the same approach, the pressure in the chamber is expressed as a Galerkin

expansion using the orthonormal basis $\boldsymbol{\psi}$ composed of the natural acoustic eigenmodes:

$$p(t, \mathbf{x}) = \sum_{i=1}^{\infty} \eta_i(t) \psi_i(\mathbf{x}), \tag{2.30}$$

with $\psi_i(\mathbf{x})$ the natural eigenmodes and $\eta_i(t)$ their amplitude. Assuming that the chamber is equipped with dampers and that, under the effect of a field dependent volumetric source, the pressure field is dominated by one of these modes, the contribution from the other modes can be neglected and one can express the amplitude of that mode in the frequency domain as [132]:

$$\hat{\eta}(s) = \frac{s \rho_c c_c^2}{s^2 + \omega_0^2} \frac{1}{V \Lambda} \left(\frac{\gamma - 1}{\rho_c c_c^2} \int_V (\hat{Q}_C(s) + \hat{Q}_N(s)) \psi^*(\mathbf{x}) dV - \int_{S_d} \hat{\eta}(s) \frac{|\psi(\mathbf{x})|^2}{Z_d(\mathbf{x}, s)} dS \right.$$
$$\left. - \int_{S-S_d} \hat{\eta}(s) \frac{|\psi(\mathbf{x})|^2}{Z(\mathbf{x}, s)} dS \right). \tag{2.31}$$

In this formula, ρ_c is the air density in the chamber, c_c the speed of sound in the chamber, γ the heat capacity ratio, V the volume of the chamber, ω_0 the natural angular frequency of the dominant mode ψ and Λ its norm defined as

$$\Lambda = \frac{1}{V} \int_V |\psi|^2 dV, \tag{2.32}$$

$\hat{Q}_C$ is the *coherent* component of the volumetric source, in the sense that it depends on the acoustic field and therefore on $\hat{\eta}$, while $\hat{Q}_N$ is the *noisy* component of the volumetric source which does not depend on the acoustic field, and which acts as a broadband acoustic forcing; S_d is the area of the chamber walls which is equipped with dampers; $Z_d(\mathbf{x}, s) = \hat{\eta}(s) \psi(\mathbf{x}) / \hat{u}(s)$ is the impedance of the dampers and $Z(\mathbf{x}, s)$ is the impedance of the chamber walls. In combustion chambers, thermoacoustic instabilities result from the constructive interaction between the coherent component of the unsteady heat release rate of the flames Q_C, and the acoustic field η. When the acoustic energy produced by the coherent volumetric source exceeds the dissipation at the boundaries, the thermoacoustic system is linearly unstable. Considering Eq. (2.31) in the situation where there are no dampers ($S_d = 0$), one can express the transfer function which links the modal amplitude to the broadband forcing

$$\mathcal{H}_0(s) = \frac{\hat{\eta}(s)}{\hat{\mathcal{Q}}_N(s)} = \frac{-2\nu_0 s}{s^2 - 2\nu_0 s + \omega_0^2}, \tag{2.33}$$

where the subscript "wod" stands for "without dampers", and where

$$\hat{\mathcal{Q}}_N(s) = \frac{\gamma - 1}{-2\nu_0 V \Lambda} \int_V \hat{Q}_N(s) \psi^*(\mathbf{x}) dV \tag{2.34}$$

is the normalized broadband component of volumetric forcing weighted by the mode shape. $\nu_0 = \beta - \alpha$ is the linear growth/decay rate of the thermoacoustic system that

results from the balance between the linear contribution of the source term β (which depends on the gain and delay between coherent component of the volumetric source Q_C and pressure $\hat{\eta}$ [37]) and the natural linear damping of the mode α, which results from the impedance at the boundary (last integral in Eq. (2.31)). The case where n identical HH dampers are coupled to this chamber is now considered. Assuming that the neck of the dampers is compact with respect to the wavelength $2\pi c_c/\omega_0$, the second integral in Eq. (2.31) can be rewritten as

$$\sum_{k=1}^{n} \frac{a\psi^2(\mathbf{x}_k)}{Z_H}\hat{\eta}(s), \qquad (2.35)$$

where a is the cross-section of the neck of the dampers and $\mathbf{x}_k$ is the location of the kth damper. With $\Psi_d = \sum_{k=1}^{n} \psi^2(\mathbf{x}_k)$ and with the expression of the HH damper impedance

$$Z_H = \rho_d l \frac{s^2 + 2\alpha_H s + \omega_H^2}{s}. \qquad (2.36)$$

One can rearrange Eq. (2.31) as

$$\hat{\eta}(s) = \mathcal{H}_0\hat{\mathcal{Q}}_N(s) - \mathcal{H}_0 \frac{\rho_c c_c^2}{\rho_d c_d^2} \underbrace{\frac{AL\Psi_d}{V\Lambda}}_{\varepsilon_H^2} \underbrace{\frac{c_d^2 a}{ALl}}_{\omega_H^2} \frac{1}{-2\nu_0 2\alpha_H} \frac{2\alpha_H s}{s^2 + 2\alpha_H s + \omega_H^2}\hat{\eta}(s), \qquad (2.37)$$

with $2\alpha_H = R_H/\rho_d l$ and R_H the resistive term from Eq. (2.3). Considering that the pressure drop across the damper neck is small ($\bar{p}_c \approx \bar{p}_d$), one has $\rho_d c_d^2 = \gamma\bar{p}_d \approx \gamma\bar{p}_c = \rho_c c_c^2$, and one can write the transfer function which links the modal amplitude to the broadband forcing, when the chamber is equipped "with dampers":

$$\mathcal{H}_{\text{wd}}(s) = \frac{\hat{\eta}(s)}{\hat{\mathcal{Q}}_N(s)} = \frac{-2\nu_0 s\left(s^2 + 2\alpha_H s + \omega_H^2\right)}{\left(s^2 - 2\nu_0 s + \omega_0^2\right)\left(s^2 + 2\alpha_H s + \omega_H^2\right) + s^2\omega_H^2\varepsilon_H^2}. \qquad (2.38)$$

In this expression, ε_H is the damping efficiency factor. If $\varepsilon_H = 0$, then $\mathcal{H}_{\text{wd}} = \mathcal{H}_0$. In fact, the damping efficiency factor is a mode-shape weighted dampers-to-chamber volume ratio

$$\varepsilon_H^2 = \frac{V_H}{V}\frac{\Psi_d}{\Lambda} \qquad (2.39)$$

with $V_H = A_H L_H$ the back volume of one damper. For instance, if all the n dampers are placed at antinodes where $\psi = 1$, then $\Psi_d = n$ and $\varepsilon_H^2 = nV_H/V\Lambda$ where one clearly sees the ratio between overall damping volume nV_H and chamber volume V. It shows that large ε_H are achieved for large damping volume, with dampers at antinodes. In the case of the addition of n identical QW dampers, replacing a by A and Z_H by Z_Q from Eq. (2.14) and multiplying numerator and denominator by $L \cdot 4/\pi^2$ yields the same transfer function as Eqs. (2.18) and (2.38) with subscripts "H" replaced by "Q", with $2\alpha_Q = 2R_Q/\rho L$ (R_Q is the QW damper resistance given at Eq. (2.13)) and with

$$\varepsilon_Q^2 = \frac{8}{\pi^2}\left(1 + \frac{L_{\text{cor}}}{L_p}\right)\frac{V_Q}{V}\frac{\Psi_d}{\Lambda}, \qquad (2.40)$$

41

where $V_Q = AL_p$. The transfer function of the system without (Eq. (2.33)) and with (Eq. (2.18)) dampers are represented as block diagrams in Figure 2.12.

Note that this model, covering the coupling of one or multiple dampers of same geometry to the cavity, can be extended to include dampers of different geometries. Assuming we have N different damper geometries, Eq. (2.37) can be rewritten:

$$\hat{\eta}(s) = \mathcal{H}_0 \hat{\mathcal{Q}}_N(s) - \mathcal{H}_0 \sum_{i=1}^{N} \frac{\rho_c c_c^2}{\rho_i c_i^2} \varepsilon_i^2 \omega_i^2 \frac{1}{-2\nu_0 2\alpha_i} \frac{2\alpha_i s}{s^2 + 2\alpha_i s + \omega_i^2} \hat{\eta}(s), \qquad (2.41)$$

with ρ_i, c_i, α_i, ω_i the air density and speed of sound inside the damper i, as well as its damping and natural resonance frequency. The damping efficiency factor ε_i is defined as in Eqs. (2.39) or (2.40), depending on the damper type. Under the same assumption as above that $\rho_i c_i^2 \approx \rho_c c_c^2$, this gives the following the transfer function:

$$\frac{\hat{\eta}(s)}{\hat{\mathcal{Q}}_N(s)} = \frac{-2\nu_0 s \prod_{i=1}^{N} \left(s^2 + 2\alpha_i s + \omega_i^2\right)}{\left(s^2 - 2\nu_0 s + \omega_0^2\right) \prod_{i=1}^{N} \left(s^2 + 2\alpha_i s + \omega_i^2\right) + \sum_{i=1}^{N} \varepsilon_i^2 \omega_i^2 s^2 \prod_{j \neq i} \left(s^2 + 2\alpha_j s + \omega_j^2\right)}. \qquad (2.42)$$

For example for $N = 2$, the characteristic polynomial of the system reads:

$$\left(s^2 - 2\nu_0 s + \omega_0^2\right) \left(s^2 + 2\alpha_1 s + \omega_1^2\right) \left(s^2 + 2\alpha_2 s + \omega_2^2\right) + \varepsilon_1^2 \omega_1^2 s^2 \left(s^2 + 2\alpha_2 s + \omega_2^2\right) + \varepsilon_2^2 \omega_2^2 s^2 \left(s^2 + 2\alpha_1 s + \omega_1^2\right), \qquad (2.43)$$

allowing for linear stability and eigenvalue analysis, in order to determine parameters achieving best stabilization.

Chapter 3

Stability and limit cycles of a nonlinear damper acting on a linearly unstable thermoacoustic mode

This chapter builds up on the linear study in the previous chapter, introducing nonlinearities into the system. It aims at providing an overview of the dynamics of the associated limit cycles using a simple analytical model, where a perfectly tuned Helmholtz damper is coupled to the chamber featuring an unstable mode. The damper, crossed by a purge flow in order to prevent hot gas ingestion, is modeled as a non-linearly damped harmonic oscillator, with vortex shedding as the main dissipation mechanism. The combustion chamber featuring a linearly unstable thermoacoustic mode is modelled as a Van der Pol oscillator. The fixed points of the coupled system and their stability can be determined by analyzing the averaged amplitude equations. This allows the computation of the limit cycle amplitudes as function of the growth rate of the unstable mode and the mean velocity through the damper neck. Time-domain simulations of the coupled ODEs system are also performed and compared to the analytical predictions. Finally, experiments are performed using the same setup as in the previous chapter, where the thermoacoustic instability resulting from the interaction between heat release and acoustic pressure is mimicked by an electro-acoustic feedback loop. The stabilization capabilities of the damper and the amplitude of the limit cycle in the unstable cases are compared between the experiments and the analytical and numerical predictions, underlining the potentially dangerous hysteretic behavior of the system which should be taken into account for real engine cases.

This chapter is based on the research article *Stability and Limit Cycles of a Nonlinear Damper Acting on a Linearly Unstable Thermoacoustic Mode* by Claire Bourquard and Nicolas Noiray published in the Journal of Engineering for Gas Turbines and Power **141 (5)**, 051012 (2019).

3.1 Introduction

Over the last decades, the ever more stringent regulations on pollutant emissions have forced gas turbines manufacturers to design turbomachinery capable of running under leaner and leaner conditions. However, this lean combustion mode makes the combustor more prone to thermoacoustic instabilities, occuring when the fluctuating heat release from the flame interacts in a constructive way with the acoustic pressure field. The limit cycles of such thermoacoustic instabilities have been the topic of multiple studies [85, 105, 174, 175].

The suppression of thermoacoustic instabilities can be achieved by adding passive damping devices such as Helmholtz resonators to the combustion chamber [8,17,47,202], but in practical system the determination of the ideal damper location can be quite challenging [116]. Using a linear model, the evolution of the stability limits [58, 132, 199] and limit cycle amplitudes [27] of the system equipped with dampers has been studied. This model, using a linear dissipation term depending on the mean velocity of the purge flow going through the damper, is justified since dissipation occurs mostly because of vortex shedding at the damper exit [69, 181]. However, if the acoustic pressure in front of the damper exceeds a threshold, the flow may reverse during part of the acoustic cycle, which then requires nonlinear modeling of the damping term.

The nonlinear behavior of a Helmholtz damper has been studied on multiple occasions in the frame of damper impedance modeling, either with resistance depending only on amplitude [8,86,208], or adding a dependence on frequency in the model [59,69,169,186]. A study by Park and Sohn [136] investigated the damping of a cavity mode with a half-wave resonator at high amplitudes using numerical simulations.

To our knowledge, however, the influence of the Helmholtz resonator damping term nonlinearity on the stability of an acoustic mode has not been yet thoroughly investigated and is the topic of the present chapter. This is of utmost importance since the nonlinear damping term might lead to non-monotonic behavior such as sudden jumps to high-amplitude limit cycles, which can be dangerous for the machine integrity during ramping between operating points. In practice, reverse flow might lead to hot gas ingestion [32, 33] and thus detuning of the damper. The damper behavior can also be influenced by some other temperature or density difference between the damper and the chamber [19,194]. In the present chapter, however, only the influence of the damping nonlinearity is studied, and the damper is assumed to stay perfectly tuned at all conditions.

In a first part the analytical model is derived: the thermoacoustic instability is modelled as a Van der Pol oscillator, while the above-mentioned nonlinear damping model is used for the resonator. Coupled differential equations are derived and averaged to obtain the theoretical limit cycle amplitudes for the perfectly tuned case. The next section introduces the experimental setup, consisting of a parallelepipedic chamber where the thermoacoustic instability is mimicked by an electro-acoustic feedback loop, to which a Helmholtz resonator can be added. The growth rate of the electro-acoustic instability as well as the purge flow velocity through the damper can be controlled. The results of the analytical predictions and the experiments, as well as results of Simulink simulations of the coupled equations are compared in the last section.

3.2 Analytical Model

3.2.1 Derivation of the coupled equations

For the derivation of a linear model for the coupling between a damper and an enclosure, we start from Eq. (2.31) from section 2.6, where the noisy component of the unsteady heat release is neglected, and where the coherent component is simply written as Q:

$$
\begin{aligned}
\hat{\eta}(s) = \frac{s\rho c^2}{s^2 + \omega_0^2} \frac{1}{V\Lambda} & \left(\frac{\gamma - 1}{\rho c^2} \int_V \hat{Q}(s)\psi_d^*(\mathbf{x})dV \right. \\
& \left. - \int_{S-S_d} \hat{\eta}(s)\frac{|\psi_d(\mathbf{x})|^2}{Z(s)}dS - \int_{S_d} \hat{\eta}(s)\frac{|\psi_d(\mathbf{x_d})|^2}{Z_d(s)}dS \right),
\end{aligned}
\tag{3.1}
$$

with s the Laplace variable, ρ the air density, c the speed of sound in the chamber, V the chamber volume, S_d the wall surface equipped with dampers, Z_d the damper impedance, γ the specific heat ratio, $\hat{Q}$ the volumetric source term and Λ the spatial norm of the mode defined as in Eq. (2.32) from section 2.6. The second integral in Eq. (2.31) corresponds to the energy flux through the chamber walls and can be modelled by a damping term $2\alpha s\hat{\eta}$, with $\alpha > 0$ the natural linear damping of the chamber. The first integral, corresponding to the source term, can be similarly modelled by $ne^{-i\omega_0\tau}s\hat{\eta}$, with n the gain and τ the delay between source term and pressure. The linear contribution of the feedback loop to the growth/decay corresponds to the real part of this term $2\beta = n\cos(\omega_0\tau)$, which can be either positive or negative. One can then define the growth rate ν such that $\nu = \beta - \alpha$. In the present case, a single damper is used. Its geometry is described in Figure 3.1. Using the assumption that the neck diameter is compact with respect to the wavelength, one can assume all quantities to be constant in the third integral. Those simplifications yield:

$$
\hat{\eta}(s) = -\frac{s\rho c^2}{s^2 - 2\nu s + \omega_0^2} \frac{S_d\hat{\eta}(s)|\psi_d(\mathbf{x_d})|^2}{V\Lambda Z_d}.
\tag{3.2}
$$

Multiplying numerator and denominator by the damper back volume V_H and the neck length l (end corrections included), using $S_d = a$ to make the damper resonance frequency $\omega_d = c\sqrt{a/V_H l}$ appear, substituting the damper impedance Z_d by

$\hat{p}/\hat{u}_d = \hat{\eta}\psi_d(\mathbf{x_d})/\hat{u}_d$ (with $\hat{u}_d$ the acoustic velocity pointing inside the damper), rearranging the terms and switching back to time domain yields our first coupled equation:

$$\ddot{\eta} - 2\nu\dot{\eta} + \omega_0^2\eta = -\frac{\varepsilon_H^2\omega_d^2\rho l}{\psi_d}\dot{u}_d, \tag{3.3}$$

For ease of notation one defines $\psi_d = \psi_d(\mathbf{x_d})$ which describes the maximum mode amplitude at damper location and ε_H^2 a damping efficiency factor, depending on the volume ratio and the damper location defined as:

$$\varepsilon_H^2 = \frac{V_H}{V}\frac{\psi_d^2}{\Lambda} \tag{3.4}$$

With such a model, the pressure amplitude would theoretically grow indefinitely. In practice, however, nonlinear effects stabilize the pressure amplitude to a certain value describing a limit cycle. The minimum order model which can be used to describe such a saturation is the Van der Pol oscillator which will be used in this chapter. This model can represent any nonlinearity that is reasonably approximated by a fourth order Taylor expansion, since the even order terms vanish when the averaging is performed. The nonlinearities are then simply modelled by a cubic saturation [130], giving:

$$\ddot{\eta} - (2\nu + \kappa\eta^2)\dot{\eta} + \omega_0^2\eta = -\frac{\varepsilon_H^2\omega_d^2\rho l}{\psi_d}\dot{u}_d. \tag{3.5}$$
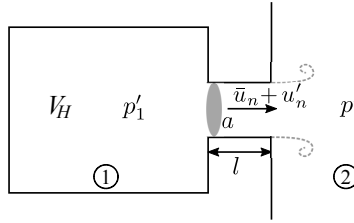

Figure 3.1: Sketch of a Helmholtz resonator with dimensions. For simplicity the neck length is simply labeled "l" but the model includes an end correction on both sides of the neck

The second coupled equation of the system is now derived using the sketch in Figure 3.1. One starts with the momentum equation along a streamline through the damper neck separating between mean and fluctuating quantities for velocity $u = \bar{u} + u'$ and pressure $p = \bar{p} + p'$:

$$\rho\frac{\partial u'}{\partial t} + \frac{1}{2}\rho\frac{\partial(\bar{u} + u')^2}{\partial x} + \frac{\partial(\bar{p} + p')}{\partial x} = 0 \tag{3.6}$$

One integrates in space from (1) to (2), using the neck length compactness (which means u'_n is constant throughout the neck):

$$\frac{1}{2}\rho(\bar{u}_1 + u'_1)^2 + \bar{p}_1 + p'_1 = \rho l\frac{du'_n}{dt} + \frac{1}{2}\rho(\bar{u}_2 + u'_2)^2 + \bar{p}_2 + p'_2, \tag{3.7}$$

with l the neck length with end corrections. Using the fact that mean quantities verify the Bernoulli equation and deriving with respect to time yields:

$$\rho(\bar{u}_1 + u'_1)\dot{u}'_1 + \dot{p}'_1 = \rho l\ddot{u}'_n + \rho(\bar{u}_2 + u'_2)\dot{u}'_2 + \dot{p}'_2 \tag{3.8}$$

Since some part of the acoustic energy is dissipated in vortex shedding when a jet occurs as in Figure 3.1, the difference between the first order derivative velocity terms on both sides is modelled by introducing a pressure loss coefficient ζ_H: if $\bar{u}_n + u'_n > 0$ the jet occurs on the right side which is where pressure loss occurs:

$$\dot{p}'_1 = \rho l\ddot{u}'_n + \rho\zeta_H(\bar{u}_n + u'_n)\dot{u}'_n + \dot{p}'_2 \tag{3.9}$$

Whereas if $\bar{u}_n + u'_n < 0$ the jet occurs on the left side:

$$\rho\zeta_H(\bar{u}_n + u'_n)\dot{u}'_n + \dot{p}'_1 = \rho l\ddot{u}'_n + \dot{p}'_2 \tag{3.10}$$

In addition, using the mass conservation and the equation of state in the volume gives $\dot{p}'_1 = -(\rho c^2 a/V_H)u'_n$ and using the fact that $\dot{p}'_2 = \psi_d\dot{\eta}$ gives for the whole cycle:

$$\ddot{u}'_n + \frac{\zeta_H}{l}|\bar{u}_n + u'_n|\dot{u}'_n + \omega_d^2 u'_n = -\frac{\psi_d}{\rho l}\dot{\eta} \tag{3.11}$$

3.2.2 Averaging and amplitude equations

For ease of notation one defines the acoustic velocity in the neck as $u = u_d = -u'_n$. The system of coupled equations is therefore:

$$\begin{cases} \ddot{\eta} - (2\nu + \kappa\eta^2)\dot{\eta} + \omega_0^2\eta = -\dfrac{\varepsilon_H^2\omega_d^2\rho l}{\psi_d}\dot{u} & \kappa < 0 \\[4mm] \ddot{u} + \dfrac{\zeta_H}{l}|\bar{u} + u|\dot{u} + \omega_d^2 u = \dfrac{\psi_d}{\rho l}\dot{\eta} & \zeta_H > 0, \end{cases} \tag{3.12}$$

This is a system of two nonlinear oscillators with linear resistive coupling. The 1$^{\text{st}}$ oscillator is a Van der Pol oscillator corresponding to self-sustained acoustic oscillations. The 2$^{\text{nd}}$ oscillator is a stable nonlinearly damped harmonic oscillator, excited by the derivative of the pressure in front of the damper divided by the mass of air in the damper neck per unit area. As a summary, the main assumptions that were done to derive the equations are the following:

1. Single dominant mode

2. A cubic saturation accurately represents the nonlinearities

3. Neck diameter and length are compact with respect to the mode wavelength

4. Dissipation in the damper is only due to vortex shedding and can thus be represented with a pressure loss coefficient ζ_H

3.2. Analytical Model

Following the averaging technique in [5,176], oscillations are assumed at a frequency ω unknown but with $\omega \simeq \omega_0 \simeq \omega_d$ and $\omega_0 + \omega_d \simeq 2\omega$. The ansatz is:

$$\begin{cases} \eta = A\cos(\omega t + \varphi_A) = \dfrac{1}{2}(ae^{i\omega t} + a^* e^{-i\omega t}) & a = Ae^{i\varphi_A} \\[3mm] u = B\cos(\omega t + \varphi_B) = \dfrac{1}{2}(be^{i\omega t} + b^* e^{-i\omega t}) & b = Be^{i\varphi_B} \end{cases}$$

(3.13)

The first order derivative is:

$$\dot{\eta} = \frac{i\omega}{2}(ae^{i\omega t} - a^* e^{-i\omega t}) \quad \text{assuming} \quad \dot{a}e^{i\omega t} + \dot{a}^* e^{-i\omega t} = 0$$

(3.14)

$$\text{Then} \quad \ddot{\eta} = i\omega\dot{a}e^{i\omega t} - \frac{\omega^2}{2}(ae^{i\omega t} + a^* e^{-i\omega t})$$

A similar sequence is used for u and b. Substituting into the first line of Eq. (3.12), multiplying by $e^{-i\omega t}/i\omega$, simplifying, integrating over one cycle, substituting a, b and $\dot{a}$, dividing by $e^{i\varphi_A}$ and taking the real and imaginary part of the equation yields:

$$\begin{cases} \dot{A} = \nu A + \dfrac{\kappa A^3}{8} - \dfrac{\varepsilon_H^2 \omega_d^2 \rho l}{2\psi_d} B\cos(\varphi_A - \varphi_B) \\[4mm] \dot{\varphi}_A = \dfrac{\omega_0^2 - \omega^2}{2\omega} + \dfrac{\varepsilon_H^2 \omega_d^2 \rho l}{2\psi_d}\dfrac{B}{A}\sin(\varphi_A - \varphi_B) \end{cases}$$

(3.15)

Similar treatment for the second line of Eq. (3.12) yields:

$$\begin{cases} \dot{B} = \dfrac{\zeta_H}{2l} B^2 g_H\left(\dfrac{\bar{u}}{B}\right) + \dfrac{\psi_d}{2\rho l}\cos(\varphi_A - \varphi_B) \\[4mm] \dot{\varphi}_B = \dfrac{\omega_d^2 - \omega^2}{2\omega} + \dfrac{\psi_d}{2\rho l}\dfrac{A}{B}\sin(\varphi_A - \varphi_B), \end{cases}$$

(3.16)

with the following function coming from the averaging of the damping term with absolute value:

$$g_H(x) = \begin{cases} \dfrac{2}{\pi}\left(x\arcsin(x) + (2+x^2)\dfrac{\sqrt{1-x^2}}{3}\right) & \text{for} \quad |x| \leq 1 \\[4mm] x & \text{for} \quad |x| > 1 \end{cases}$$

(3.17)

This function corresponds to the one in the nonlinear damping term model used in [8, 86,208], whose accuracy will be confirmed experimentally in the next section. Defining $\Delta\varphi = \varphi_A - \varphi_B$ yields the following system of three coupled equations for the slowly
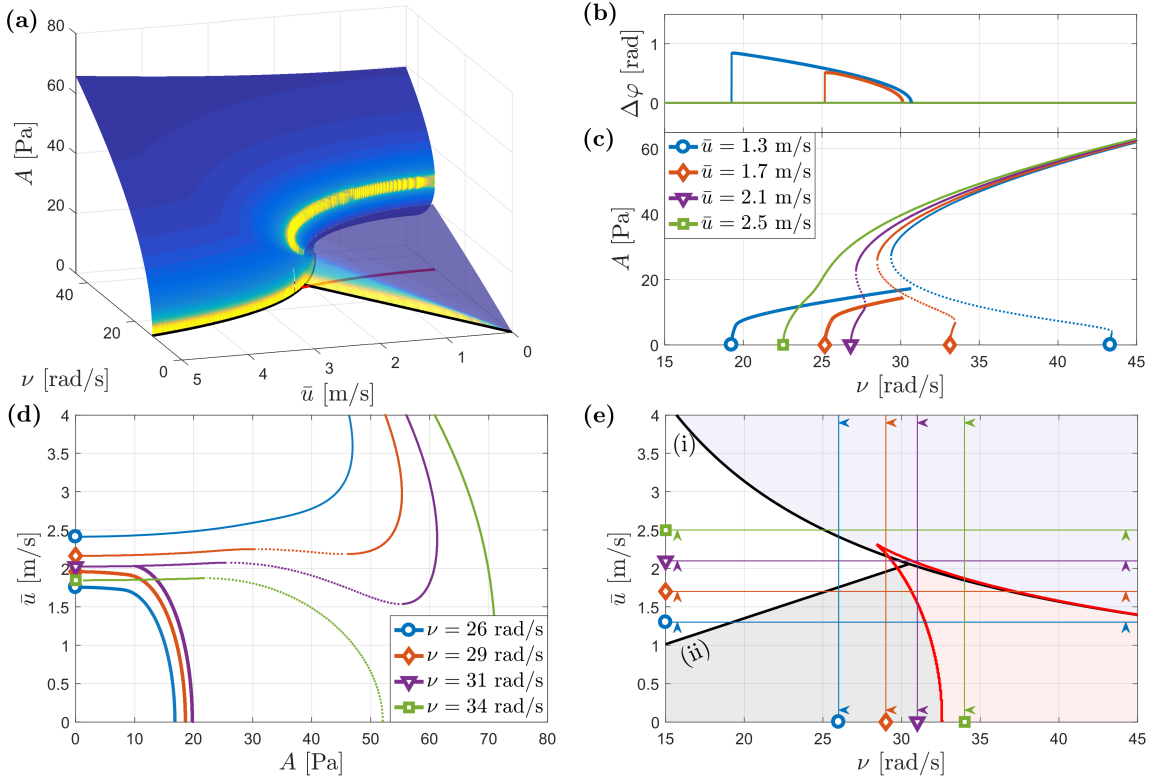
Figure 3.2: **(a)** Chamber limit cycle amplitude A as function of ν and $\bar{u}$ for $\kappa = -0.06$ [s^{-1}.Pa^{-2}] (other parameters are the same as in the experimental setup introduced in the next section) Coloring: gradient of the amplitude A. The transparent surface corresponds to the solutions of Eq. (3.23) (η and u not in phase), while the opaque surface corresponds to the solutions of Eq. (3.20) (η and u in phase) **(b,c)** Corresponding bifurcation diagram as function of ν for different fixed $\bar{u}$ for the amplitude A **(c)** and the phase $\Delta\varphi$ **(b)**. Plain lines correspond to stable fixed points (i.e. limit cycles. thick=out-of-phase, thin=in phase), dotted lines correspond to unstable fixed points. **(d)** Corresponding bifurcation diagram as function of $\bar{u}$ for different fixed ν. **(e)** Stability map as function of ν and $\bar{u}$. Black lines: Hopf bifurcations corresponding to the linear model stability limit. Red lines: fold bifurcations merging in a cusp catastrophe point at ($\nu = 28.4$ rad/s,$\bar{u} = 2.31$ m/s). Grey shaded area: limit-cycles corresponding to out-of-phase solution. Pink shaded area: zone of existence of an unstable fixed point. Purple shaded area: zone where a single stable limit cycle exists. The area not shaded corresponds to the zone where the whole system is stable.

varying amplitudes and the phase between the coupled oscillators:

$$
\begin{cases}
\dot{A} = \nu A + \dfrac{\kappa A^3}{8} - \dfrac{\varepsilon_H^2 \omega_d^2 \rho l}{2\psi_d} B \cos(\Delta\varphi) \\[2em]
\dot{B} = -\dfrac{\zeta_H}{2l} B^2 g_H \left(\dfrac{\bar{u}}{B}\right) + \dfrac{\psi_d}{2\rho l} A \cos(\Delta\varphi) \\[2em]
\Delta\dot{\varphi} = \Delta\omega + \left(\dfrac{\varepsilon_H^2 \omega_d^2 \rho l}{2\psi_d}\dfrac{B}{A} - \dfrac{\psi_d}{2\rho l}\dfrac{A}{B}\right) \sin(\Delta\varphi),
\end{cases}
\tag{3.18}
$$

with $\Delta\omega = \dfrac{\omega_0^2 - \omega_d^2}{2\omega} \simeq \omega_0 - \omega_d$ the detuning constant.

3.2.3 Solutions and interpretation

For the solutions to be partially analytically tractable, one has to assume that the damper is perfectly tuned, i.e. $\Delta\omega = 0$. The first trivial fixed point of the system in Eq. (3.18) is $(0, 0, 0)$. For the non-trivial fixed points, there are two types of solutions. Either **(i)** pressure and velocity are in phase, i.e. $\Delta\varphi = 0$. Then

$$
A = \frac{\zeta_H \rho}{\psi_d} B^2 g_H \left(\frac{\bar{u}}{B}\right)
\tag{3.19}
$$

Substituting this into the second line of Eq. (3.18) gives:

$$
B^5 g_H^3 \left(\frac{\bar{u}}{B}\right) + \frac{8\nu\psi_d^2}{\kappa\zeta_H^2\rho^2} B g_H \left(\frac{\bar{u}}{B}\right) - \frac{4\varepsilon_H^2 l\psi_d^2\omega_0^2}{\kappa\zeta_H^3\rho^2} = 0
\tag{3.20}
$$

Depending on the values of the parameters κ, ν and $\bar{u}$, this equation yields between 0 and 3 solutions. The other type of solution can be found if **(ii)** pressure and velocity are not in phase, i.e. $\Delta\varphi \neq 0$:

$$
\frac{\varepsilon_H^2 \omega_d^2 \rho l}{2\psi_d}\frac{B}{A} - \frac{\psi_d}{2\rho l}\frac{A}{B} = 0
$$

$$
\Rightarrow A = \frac{\omega_d \rho l \sqrt{\varepsilon_H^2}}{\psi_d} B
\tag{3.21}
$$

Substituting this into the first line of Eq. (3.18) gives:

$$
\cos(\Delta\varphi) = \frac{\kappa}{4}\omega_d\rho^2 l^2 \sqrt{\varepsilon_H^2} B^2 + \frac{2\nu}{\omega_d\sqrt{\varepsilon_H^2}}
\tag{3.22}
$$

Substituting the previous results into the second line of Eq. (3.18) gives:

$$
-\frac{\zeta_H}{2l} B g_H \left(\frac{\bar{u}}{B}\right) + \frac{\kappa}{8}\frac{\omega_d^2\rho^2 l^2 \varepsilon_H^2}{\psi_d^2} B^2 + \nu = 0
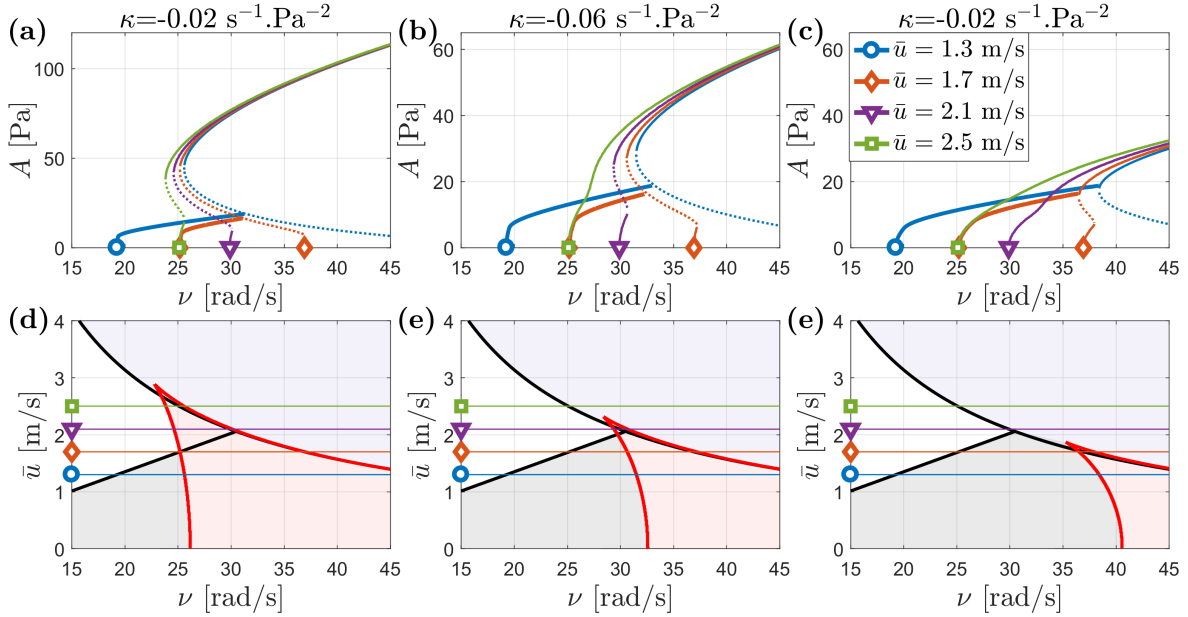\tag{3.23}
$$

Figure 3.3: Influence of the value of κ on the bifurcation diagram ((**a**), (**c**) and (**e**)) and position of the bifurcation lines on the $(\nu - u)$ map ((**b**), (**d**) and (**f**)).

Depending on the values of the parameters κ, ν and $\bar{u}$, this equation yields either 0 or 1 solution. Equations (3.20) and (3.23) are numerically solved for velocity amplitude B and the results used with the other equations to obtain A and $\Delta\varphi$. Since only the acoustic pressure will be measured in the experimental case, the limit cycles are described in terms of averaged amplitude A only. The solutions correspond to stable or unstable fixed points of the system. The stability of the fixed points has been determined by looking at the signs of the eigenvalues of the Jacobian of Eq. (3.18) at the values of the fixed points. In Figure 3.2(**c**) and (**d**), the stable fixed points (i.e. limit cycles) are represented by plain lines, and the unstable fixed points by dotted lines. The fixed points corresponding to solutions of Eq.(3.23) (out-of-phase) are always stable and are represented by thicker plain lines.

Figure 3.2 presents the analytical results for pressure amplitude A for one fixed $\kappa = -0.06$ [s^{-1}.Pa^{-2}]. First, a 3D view of the chamber-damper system limit cycle amplitude A as function of ν and $\bar{u}$ is shown in Figure 3.2 (**a**). The transparent surface corresponds to the solutions of Eq. (3.23) (η and u not in phase), while the opaque surface corresponds to the solutions of Eq. (3.20) (η and u in phase). Taking a closer look at the bifurcations in 2D (Figure 3.2 (**e**)), the two Hopf bifurcations (black lines, defined as transition from stable system to a limit cycle) correspond to the stability limits predicted by the linear model: indeed if one starts from Eq. (3.2), considers the system excited by non-coherent noise, and uses a linear impedance model for the damper, then the RHS corresponds to a linear transfer function. Applying the Routh-Hurwitz criterion to this transfer function gives the linear stability limits corresponding to the Hopf bifurcations in Figure 3.2 (**e**)

(see chapter 2). The result of the use of a nonlinear damping model is the appearance of the two fold bifurcations curves (in red), which are defined as loci where two fixed points collide and disappear. For the present case, they are equivalent to the limit of existence of an unstable fixed point. The point where those two fold bifurcation curves meet is called a cusp catastrophe point, occuring at ($\nu = 28.4$ rad/s,$\bar{u} = 2.31$ m/s). The non-shaded area then corresponds to the stable zone. The grey-shaded area corresponds to a single out-of-phase limit-cycle. The pink-shaded area is the zone of existence of an unstable fixed point, and the purple-shaded area is where a single stable in-phase limit cycle exists.

Some cuts of the bifurcation diagram in Figure 3.2 (e) are shown in Figure 3.2 (d) for fixed ν and Figure 3.2 (b) and (c) for A and $\Delta\varphi$ for fixed $\bar{u}$ respectively. Taking a closer look at Figure 3.2 (c) since those are the results which will be compared to simulations and experiments: one can see that there is an "ideal" purge flow velocity $\bar{u} \simeq 2.1$ m/s for which the onset of instability occurs at the highest initial growth rate ν possible (here about 30 rad/s). For fixed velocity $\bar{u} < 2.1$ m/s, and an increasing ν, a first limit cycle develops when crossing the Hopf bifurcation line (ii) for which η and u are not in phase, with the phase difference decreasing progressively as one increases ν (see Figure 3.2 (b)), until it reaches the fold bifurcation, at which the system "jumps" to a higher limit cycle for which η and u are in phase. From the shape of the bifurcation plots in Figure 3.2 (c), one might also expect some hysteresis to happen when the growth rate ν is ramped up and down. The influence of the value of κ on the bifurcation diagram can be seen in Figure 3.3. For the remainder of this chapter, the initial value of $\kappa = -0.06$ [s^{-1}.Pa^{-2}] will be used.
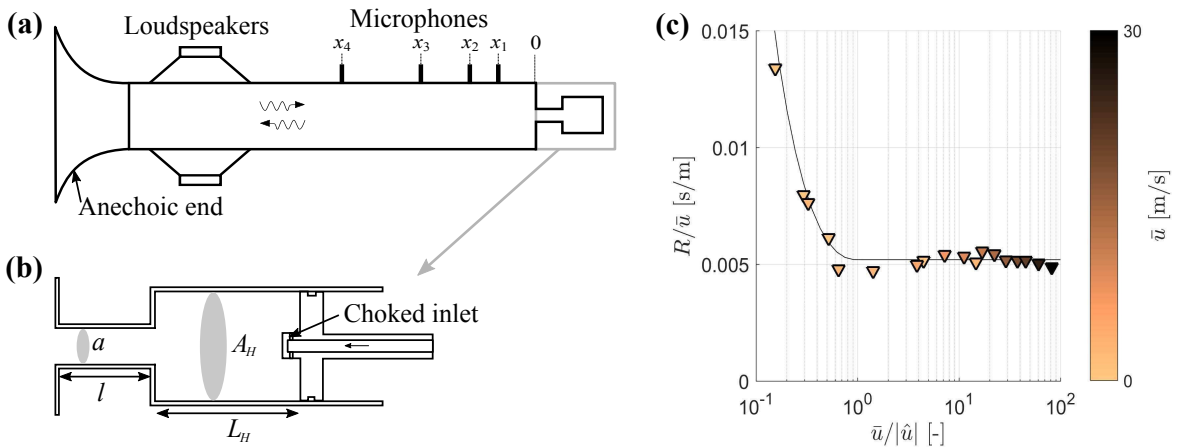

Figure 3.4: (a) Sketch of the impedance tube used for the damper nonlinear model validation (b) cut of the Helmholtz damper (c) Comparison between the resistive term obtained from a fit on the experimental reflection coefficient (triangles) and the resistive term obtained from the nonlinear model R_{NL} (black line).

3.3 Experiments

3.3.1 Validation of the damper nonlinear model

First the validity of the nonlinear damper model using the function g in Eq. (3.17) has to be confirmed. In order to achieve this, the acoustic reflection coefficient $\mathcal{R}$ of our Helmholtz resonator was measured for different mean purge flow velocities and different excitation amplitudes using the Multi-Microphone-Method [79]. A sketch of the impedance tube can be seen in Figure 3.4(a). Two Beyma 12SW1300Nd Loud-speakers and four G.R.A.S. 46BD 1/4" CCP microphones were used. The impedance tube cross-section is 62x62mm. The damper is also sketched in Figure 3.4(b), and its dimensions are as follows: the neck has a diameter of 16.4mm and a length of 45mm. The appropriate end correction is determined using the Helmholtz solver AVSP for the corresponding geometry, which gives $l_{\mathrm{cor}} = 15.6$mm. The back-cavity of the Helmholtz damper is 64mm long (this length is adjustable to be able to tune the damper) and 50mm of diameter. Eight small choked holes feed the damper with purge flow. The experimental reflection coefficient is used to compute the acoustic impedance of the damper using

$$Z_d = \frac{\rho c + \mathcal{R}}{\rho c - \mathcal{R}} \tag{3.24}$$

This experimental impedance is fitted to a simple model by adjusting the specific resistance term R (non-frequency dependent):

$$Z_d = \rho c \left(\frac{l}{c} \cdot \frac{s^2 + \omega_d^2}{s} + R \right), \tag{3.25}$$

Finally this experimentally fitted resistance R is compared to the resistive term from the nonlinear model: indeed, starting from Eq. (3.11), performing a Fourier series expansion of the nonlinear term while neglecting higher frequency terms, uses $\psi_d \dot{\eta} = \dot{p}$, and switching back to frequency domain yields the same expression as Eq. (3.25) replacing R by R_{NL} defined as follows:

$$R_{\mathrm{NL}} = \frac{\zeta_H \hat{u}}{c} g_H \left(\frac{\bar{u}}{\hat{u}} \right), \tag{3.26}$$

with $\hat{u}$ the acoustic velocity and g_H the function from Eq. (3.17). This model with non-frequency dependent nonlinear resistive term has already been used in [8, 86, 208]. The value of the pressure loss coefficient ζ_H has to be fitted so that R_{NL} best matches the resistive term computed for each single measure. The comparison is done in Figure 3.4(c) for $\zeta_H = 1.78$ which gives very good agreement, whether on the linear part (straight line) or on the nonlinear part.

3.3.2 Chamber-damper coupled system measurements

To show the relevance of the analytical model from the first section, a coupled chamber-damper experiment has been designed. The experimental setup consists of a main
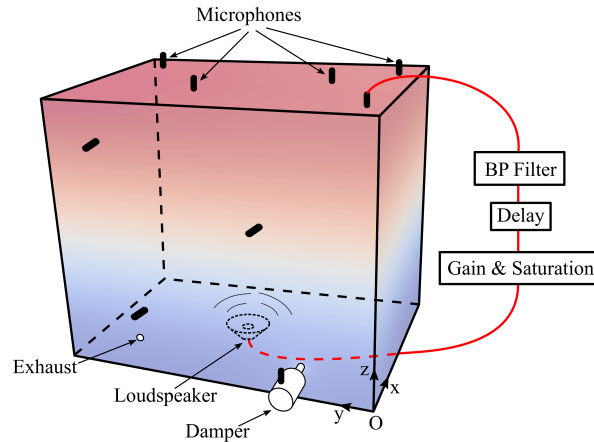
Figure 3.5: Sketch of the measurement setup

Element	x	y	z
Feedback Microphone	70	80	590
Feedback Loudspeaker	245	345	50
Damper	0	165	45
Exhaust	0	325	45

Table 3.1: Coordinates of the different elements in mm in the chamber coordinate system

chamber, which is a 500mm x 700mm x 600mm parallelepipoid metal box, with ridges on the side panels and tensioned metal rods between both main panels to guarantee rigidity. This is essential to ensure that the measured oscillations are indeed acoustic oscillations and that no mechanical resonance interferes. A Pioneer TS-1001I loudspeaker, mounted inside the chamber, is part of the feedback loop that creates the instability. The hole through which the cable enters the chamber also serves as an exhaust for the damper purge flow. A set of eight G.R.A.S. 46BD 1/4" CCP microphones are distributed at different locations on the chamber boundaries for measuring pressure. One suitably located microphone is chosen as the feedback microphone: its signal is filtered, delayed, saturated and amplified by a LabVIEW program loaded onto the National Instruments cRIO-9066 board before being sent back to the loudspeaker. The feedback loop which mimics the constructive interaction between flame heat release and acoustic pressure occurring in real combustion systems is thus completed.

The filter is necessary to ensure that only the first transversal eigenmode (mode of interest) is excited. This mode has a frequency of about 288 Hz and a natural damping $\alpha = 4.8$ rad/s. The additional acoustic losses induced by the exhaust hole when flow is passing through gives an increase of 0.4rad/s to this damping, which is negligible compared to the growth rates ν at which the onset of instability occurs. One can then see in Figure 3.5 that both the loudspeaker and the feedback microphone are

located at pressure anti-nodes. The exact location of the different elements in the chamber coordinate system is shown in Table 3.1. The delay $\tau = 2.1$ms, giving the most unstable state (i.e. maximizing β) was chosen and kept fixed for the whole set of experiments. The saturation takes the form of the nonlinear term of the first coupled equation, similar to what was used in [133]:

$$S(U_f) = c_1 U_f + c_2 U_f^3, \qquad (3.27)$$

with U_f the incoming voltage from the feedback microphone. One can thus play on the saturation coefficient and the growth rate separately, knowing that $\nu_{\text{eff}} \propto c_1$ and $\kappa_{\text{eff}} \propto c_2$. On one of the chamber main panels, the previously tested Helmholtz damper can be mounted and fed with a purge flow. The damper is tuned by setting the feedback loop so that an instability is established inside the box and adjusting the length of the damper so that the amplitude of the instability is minimal (determination by ear). From the location of the damper with respect to the mode $\psi_d \simeq 0.95$ is an adequate estimation. An additional microphone records the pressure inside the damper volume, which is in quadrature with the velocity u inside the damper neck.

Two types of measurements were performed and are shown in Figure 3.6. To determine the law between c_1 and ν, growth rate measurements were performed where one lets the instability grow and then fits the linear growth of the logarithm of the envelope and average over ten instances to obtain the growth rate (Figure 3.6 **(a)**). Once the growth rate is known, one can get the actual saturation coefficient κ from any limit cycle amplitude without damper using: $A = \sqrt{-8\nu/\kappa}$. The second type of measurement performed is the actual ramping of the growth rate, which was achieved by simply ramping c_1 automatically within the LabVIEW program. The experimental ramp speed was about 20s for 1 rad/s increase/decrease. An example of the results of such a measurement is shown Figures 3.6 **(b)** and **(c)** for $\bar{u} = 1.3$ m/s: one can see that the pressure inside the chamber grows to a limit cycle past a certain growth rate ν, and then jumps to a higher limit cycle. The phase between chamber pressure and damper neck velocity (obtained by substracting $\pi/2$ to the phase between chamber pressure and damper volume pressure) also follows the trend shown in Figure 3.2 **(b)**: it is not defined when there is no limit cycle, then starts from a non-zero value and decays to zero as the growth rate is increased.
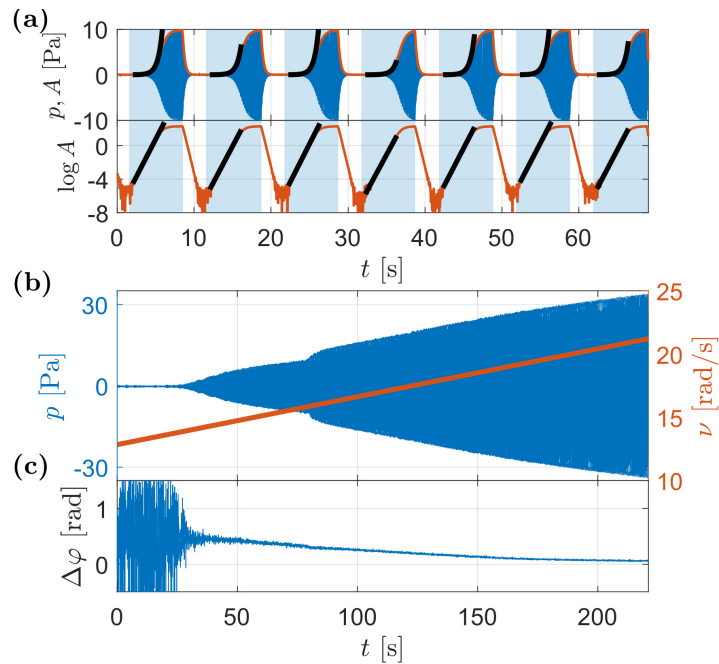
Figure 3.6: Measurement techniques: growth rate measurements **(a)** and growth rate ramping with effect on the pressure inside the chamber **(b)** and on the phase between the chamber pressure and the damper neck velocity (which corresponds to $\pi/2$ substracted to the phase between chamber pressure and damper volume pressure)

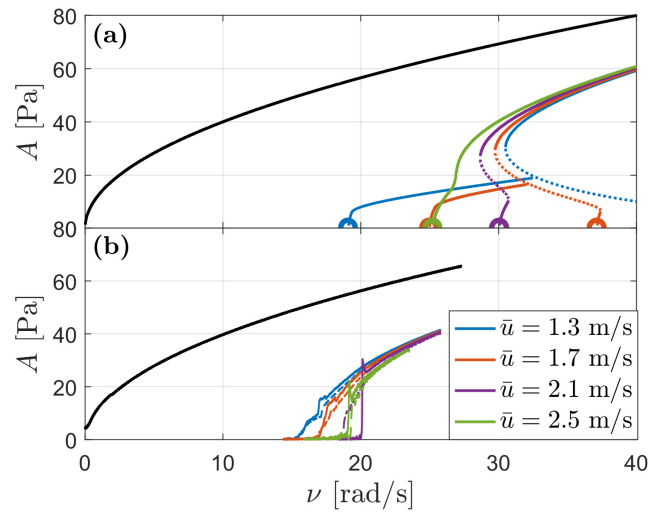Figure 3.7: Comparison between analytical results **(a)** and experiments (envelope of the pressure measured during ramping of ν, plain=ramping up, dashed=ramping down) **(b)**. Black lines= chamber without damper. Besides the mismatch for the onset growth rate, one can see that the tendency is well reproduced, and all curves seem to collapse for higher growth rate even though their order is reversed.
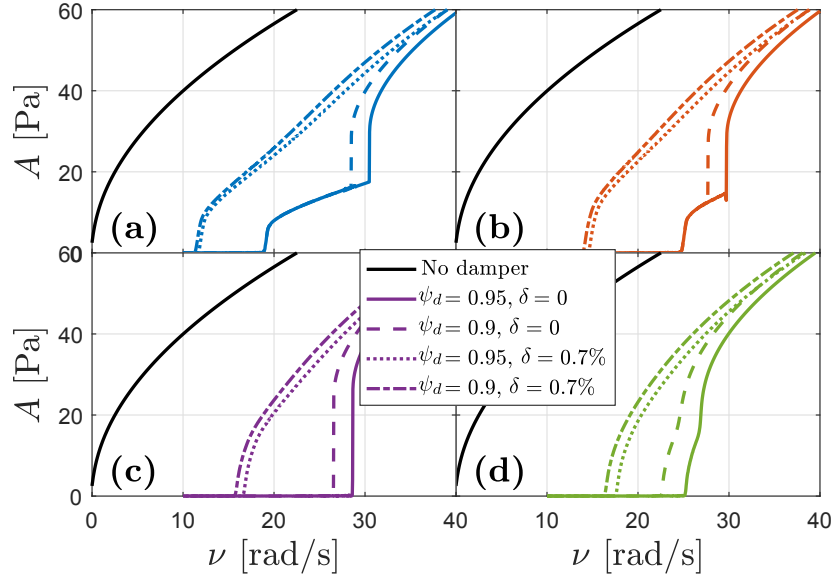
3.4 Results

Figure 3.8: Comparison between numerical results from slowly ramping down the growth rate, highlighting the influence of detuning $\delta = \Delta\omega/\omega_0$ and of damper position with regard to mode shape ψ_d **(a)** $\bar{u} = 1.3$ m/s **(b)** $\bar{u} = 1.7$ m/s **(c)** $\bar{u} = 2.1$ m/s **(d)** $\bar{u} = 2.5$ m/s

We now concentrate on the effect of the damper on the chamber pressure amplitude A only. Figure 3.7 compares the results of the analytical model (top) with the experiments (bottom) for different purge flow velocities $\bar{u}$. The results of the chamber without damper (black curves) are very well reproduced. For the results with damper, the behavior of the limit cycles is also well reproduced although there is a 30% error on the predicted onset of instability between model and experiments. Our hypothesis is that this is due to a small detuning of the damper: indeed, modifying the damper back chamber length L by 1mm leads to a detuning $\delta = \Delta\omega/\omega_0 > 0.7\%$.

Figure 3.8 shows how such a small detuning can strongly influence the onset point of the instability. Another source of uncertainty is the maximum mode amplitude at damper location ψ_d. Since the chamber acoustic shape is altered by the presence of the loudspeaker, the exhaust hole and the damper itself it can well be that the mode shape is different from the theoretical one and that ψ_d has been overestimated. Despite this fact, in Figure 3.7, the onset of instability follows the trend of the model for increasing velocity: at first, the higher the purge flow, the later the instability is triggered, until one reaches an "ideal" velocity, after which the onset of instability occurs at lower initial growth rates again. The collapsing of all curves for high growth rates is also well reproduced even though their order is reversed.
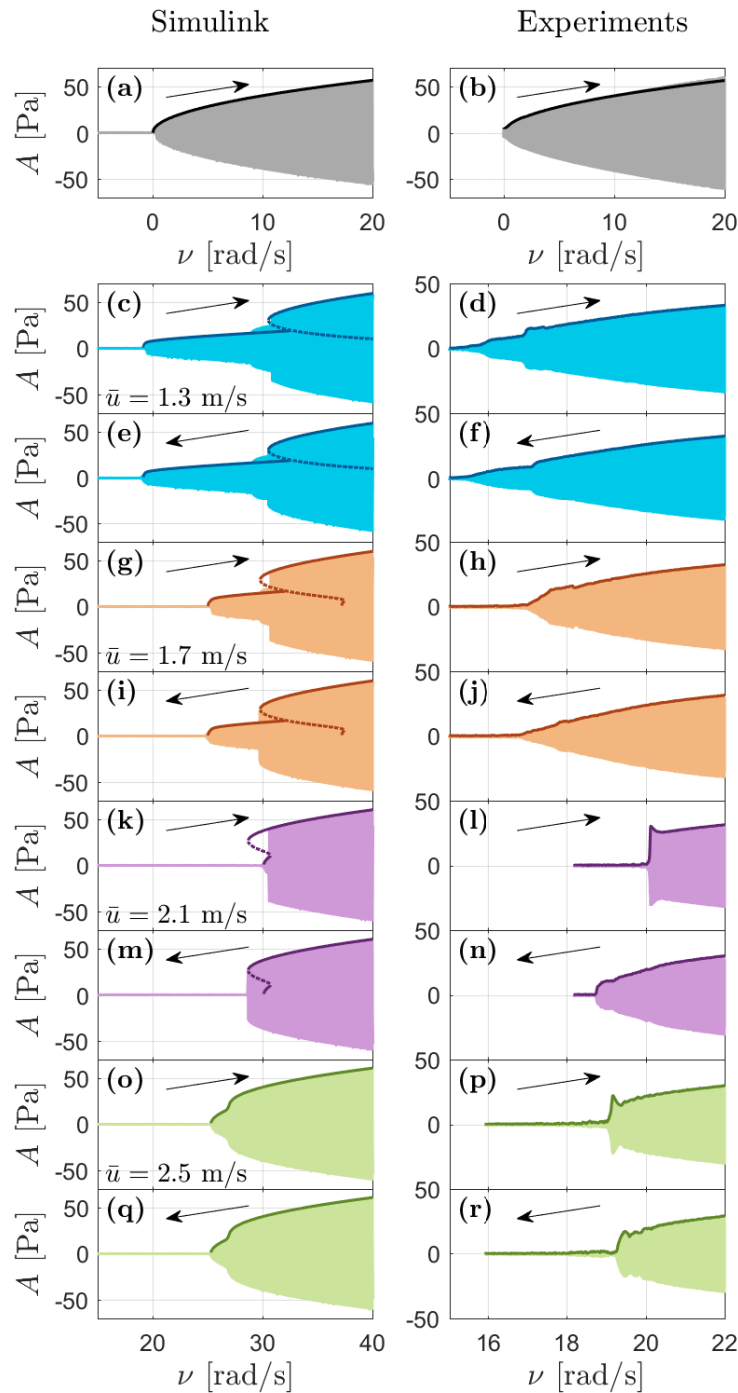
Figure 3.9: Comparison between Simulink simulations and analytical model (left column) and experiments (right column). On the left, the results of the analytical model are superimposed on the Simulink simulations, which highlights the perfect match between both. **(a)** and **(b)** represent the chamber without damper. Despite a different onset of instability, nonlinear features are well reproduced experimentally, for example the "jump" in **(d)** and **(f)**, and the hysteresis in **(l)** and **(n)**.

In addition to the analytical work and to the experiments, Simulink simulations of the system in Eq. (3.12) were performed for different $\bar{u}$ ramping ν up and down at a rate of about 100s for 1 rad/s increase/decrease. In order to have a better look at the limit cycle behavior close to the onset of instability, one has to zoom on this part of the curve for both Simulink/analytical model and experiments. Those results for ramping up and down and for different velocities are shown in Figure 3.9. The agreement between theoretical results and simulations (on the left) is very good. One is able to reproduce the "jump" between limit cycles (**(c)**, **(e)**, **(g)** and **(i)**), and the inferred hysteresis as well (**(k)** and **(m)**). And most importantly, the general behaviour of the experimental limit cycles (on the right) confirms the validity of our model since both the "jump" from different limit cycles (**(d)** and **(f)**), and the hysteresis (**(l)** and **(n)**) are reproduced.

3.5   Conclusion

An analytical model for the chamber-damper coupled system was derived, using a linearly unstable oscillator with cubic saturation for the chamber and a nonlinear damping for the damper. Amplitude equations were derived and the theoretical limit cycles of the coupled system computed in the case where the damper is perfectly tuned. Time-domain simulations of the analytical system of ODEs were performed which are in excellent agreement with the theoretical predictions of the limit cycle amplitude. Experiments were then performed by ramping the growth rate inside a papallelepipedic chamber with a damper, in which the thermoacoustic instability is mimicked by an electro-acoustic feedback loop. Although the onset of instability occured about 30% earlier than expected (most probably due to slight detuning of the damper), some of the nonlinear features of the model were experimentally reproduced, thus underlining the importance of using a nonlinear model for the damper. This is essential if one wants to be able to predict potential dangerous behavior close to the onset of instability when mapping a new engine for example, such as hysteresis and sudden "jumps" from one limit cycle to another.

Chapter 4

Whistling of deep cavities subject to turbulent grazing flow: intermittently unstable aeroacoustic feedback

In this chapter, the focus is on aeroacoustic instabilities, namely where the acoustic cavity modelled as a damped harmonic oscillator does not act as an additional stabilizing device, but rather enables the instability to take place when coupled to an unsteady shear layer. To that end, the classic problem of the aeroacoustic instability occurring in deep cavities subject to a low-Mach grazing flow is revisited experimentally and theoretically. The deep cavity can be modelled in a similar manner to the Quarter-Wave damper modelling done in Chapter 2. The aeroacoustic instability is caused by the constructive feedback between the acoustic modes of the cavity and the turbulent shear layer that forms at its opening. Systematic experiments are performed in order to construct a new theoretical model, which describes the aeroacoustic system as two linearly stable oscillators, with linear reactive coupling, nonlinear damping and nonlinear resistive coupling. This model constitutes the basis for a linear stability analysis, and for the prediction of limit cycle amplitudes by using a describing function approach and by searching the fixed points of amplitudes equations. Moreover, it is shown that only supercritical Hopf bifurcations are found in this aeroacoustic system, and that in contrast with many flow-induced-vibration problems, frequency lock-in does not occur. In the last part of the chapter, the intermittency observed in the vicinity of the supercritical Hopf bifurcations is successfully modelled by adding a coloured multiplicative noise to the grazing flow velocity in order to account for the effect of turbulence. The necessary conditions

favouring intermittently stable or intermittently unstable intervals in such systems are identified using stochastic differential equations governing the aeroacoustic oscillations and Fokker-Planck equations ruling the probability density function of the acoustic envelope. This work is relevant for many musical and industrial configurations exhibiting this type of aeroacoustic instabilities.

This chapter is pased on the research article *"Whistling of a deep cavity subject to turbulent grazing flow: intermittently unstable aeroacoustic feedback"* by Claire Bourquard, Abel Faure-Beaulieu and Nicolas Noiray submitted to the Journal of Fluid Mechanics in April 2020.

4.1 Introduction

The sound of flutes is produced through aeroacoustic instabilities that result from the constructive feedback between the acoustic modes of the instruments and the dynamics of a shear layer [54]. These instabilities also cause numerous issues in industry because they can induce significant noise pollution and unwanted vibrations leading to fatigue failures [207]. They have been investigated over several decades and they fall into the category of "fluid-resonant" cavity flows in the classification established by Rockwell & Naudascher [150]. This type of instability can be further divided into two groups: the self-sustained flow oscillations in shallow cavities [154], and the ones of deep cavities [183].

In the former group, the unsteady cavity flows are governed by the mechanism described by Rossiter [152] and they are particularly relevant for aeronautic applications at high subsonic and low supersonic grazing flows. Canonical configurations have been investigated numerically with dynamic systems and control theory [76], and with computational aeroacoustics (CAA) methods, which are based on Direct Numerical Simulations (DNS) and Large Eddy Simulations (LES) of the compressible Navier-Stokes equations [63, 153, 196] or on the linearization of these equations around a given base flow [178, 192].

In the latter group, to which belongs the aeroacoustic instability investigated in this work, the self-sustained flow oscillations involve the longitudinal acoustic eigenmodes of the deep cavity. These instabilities are usually relevant for low-Mach grazing flows and their modelling has been the topic of intense research over several decades. Most of the investigations considered the canonical problem of a single deep cavity, while some works deal with multiple deep cavities [40, 184] and liners made of deep cavities equipped with perforated plates [39]. There are also several studies dealing with various passive control methods to prevent whistling of a deep cavity, such as flow obstacles inside the cavity [113], internal cavity liner [72] or changes of the curvature of the cavity opening corners [188].

Many of the studies focusing on single deep cavities, including the present investigation, follow the work of Elder [50], who proposed a feedback loop analysis with the cavity opening and its aerodynamic forcing as a *forward* transfer function and the acoustic resonance of the deep cavity as a *backward* transfer function. For example, Mast & Pierce [112] and Kook & Mongeau [93], who used a frequency-domain describing function analysis to predict the occurrence and the amplitude of deep cavity whistling.

A key element of this type of analysis is the forward transfer function, which is governed by the unsteady vorticity-velocity cross product as pointed out by Howe [73] and Nelson *et al.* [126] about 40 years ago. The analytical models of this transfer function can be grouped into two categories: the ones based on the work of Howe [74], which considers the shear layer as a thin vortex sheet and the ones that are based on discrete vortices that are periodically shed from the upstream corner of the cavity [126]. One can for instance refer to the papers of Bruggeman *et al.* [24] or Dequand *et al.* [42] in which the latter formulation is adopted. Dequand *et al.* [42] also compared against simulations of the compressible Euler equations and results from the vortex blob method of of Peters & Hoeijemakers [140]. More recently, Ma *et al.* [109] used particle image velocimetry to show that shear layers do not appear as either a flapping vortex sheet or discrete vortices, but rather as a combination of these two ideals, which depends on the grazing flow velocity and on the self-sustained oscillation amplitude. While several studies concentrate on frequency-domain oriented analysis, there are also some investigations focusing on time-domain simulations and transients, which is particularly relevant for music instruments [182, 187]. Semi-empirical models of the forward transfer function can also be directly derived from measurements of the impedance of the cavity opening and its shear layer [64, 83]. Finally, it is important to mention that one can use various computational methods to identify the aeroacoustic response of the cavity opening. A first example is the paper of Martínez-Lera *et al.* [111], in which the forward transfer function is obtained from incompressible flow simulations, vortex sound theory and system identification techniques. In fact, for sufficiently low frequencies, the cavity opening is acoustically compact and the unsteady flow can be locally considered and simulated as incompressible. Another example is the work of Gikadi *et al.* [62], where the compressible Navier-Stokes equations are linearized around a mean grazing flow obtained from LES and where the forward transfer function and transfer matrices are successfully compared with the experiments from Karlsson & Åbom [83]. One can also refer to the paper of Boujo *et al.* [20], who considered the incompressible Navier-Stokes equations linearized around mean flows of the acoustically forced cavity opening. The latter mean flows were obtained from LES for a range of acoustic forcing amplitudes, in order to demonstrate that the forward transfer functions can be extracted with this method in the linear regime, but also in the saturated non-linear regime.

In the present work the forward and backward transfer functions are measured for ranges of grazing flow velocities, cavity depths and acoustic amplitudes, and used for deriving a new low-order model of the aeroacoustic system in the form of two coupled oscillators. This formulation allows us to revisit this classic problem and to provide novel insights

about the underlying deterministic and stochastic dynamics. This nonlinear model is used for frequency-domain describing function analysis as well as for performing time-domain simulations and for deriving amplitude and phase equations. We also add stochastic forcing terms to this low-order predictive model to represent the effect of turbulence on the aeroacoustic instability. In fact the unsteady component of the flow in deep cavities subject to turbulent grazing flows can be decomposed as turbulent fluctuations and coherent fluctuations. The recent experimental works of Ishikawa *et al.* [78] and of Boujo *et al.* [21] show the coexistence of these two types of fluctuations in the case of a whistle and of a bottle.

We will also focus on the fact that our aeroacoustic oscillations are intermittent for some combinations of turbulent grazing flow velocity and cavity depth. Intermittency in dynamical systems has received considerable attention. In the case of thermoacoustic instabilities, one can for instance refer to the early work of Clavin *et al.* [29] or to the more recent studies from Nair *et al.* [124] or from Bonciolini *et al.* [14]. Many of the investigations dealing with intermittency of thermoacoustic systems concentrate on noise-driven subcritical Hopf bifurcations. We will show in the present chapter that thermoacoustic and aeroacoustic configurations exhibiting supercritical Hopf bifurcations can also exhibit intermittency, with similar acoustic pressure statistics that correspond to sporadic bursts of high amplitude oscillations, but with very different dynamical signature. Indeed, we will show that the present aeroacoustic system can be intermittently unstable, as the systems investigated by Mohamad & Sapsis [118], and we will identify the necessary conditions for observing this intermittency.

The experimental setup and the aeroacoustic instability are introduced in section 4.2. The specific acoustic admittance of the deep cavity and the specific acoustic impedance of its opening with and without grazing flow are presented in section 4.3, together with the linear model of coupled oscillators and the analysis of its eigenvalues. In section 4.4, the nonlinear problem is treated with a describing function analysis as well as with amplitude equations. Finally, the experimental and theoretical analysis of the intermittency at play in the present aeroacoustic system is investigated in section 4.5.

4.2 Experimental setup and aeroacoustic instability

The system considered in the present work consists of a two meters long wind channel with a square cross-section of side $H = 62$ mm, which is supplied by a blower and is operated at atmospheric pressure. The temperature in the channel is maintained constant at 23°C with a heat exchanger located immediately downstream of the blower, which corresponds to a speed of sound in the channel c of 345 m/s. The bulk flow velocity U in the channel is varied between 35 and 75 m/s, respectively corresponding to Reynolds numbers $Re = UH/\nu = 145\,000$ and $310\,000$, where $\nu = 1.5 \times 10^{-5}$ m^2/s is the kinematic viscosity of the air. The bulk velocity is deduced from the mass flow and the temperature in the channel, which are respectively measured with a Bronkhorst
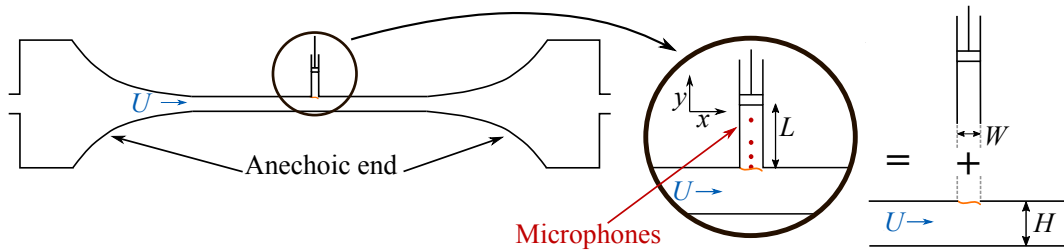
Figure 4.1: Sketch of the experimental setup used to investigate the side-branch cavity whistling. The system is broken down into two subsystems: the deep cavity and the interface between the cavity and the channel along which the shear layer develops.

IN-FLOW F-106CI and a thermocouple. A side-branch cavity is located in the middle of the channel as shown in Figure 4.1. This rectangular cuboid spans across one of the channel sides, exhibits a cross section $W \times H$ with $W = 30$ mm, and its length L can be varied using a tight piston. The edges of the T-junction are sharp. Large plenums ($0.5 \times 0.7 \times 0.7$ m^3) equipped with sound absorbing foam and catenoid horns are mounted at both ends of the channel in order to create anechoic conditions upstream and downstream of the side-branch cavity. The corresponding cut-off frequency is around 300 Hz, and the upstream and downstream reflection coefficients drop below 0.1 beyond that frequency. The coordinate system is defined as follows: the x axis points in the direction of the flow, and the y axis inside the deep cavity, with the origin set in the middle of the junction. A turbulent shear layer develops between the main channel and the side-branch cavity. Depending on the mean flow velocity U and the cavity length L, an aeroacoustic instability can occur due to a constructive feedback between the acoustic modes of the cavity and the aerodynamic modes of the shear layer.

In the present study, the cavity length L is varied between 200 and 270 mm, and the acoustic mode of the cavity which is involved in the aeroacoustic instability is the three-quarter wave eigenmode, with its eigenfrequency being close to $f_a = 3c/4L$. For this range of length, the cavity length to width ratio L/W is about 8 and therefore the configuration falls in the category of *deep cavity* whistling. Four G.R.A.S. 46BD 1/4" CCP microphones are flush-mounted on the internal wall of the cavity, at $y = 0$, 45, 90 and 190 mm. The full set of microphones is used for the measurements of reflection coefficient presented in the next section. The acoustic pressure time traces used to characterise the aeroacoustic instability were recorded with the third microphone, which is located in the vicinity of a pressure antinode of the three-quarter wave mode for the considered range of length L.

The length of the deep cavity is first fixed to $L = 250$mm and the power spectral density S_{pp} of the acoustic pressure p at $y = 90$ mm is measured for a range of mean flow velocity U, between 35 and 75 m/s. This mapping is presented in Figure 4.2(a). One can see in Figure 4.2(b) that for $U = 74$ m/s, the power spectral density of the acoustic pressure exhibits a sharp high amplitude peak at around 980 Hz, which is the
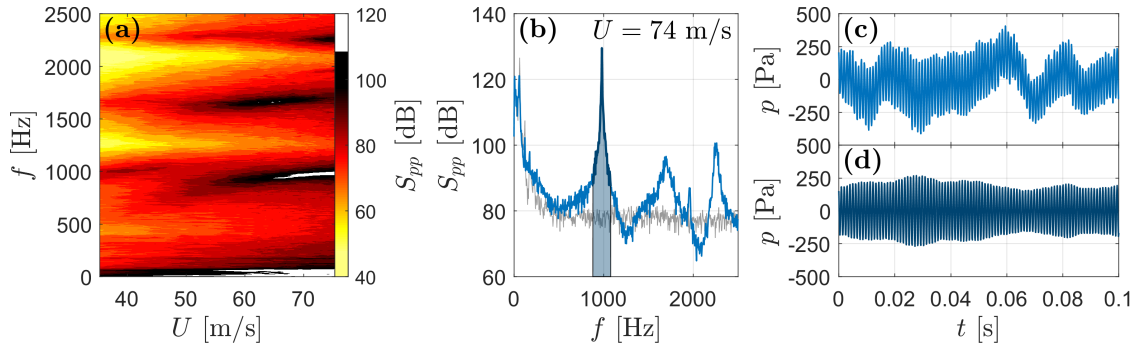
Figure 4.2: **(a)** Mapping of the power spectral density of the acoustic pressure S_{pp} recorded in the cavity at $y = 90$ mm for mean bulk flow velocities in the wind channel ranging from 35 to 75 m/s, and for a fixed cavity length $L = 250$ mm. **(b)** Blue line: S_{pp} in the cavity at $y = 90$ mm for $U = 74$ m/s. Gray line: S_{pp} in the wind channel at $y = -31$ mm for the same velocity, but without cavity, i.e. $L = 0$ (the piston is flush to the wind channel wall). **(c)** Raw acoustic pressure time trace at $y = 90$ mm, for $L = 250$ mm and $U = 74$ m/s. **(d)** Band-pass filtered acoustic pressure (inverse Fourier transform of the shaded area in Figure 4.2**(b)**).

signature of a strong aeroacoustic limit cycle. Its harmonic at 1960 Hz is also visible in the power spectral density. This limit cycle involves the three-quarter wave acoustic eigenmode of the deep cavity, whose natural eigenfrequency can be approximated by $3c/4L = 1035$ Hz when the end correction is not considered, and whose presence is visible at low velocities in Figure 4.2**(a)**.

The raw acoustic pressure time trace for $U = 74$ m/s is shown in Figure 4.2**(c)**. It can be decomposed into two main components: slow fluctuations, which correspond to the high-amplitude low-frequency content of the power spectral density (below 200 Hz), and fast fluctuations originating from the aeroacoustic instability of the deep cavity. The low frequency content originates from the blower and the natural aeroacoustic sources of the air supply line, as indicated in the acoustic power spectral density in the channel and in absence of cavity, which is shown in Figure 4.2**(b)**. In order to isolate the dynamics of the aeroacoustic limit cycle, the acoustic pressure signal is band-pass filtered with a 200 Hz bandwidth centered on the main peak (see shaded region in Figure 4.2**(b)**). In the next figures showing time traces and probability density functions (PDFs) of acoustic pressure from experiments, the signals are filtered in this way. The filtered time trace for $U = 74$ m/s is shown in Figure 4.2**(d)** and it features a slowly varying amplitude modulation that is typical of a self-sustained weakly nonlinear oscillator subject to random forcing.

In order to get insights in the aeroacoustic feedback at play in these self-sustained oscillations, Particle Image Velocimetry (PIV) is used to characterize the dynamics of the shear layer. The use of PIV for characterizing shear layer dynamics of unsteady cavity flows has been reviewed by Morris [121]. It is here combined with acoustic
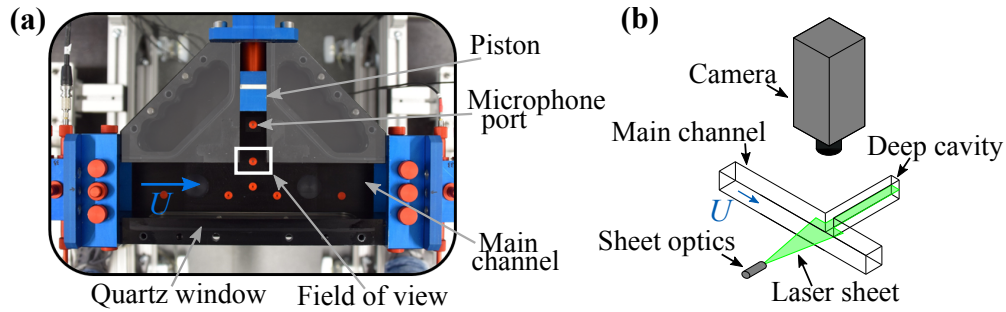
Figure 4.3: **(a)** Picture of the test section placed in the middle of the wind channel. The length L of the side-branch cavity is adjusted with the piston. The PIV field of view, which encompasses the turbulent shear layer, is indicated with the dotted line rectangle. **(b)** Sketch of the experimental setup used for PIV measurements.

records to perform phase-averaging of the velocity field in the shear layer region, which is optically accessible through two quartz windows as shown in Figure 4.3. These PIV measurements are made using a double cavity laser (Photonics DM60Nd:YAG, 532 nm), a laser guiding arm, sheet optics and a HighSpeedStar X camera from Lavision. The camera is equipped with a Nikon 100F/2.8D lens and a 36mm extension ring, and it is placed perpendicularly to the laser sheet formed in the central plane of the channel. The seeding of the flow is achieved with a spray of Di-Ethyl-Hexyl-Sebacat (DEHS) in the inlet plenum. A measurement of 2500 double-frame images at a rate of 5 kHz with time interval of 10 μs between pairs of consecutive laser pulses is performed in combination with the recording of acoustic signal at 50 kHz sampling rate.

The trigger of the camera and the acoustic pressure signal are used to assign to each Mie-scattering image its corresponding phase angle with respect to the self-sustained aeroacoustic oscillations. Instantaneous snapshots of the velocity magnitude $|\boldsymbol{v}|$ are presented in the top row of Figure 4.4 and show the presence of small scale turbulent structure along the shear layer. Phase averaging was performed by considering instantaneous velocity fields falling in the same phase bin in order to remove the *zero mean turbulent component* of the velocity $\check{\boldsymbol{v}}$, and the magnitude of the resulting *phase-averaged component* of the velocity $|\langle\boldsymbol{v}\rangle|$ are shown in the middle row of Figure 4.4.

One can observe that there is no coherent vortex shedding from the upstream corner. In fact, the shear layer exhibits a hardly discernible low-amplitude coherent flapping motion, despite the intense sound level ($\approx$ 130 dB) in the cavity that results from this aeroacoustic limit cycle. These results clearly show that the assumption of a thin vortex sheet [74] is adequate to describe the present aeroacoustic limit cycle. The *mean component* of the velocity field $\bar{\boldsymbol{v}}$, which is obtained by averaging the 2500 instantaneous fields, is then subtracted from the phase-averaged velocity fields $\langle\boldsymbol{v}\rangle$ in order to extract the *zero mean coherent component* of the velocity fluctuations $\tilde{\boldsymbol{v}}$. Note that these
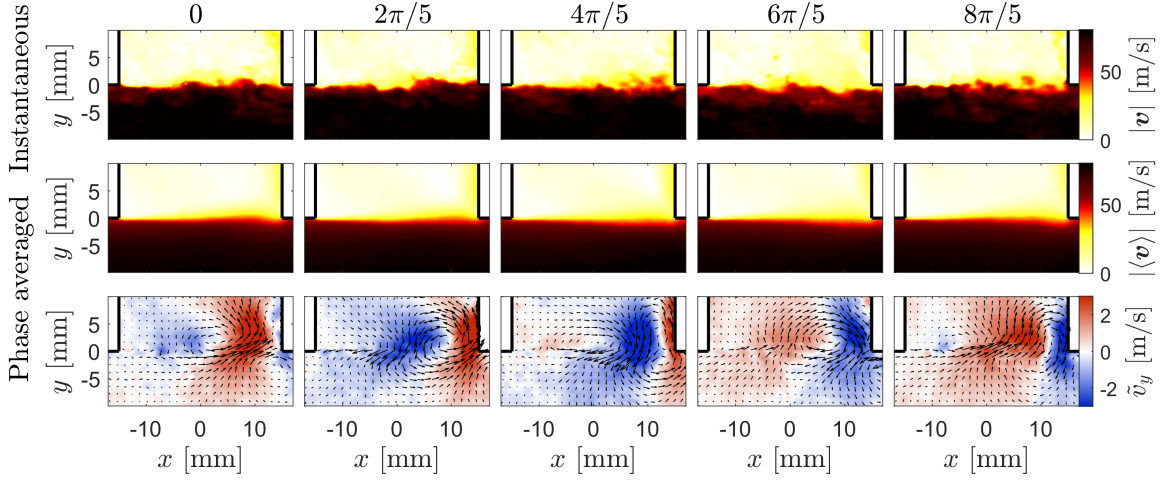
Figure 4.4: Combined PIV and acoustic data processing for characterizing the shear layer dynamics of the aeroacoustic limit cycle occurring when $L = 250$ mm and $U = 74$ m/s. Top row: Instantaneous velocity magnitude $|\boldsymbol{v}|$ at 5 regularly spaced instants of an acoustic period. Middle row: Phase-averaged velocity magnitude $|\langle \boldsymbol{v} \rangle|$. Bottom row: vector field of the zero mean coherent component of the velocity fluctuations $\tilde{\boldsymbol{v}}$ coloured by its vertical amplitude $\tilde{v}_y$. Movies can be seen in the supplementary material.

notations correspond to the following decompositions of the total velocity field: $\boldsymbol{v} = \bar{\boldsymbol{v}} + \tilde{\boldsymbol{v}} + \check{\boldsymbol{v}} = \langle \boldsymbol{v} \rangle + \check{\boldsymbol{v}} = \bar{\boldsymbol{v}} + \boldsymbol{v}'$, where $\boldsymbol{v}'$ are the zero mean fluctuations. The vector field $\tilde{\boldsymbol{v}}$ is presented in the bottom row of Figure 4.4 together with the magnitude of the vertical coherent velocity fluctuations. It shows that the constructive aeroacoustic feedback involves the first longitudinal hydrodynamic mode whose wavelength is close to the cavity width W. The nonlinear response of this aerodynamic eigenmode to transverse acoustic forcing has been investigated numerically by Boujo *et al.* [20] with the same geometry but at a lower bulk flow velocity ($U = 56$ m/s).

4.3 Linear model of coupled oscillators

In this section, a linear model is derived to describe the aeroacoustic instability. As shown in the sketch on the right of Figure 4.1, the aeroacoustic system is broken into two coupled subsystems: the deep cavity and the cavity opening being subject to the turbulent grazing flow. The acoustic velocity $\tilde{\boldsymbol{u}}$ is the irrotational part of the zero-mean coherent component of the velocity, and in the remainder of this chapter, we focus on its vertical component at the opening $\tilde{u}_y$, which we will just denote u. In subsection 4.3.1, measurements of the specific acoustic admittance of the deep cavity $\mathcal{A} = \rho c \hat{u}/\hat{p}$ and of the specific acoustic impedance of the cavity opening $\mathcal{Z} = \hat{p}/\rho c \hat{u}$, are conducted and serve as a basis for the model derivation. In these expressions, ρ denotes the air density and $\hat{\cdot}$ stands as frequency domain formulation for the acoustic velocity $\hat{u}$ and pressure $\hat{p}$ at the cavity opening.
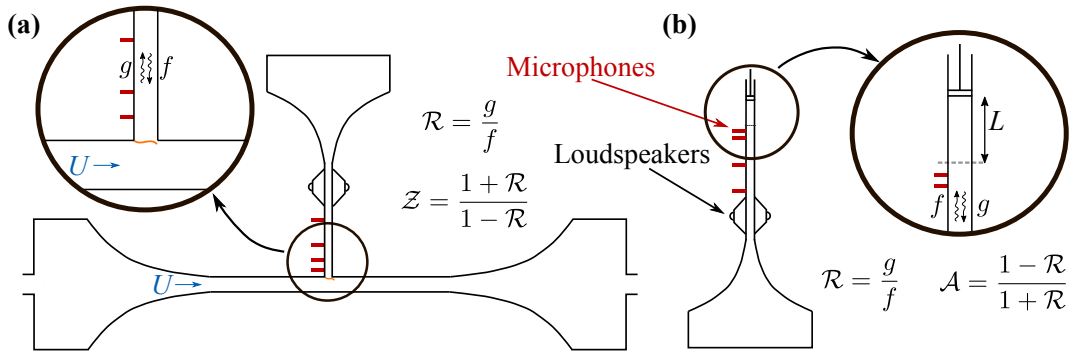
Figure 4.5: **(a)** Experimental setup for measuring the reflection coefficient $\mathcal{R}$, which is the ratio of the forward and backward acoustic Riemann invariants f and g, and the specific impedance $\mathcal{Z}$ of the interface between the cavity and the channel along which the shear layer develops. **(b)** Experimental setup for measuring the specific admittance of the deep cavity $\mathcal{A}$.

4.3.1 Impedance measurements and model derivation

Measurements of $\mathcal{Z}$ and $\mathcal{A}$ are made using the experimental setups respectively shown in Figure 4.5**(a)** and 4.5**(b)**. Acoustic forcing is applied with loudspeakers and the Multi-Microphone Method [159] is used to reconstruct the amplitude and phase of the forward and backward acoustic Riemann invariants f and g, with which the reflection coefficient $\mathcal{R}$ and the specific impedance or admittance at a reference plane are deduced. The specific impedance of the cavity opening $\mathcal{Z}$ and the specific admittance of the deep cavity $\mathcal{A}$, which are measured with this method, are respectively presented in Figure 4.6**(a)** and 4.6**(b)** for several bulk flow velocities U, and in Figure 4.6**(c)** and 4.6**(d)** for several cavity lengths L.

The white circles correspond to the specific impedance $\mathcal{Z}$ without flow. In that case, the specific resistance $\Re(\mathcal{Z})$ is rather constant and it is equal to about 0.25 for the considered frequency range. This can be explained by considering the analogy between the travelling acoustic waves f and g in the side-branch cavity (see Figure 4.5**(a)**) and the ones travelling toward and from an idealized compact area expansion in a duct. In the latter configuration, the amplitude reflection and transmission coefficients are respectively given by $\mathcal{R} = (\varepsilon-1)/(\varepsilon+1)$ and $\mathcal{T} = 2\varepsilon/(\varepsilon+1)$, and the specific impedance is $\mathcal{Z} = \varepsilon$, where ε is the area ratio at the sudden area expansion.

In the present configuration, one can approximate the effective area expansion as the ratio between the cavity cross section WH and twice the wind channel cross section $2H^2$, because acoustic energy originating from the cavity is transmitted in both the upstream and downstream direction of the channel. It leads to $\varepsilon \approx W/2H = 0.24$, which is very close to the measured specific acoustic resistance. In contrast with the above-mentioned model for a compact area expansion, the measured specific reactance is not zero. This is due to the fact that an end-correction due to inertial effects is not
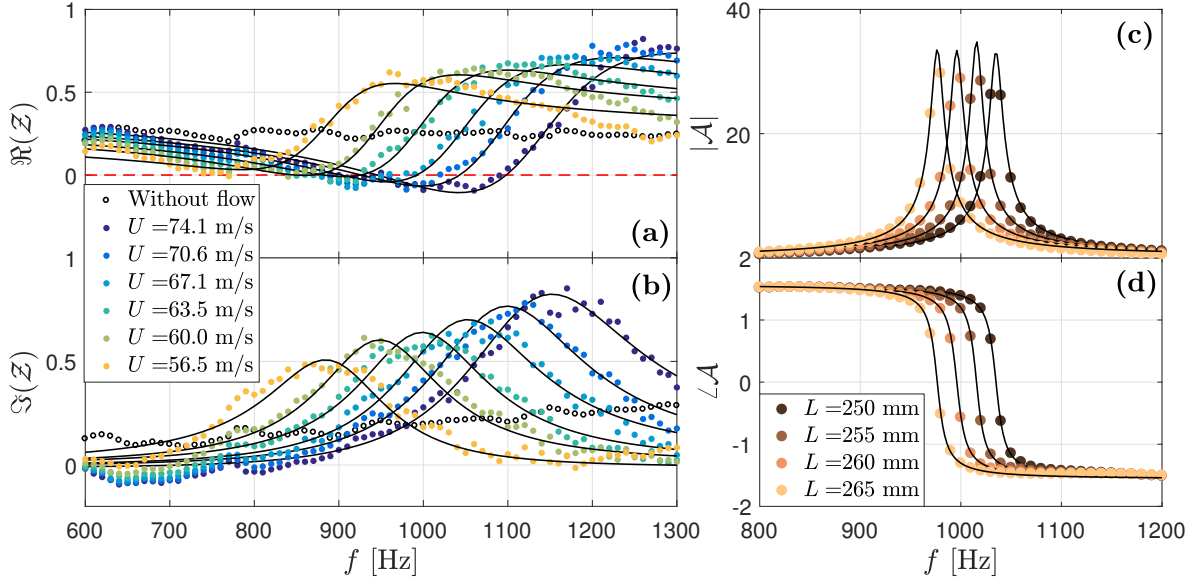
Figure 4.6: **(a)** and **(b)**: Specific resistance $\Re(\mathcal{Z})$ and reactance $\Im(\mathcal{Z})$ of the cavity opening along which the shear layer develops for several bulk flow velocities U and for excitation amplitude 20Pa. The black lines correspond to the fits based on Eq. (4.1). The red dotted line in **(a)** highlights the presence of frequency ranges for which the resistance is negative, which means that reflected waves g exhibit higher amplitude than incident waves f (necessary condition for an aeroacoustic instability in the configuration of Figure 4.1). **(c)** and **(d)**: Modulus and phase of the specific admittance of the deep cavity for different lengths L. The black lines correspond to the fits based on Eq. (4.2).

accounted for in this simplified model.

In presence of the shear layer, the specific impedance of the cavity opening is significantly affected. One can see in Figure 4.6**(a)** and 4.6**(b)** that the specific resistance and reactance both exhibit a frequency dependence oscillating around the values obtained without channel flow, which is typical of the impedance of side-branches subject to grazing flow [83]. This is due to the response of the first longitudinal aerodynamic mode to the incident acoustic wave of complex amplitude f. Further insights about the nonlinear aerodynamic response of this shear layer when it is subject to incident acoustic waves are provided in the study from Boujo *et al.* [20]. One can see in Figure 4.6**(a)** that for each velocity U, there exists a resistance minimum, which corresponds to the eigenfrequency f_1 of this aerodynamic eigenmode. The frequency of the minimum of $\Re(\mathcal{Z})$ increases linearly with the flow velocity, scaling with a Strouhal number $St_1 = f_1 W/U \approx 0.4$, which has been already observed in several works on the topic [42]. This corresponds to flow perturbations originating from the upstream corner that travel at about $0.4\,U$ across the opening during one acoustic oscillation cycle. The advection speed of the perturbations is roughly equal to the mean value of the velocity across the shear layer, which ranges from very low velocities in the cavity to the bulk velocity U

in the mean channel (see Figure 4.4).

It is important to note that the specific resistance minimum becomes negative for velocities exceeding 65 m/s. In fact, when the reflection coefficient satisfies $|\mathcal{R}| = |g/f| > 1$, then $\Re(\mathcal{Z}) < 0$, which is a necessary condition for self-sustained aeroacoustic oscillations in the configuration presented in Figure 4.1. It occurs (i) if the time and spatially averaged projection of the unsteady component of the Lamb vector $(\boldsymbol{\omega} \times \boldsymbol{v})'$ onto the acoustic field is positive ($\boldsymbol{\omega} = \boldsymbol{\nabla} \times \boldsymbol{v}$ is the vorticity), which corresponds to acoustic energy production according to the Howe's energy corollary [73], and (ii) if this acoustic energy production exceeds the radiation losses in the wind channel. Readers interested by the space-time evolution of the unsteady component of the Lamb vector in a similar configuration (self-sustained aeroacoustic oscillations of a bottle whose neck is subject to a grazing flow) can refer to the recent work from Boujo *et al.* [21]. In the present study, the measured specific impedance is fitted using the following second order transfer function

$$\mathcal{Z}(s) = \frac{\hat{p}}{\rho c \hat{u}} = n \frac{s^2 + 2ms + \omega_l^2}{s^2 + 2ds + \omega_r^2},\tag{4.1}$$

with $s = i\omega$ the Laplace variable ($\omega = 2\pi f$ is the angular frequency), n the gain, m and d the damping coefficients, and ω_l and ω_r the left and right angular frequencies associated with the response of the aerodynamic mode. For each bulk flow velocity, optimization of these parameters is performed in order to find the best fit of the measured specific impedance over the frequency range of interest. The results are presented in Figure 4.6(a) and 4.6(b) where the solid lines show the best fits.

As a further step, these optimized model parameters can be linked to the system parameters (U, W and c) in the form of non-dimensional numbers. First, very good estimates of gains n can be obtained using the relationship $n_0 = n/M^2 = 11.8$, where $M = U/c$ is the Mach number. Second, the parameters m and d providing best impedance predictions can be very well approximated using $d_1 = dW/U = 0.273$ and $m_1 = mWM^3/c = 2.75 \times 10^{-4}$. Third, the left and right angular frequencies $\omega_l = 2\pi f_l$ and $\omega_r = 2\pi f_r$ can be deduced from the following Strouhal numbers $St_l = f_l W/U = 0.375$ and $St_r = f_r W/U = 0.461$. It is important to mention that the values obtained here for n_0, d_1, m_1, St_l and St_r cannot be generalised because they depend on the detail of the side-branch geometry and on the turbulent boundary layer thickness in the channel upstream of the cavity. It is for instance expected that they would differ for other shapes of the cavity opening, e.g. with round corners. Another important point to mention is that this model for the specific impedance of the cavity opening subject to grazing flow can only capture the effect of one of the shear layer's aerodynamic eigenmode.

Having found a suitable model for the specific impedance of the cavity opening, one now focuses on the modelling of the cavity's specific admittance at $y = 0$, whose measured modulus and phase are shown in Figure 4.6(c) and 4.6(d). The specific admittance $\mathcal{A}$ is governed by the quarter wave resonances of the deep cavity, which occur at frequencies

$f_n = (2n + 1)c/4L$. Since we focus here on only one of these resonances, it is natural to consider the simple transfer function

$$A(s) = \frac{\rho c \hat{u}}{\hat{p}} = -\frac{\gamma s}{s^2 + 2\alpha s + \omega_a^2}, \tag{4.2}$$

where γ is a gain, which is equal to $2c/L$ as shown in section 2.2, α is the acoustic damping in the cavity and ω_a is the angular frequency of the three-quarter wave resonance of the deep cavity. Using the measured specific admittance (colored dots in Figure 4.6(**c**) and 4.6(**d**)) and setting $\gamma = 2c/L$ and $\omega_a = 3\pi c/2L$ (as in section 2.2.1), it is found that a damping $\alpha \simeq 40$ rad/s provides an excellent match between the measured A and the above transfer function model (solid lines) for the range of deep cavity length considered in this work.

Combining Eqs. (4.2) and (4.1), and expressing these transfer functions in the time domain, one obtains the following system of differential equations for the acoustic pressure p and the acoustic velocity u at the cavity opening:

$$\begin{cases} \ddot{p} + 2d\,\dot{p} + \omega_r^2\, p = n(\ddot{u} + 2m\,\dot{u} + \omega_l^2\, u) \\ \\ \ddot{u} + 2\alpha\,\dot{u} + \omega_a^2\, u = -\gamma\,\dot{p}. \end{cases} \tag{4.3}$$

Using the second equation to express the second time derivative of the acoustic velocity $\ddot{u}$ in the first equation, the system can be rewritten as

$$\begin{cases} \ddot{p} + 2\beta\,\dot{p} + \omega_r^2\, p = \mu\dot{u} + \sigma u \\ \\ \ddot{u} + 2\alpha\,\dot{u} + \omega_a^2\, u = -\gamma\dot{p}, \end{cases} \tag{4.4}$$

with $\beta = (2d + n\gamma)/2$, $\mu = 2n(m - \alpha)$ and $\sigma = n(\omega_l^2 - \omega_a^2)$. This system of oscillators with resistive and reactive coupling depends on a set of a parameters, whose values are directly linked, as described above, to the physical parameters U, L and W. It will now be used to predict the aeroacoustic stability of the deep cavity subject to grazing turbulent flow.

4.3.2 Linear stability analysis

Using $\boldsymbol{x} = (u, p)^T$, the system is expressed in the following matrix form

$$\begin{bmatrix} 1 & 0 \\ 0 & 1 \end{bmatrix} \ddot{\boldsymbol{x}} + \begin{bmatrix} 2\beta & -\mu \\ \gamma & 2\alpha \end{bmatrix} \dot{\boldsymbol{x}} + \begin{bmatrix} \omega_r^2 & -\sigma \\ 0 & \omega_a^2 \end{bmatrix} \boldsymbol{x} = 0. \tag{4.5}$$

The linear stability depends on the sign of the real part of the system's eigenvalues λ, which are the roots of the characteristic polynomial:

$$\lambda^4 + \lambda^3 2(\alpha + \beta) + \lambda^2(\omega_a^2 + \omega_r^2 + 4\alpha\beta + \gamma\mu) + \lambda(2\alpha\omega_r^2 + 2\beta\omega_a^2 + \gamma\sigma) + \omega_r^2\omega_a^2 = 0. \tag{4.6}$$
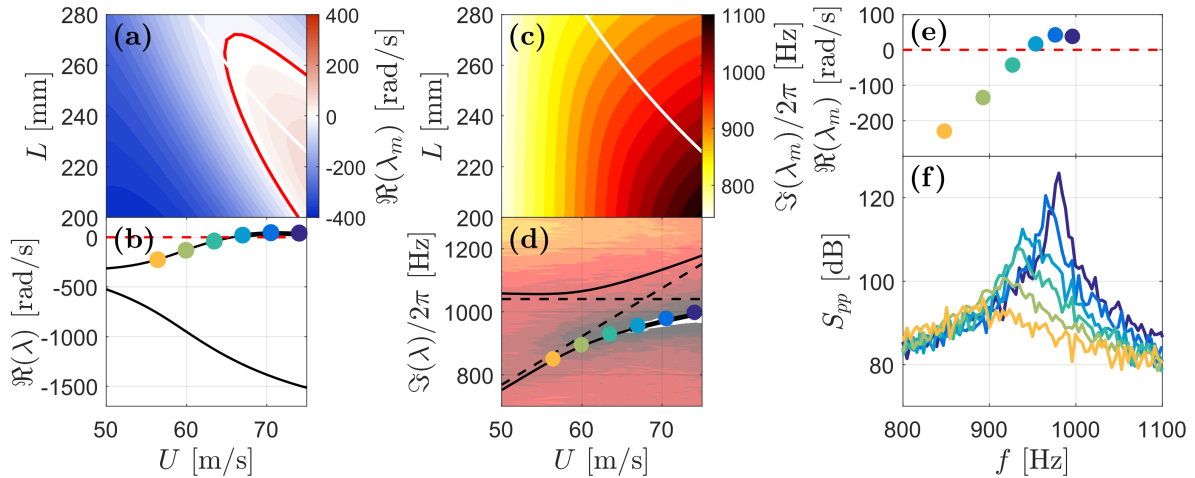
Figure 4.7: Eigenvalues λ of the aeroacoustic system for a range of U and L. These eigenvalues are the roots of (4.6). **(a)** Map of the real part (growth rate) of the largest eigenvalue λ_m as function of L and U. The linear stability limit is drawn in red, and the line where $\omega_a = \omega_r$ in white. **(b)** $\Re(\lambda)$ for $L = 250$ mm as function of U (black lines). The stability limit is drawn as dashed red line, and the coloured circles correspond to the eigenvalues with the largest real part, at the values of U considered in Figure 4.6. **(c)** Map of the imaginary part (frequency) of the most unstable eigenvalue λ_m. **(d)** $\Im(\lambda)$ for $L = 250$ mm as function of U (black lines), superimposed with the acoustic mapping of Figure 4.2. The black dashed lines correspond to the frequencies of each oscillator of the coupled system: ω_a (horizontal line) and ω_r (linearly increasing with U). The coloured circles correspond to the most unstable eigenvalues λ_m at the values of U considered in Figure 4.6. **(e)** Prediction of the most unstable eigenvalue for the velocities considered in Figure 4.6. **(f)** Corresponding experimental spectra for $L = 250$mm and for these velocities.

Based on the previously identified scaling laws for the parameters of the linear model, the polynomial roots are computed for a range of bulk flow velocity U and deep cavity length L. These roots are two pairs of complex conjugate eigenvalues, of which only the ones with positive imaginary part, i.e. positive angular frequency, are presented in Figure 4.7. Several comments are now made about this figure.

Firstly, the predicted linear stability of the aeroacoustic system for varying L and U is presented in Figure 4.7$\mathbf{(a)}$ and 4.7$\mathbf{(c)}$. The former and the latter subfigures respectively show the real and imaginary parts (linear growth rate and oscillation frequency) of the most unstable of the two eigenvalues, which is denoted λ_m. The red line indicates the stability limit $\Re(\lambda_m) = 0$. It shows that, for $L < 270$ mm and $U > 65$ m/s, the system is linearly unstable around the white line indicating coincidence of the resonance frequency of the deep cavity ω_a, which governs the oscillator equation for the acoustic velocity, and of the resonance frequency of the shear layer ω_r, which governs the oscillator equation for the acoustic pressure.

Secondly, a subset (for $L = 250$ mm) of the predicted system eigenvalues λ is presented in Figures 4.7$\mathbf{(b)}$ and 4.7$\mathbf{(d)}$. In the former subfigure, one of the eigenvalues has a significantly smaller real part for the considered range of U, which implies that it is much more stable than the other. The eigenvalue with the largest real part crosses the complex plane imaginary axis when $U \simeq 65$ m/s, i.e. the system becomes linearly unstable beyond this bulk flow velocity. In Figure 4.7$\mathbf{(d)}$, the excellent match between the peak frequency of the overlayed power spectral density and the frequency of the least-stable eigenvalue indicates that the present coupled oscillators model performs very well. Moreover, in contrast with the phenomenon of *frequency lock-in* in flow-induced vibrations problems, which are also modelled as coupled oscillators [44,97,119,168], the frequencies of the eigenvalues $\Im(\lambda)$ do not merge in the range of L and U for which the present aeroacoustic system is linearly unstable. Indeed, the black lines corresponding to the root loci are repelled from the intersection point of the natural frequencies of the two oscillators (dashed black lines).

The fundamental topological difference of the coupled-oscillator root loci between flow-induced vibration problems and aeroacoustic instabilities of deep cavities subject grazing flow originates from the differences in stability and coupling nature of the coupled-oscillators model. In the case of the flow-induced vibration problems, the hydrodynamic oscillator is linearly unstable and it is typically modelled as a Van-der-Pol oscillator [97], the mechanical oscillator is linearly stable and their coupling is usually purely reactive. In the present case of aeroacoustic instabilities of deep cavities, which we model in this section with the system (4.4), both oscillators are linearly stable and the system can become linearly unstable because of the presence of both resistive and reactive coupling terms.

Finally, in Figure 4.7$\mathbf{(e)}$, the most unstable eigenvalue λ_m is plotted in the complex plane for the velocities considered in Figure 4.6) and for $L = 250$ mm. These eigenvalues can be compared with the corresponding experimental power spectral densities for the
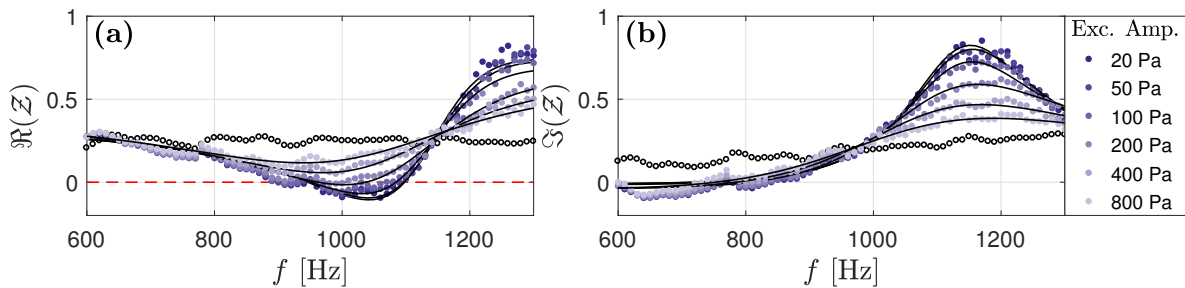
Figure 4.8: **(a)** Real and **(b)** imaginary part of the specific impedance of the cavity opening for different acoustic forcing amplitudes and for $U = 74$m/s. The white circles correspond to the specific impedance without flow.

same velocities U that are presented in Figure 4.7**(f)**. The good agreement in terms of frequency and the sharpening of the peak for $U > 65$ m/s again contribute to the linear model validation.

4.4 Nonlinear deterministic model

The nonlinearities of the system are now investigated and modelled. To that end, measurements of the specific acoustic impedance and admittance at relevant acoustic amplitudes are performed. Considering that the admittance of the cavity does not feature any noticeable dependance on the acoustic level at forcing amplitudes that corresponds to observed aeroacoustic limit cycles, it is considered in the remainder of this chapter as a linear oscillator.

4.4.1 Describing function analysis

Impedance measurements of the cavity opening are performed with the setup shown in Figure 4.5**(b)** for a range of forcing amplitude. This forcing amplitude is deduced from the multi-microphone method and corresponds to the amplitude at a pressure antinode. The results of these measurements for $U = 74$ m/s are presented in Figure 4.8**(a)** and 4.8**(b)**, respectively showing $\Re(\mathcal{Z})$ and $\Im(\mathcal{Z})$. For increasing amplitude, there is a monotonous decrease of the deviation of the specific impedance from the one without flow, which shows that the shear layer responds with less strength to the acoustic forcing. The underlying mechanism has been presented by Boujo *et al.* [20] for $U = 56$ m/s and is in line with previous work on the subject: as the forcing amplitude grows, coherent Reynolds stresses thicken the mean shear layer, which reduces the potential for perturbation amplification at the forcing frequency. As a consequence, the range across which the real part of the impedance is negative reduces progressively as the amplitude increases. It is seen that beyond a forcing amplitude of 200 Pa, $\Re(\mathcal{Z})$ is positive for the whole frequency range. Noticeably, in the range 800 Hz to about 1150 Hz, for which the shear layer produces acoustic energy, this contribution is less
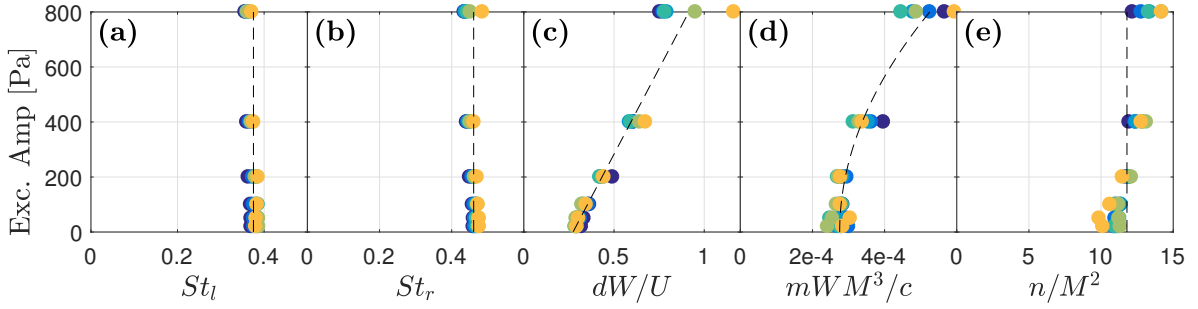
Figure 4.9: Non-dimensional numbers, which link the system parameters U, W and c to the optimized model parameters ω_l, ω_r, d, m and n as function of the acoustic forcing amplitude. The symbols are coloured with the same colour code for the bulk flow velocity U as in Figure 4.6. The dashed lines show the scaling laws used in the model of subsection 4.4.2. **(a)** and **(b)** respectively show $St_l = \omega_l W/2\pi U$ and $St_r = \omega_r W/2\pi U$ that are assumed independent of the forcing amplitude in subsection 4.4.2. **(c)** shows dW/U and the scaling law used in subsection 4.4.2: $dW/U = d_1 + d_2|p|$. **(d)** shows mWM^3/c and the scaling law used in subsection 4.4.2: $mWM^3/c = m_1 + m_3p^2$. **(e)** shows $n_0 = n/M^2$ that is assumed constant in subsection 4.4.2.

energetic than the radiation losses to the wind channel, and consequently, $\Re(\mathcal{Z}) > 0$ and the modulus of the reflection coefficient $|\mathcal{R}|$ is lower than 1.

As in subsection 4.3.1, for each forcing amplitude, the parameters of the transfer function given in Eq. (4.1) are optimized to best fit the measured specific impedance $\mathcal{Z}$ over the frequency range presented in Figure 4.8**(a)** and 4.8**(b)**. The solid lines in this figure show these best fits. This optimization has also been performed with measurements of the specific impedance for the same set of bulk flow velocities as in Figure 4.6. For each forcing amplitude, the optimized model parameters (d, m, n, ω_l and ω_r) were linked to the system parameters U, W and c with the scaling laws presented in subsection 4.3.1. The non-dimensional numbers with which these optimized model parameters can be deduced, are presented as coloured dots in Figure 4.9 for several acoustic forcing amplitudes, with the same colour code for the bulk flow velocity U as in Figure 4.6.

Based on this data, it is possible to perform a describing function analysis for predicting the amplitude of the aeroacoustic limit cycle, as it was done by Noiray *et al.* [131] in the case of a thermoacoustic instability. In the present situation, it is possible to predict the limit cycle amplitude and frequency as function of the cavity length L, as in [131], and thanks to the model and the identified scaling laws for its parameters, one can also construct bifurcation diagrams as function of the bulk flow velocity in the channel U. This is now performed for $L = 250$ mm and $U = 74$ m/s: the eigenvalues of the coupled system (4.4) are computed using the optimized model parameters. For each of the forcing amplitude, the real and imaginary part of the most unstable eigenvalue λ_m are displayed in Figures 4.10**(a)** and 4.10**(b)**.
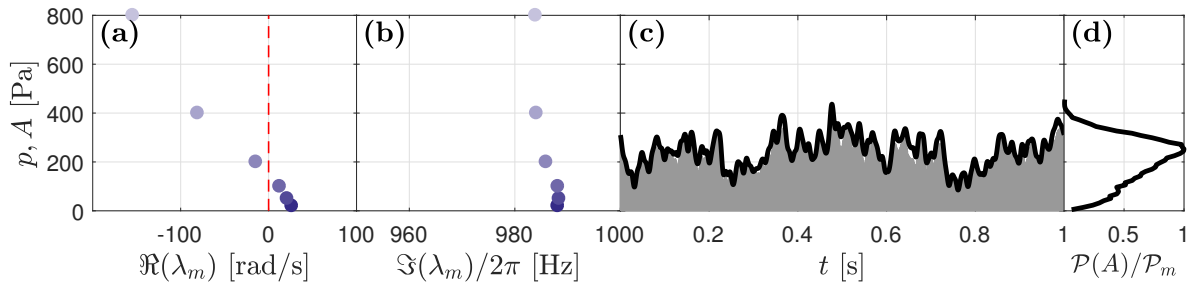
Figure 4.10: **(a)** Real and **(b)** imaginary part of the most unstable eigenvalue from system (4.5) as function of the acoustic amplitude for $L = 250$ mm and $U = 74$ m/s. The eigenvalues are the roots of (4.6) in which the optimized model parameters ω_l, ω_r, d, m and n (dark blue circles in Figure 4.9) were set. **(c)** Acoustic pressure filtered around the limit cycle frequency as done in Figure 4.2**(d)** (gray line, only $p > 0$ is shown), and corresponding envelope A (thick black line), for $L = 250$ mm and $U = 74$ m/s. **(d)** Probability density function (PDF) of the acoustic signal envelope $\mathcal{P}(A)$.

When the amplitude increases, the linear growth rate of the system monotonically decreases while the oscillation frequency does not significantly vary. The linear growth rate is positive at very low amplitude (about 20 rad/s) and according to the describing function framework, the aeroacoustic system becomes marginally stable when the real part of λ_m vanishes, which in the present case occurs for about 150 Pa. This predicted limit cycle amplitude is now compared to the actual self-sustained oscillation amplitude, which is measured for $L = 250$ mm and $U = 74$ m/s using the experimental setup presented in Figure 4.1. This comparison can be done with Figure 4.10**(c)** and 4.10**(d)**, which respectively show the band-pass filtered acoustic signal measured at a pressure antinode (only the positive acoustic pressure fluctuations are shown on this figure), and the probability density function (PDF) of the signal's envelope.

One can draw the following conclusions from Figure 4.10: First, this describing function analysis provides a realistic estimate of the limit cycle amplitude (about 150 Pa), but it cannot be used for a quantitative prediction of the most probable amplitude (about 250 Pa). Second, the deterministic and frequency-domain describing-function-framework cannot capture the significant random fluctuations of the aeroacoustic limit cycle amplitude that are induced by the forcing from the intense turbulence in the channel. The next section aims at filling this gap by considering a nonlinear time-domain analysis of the problem and the turbulent stochastic forcing will be accounted for in section 4.5.

4.4.2 Time-domain model of coupled oscillators

The starting point of this section is the time domain model (4.4) of the two coupled linear oscillators developed in section 4.3. One now aims at incorporating into this model relevant nonlinear terms on the basis of the specific impedance measurements

presented in the previous section.

One can deduce from the model parameters, which were optimized to reproduce the specific impedance for different forcing amplitudes and flow velocities, scaling laws that not only depend on the system parameters, but also on the acoustic amplitude. These scaling laws are presented as dashed lines in Figure 4.9. Considering that St_l, St_r and n_0 do not vary significantly with the acoustic forcing, and that they are respectively equal to 0.375, 0.461 and 11.8, the same simple laws as in subsection 4.3.1 are used in the next sections: $\omega_l = 2\pi St_l U/W$, $\omega_r = 2\pi St_r U/W$ and $n = n_0 M^2$.

On the other hand, one can see in Figure 4.9(c) and 4.9(d) that the values of dW/U and mWM^3/c significantly depend on the acoustic amplitude, and they can be respectively approximated by a linear and quadratic regression (dashed lines). Therefore, the model parameters m and d are respectively deduced from the $dW/U = d_1 + d_2|p|$ with $d_1 = 0.273$ and $d_2 = 8.03\times10^{-4}$ Pa^{-1}, and from $mWM^3/c = m_1+m_3 p^2$ with $m_1 = 2.75\times10^{-4}$ and $m_3 = 3.90 \times 10^{-10}$ Pa^{-2}. These scaling laws are now incorporated to the time-domain model which becomes:

$$\begin{cases} \ddot{p} + 2(\beta_1 + \beta_2|p|)\ \dot{p} + \omega_r^2\ p = (\mu_1 + \mu_3 u^2)\dot{u} + \sigma u \\[2mm] \ddot{u} + 2\alpha\ \dot{u} + \omega_a^2\ u = -\gamma\dot{p}, \end{cases} \tag{4.7}$$

with

$$\begin{aligned} \beta_1 &= \frac{U}{W}d_1 + \frac{\gamma M^2}{2}n_0, \quad \beta_2 = \frac{U}{W}d_2, \quad \mu_1 = 2n_0 M^2\left(\frac{c}{WM^3}m_1 - \alpha\right), \quad \gamma = \frac{2c}{L} \\[2mm] \mu_3 &= (\rho c)^2\frac{2c}{WM}n_0 m_3, \quad \sigma = n_0 M^2\left(\left[2\pi\frac{U}{W}St_l\right]^2 - \omega_a^2\right), \quad \omega_r = 2\pi\frac{U}{W}St_r. \quad (4.8) \end{aligned}$$

It can be noted (i) that the increase of the acoustic pressure amplitude p leads to an increase of the effective damping coefficient $(\beta_1+\beta_2|p|)$ of the second oscillator, which is associated with the lower receptivity of the thickened shear layer at higher amplitude, and (ii) that the increase of the acoustic velocity amplitude u yields an increase of the effective resistive coupling coefficient $(\mu_1 + \mu_3 u^2)$.

This nonlinear deterministic model of coupled oscillators for describing the aeroacoustic dynamics of the deep cavity depends on a set of constants $(n_0, d_1, d_2, m_1, m_3, St_l, St_r$ and $\alpha)$ that were quantified from measurements, and on the system parameters ρ, U, c, L, W and the Mach number $M = U/c$. One also recalls that the angular frequency of the three-quarter wave resonance is $\omega_a = 3\pi c/2L$. Before augmenting this model in section 4.5 with stochastic forcing from turbulence in order to explain the random fluctuations of the limit cycle amplitude, the amplitude and phase equations of this deterministic model are derived and analysed in the next section.

4.4.3 Amplitude and phase equations

The averaging procedure of Krylov & Bogoliubov [95] is now applied to the system of coupled oscillators (4.7) in order to obtain first order differential equations for the oscillation amplitude and phases. One assumes that oscillations occur at ω and that this angular frequency satisfies $\omega \simeq \omega_a \simeq \omega_r$ and $\omega_a + \omega_r \simeq 2\omega$. The following ansatz for the acoustic velocity and pressure are used:

$$\begin{cases} p = A\cos(\omega t + \varphi_A) = \dfrac{1}{2}(ae^{i\omega t} + a^*e^{-i\omega t}) & \text{with} \quad a = Ae^{i\varphi_A}, \\ u = B\cos(\omega t + \varphi_B) = \dfrac{1}{2}(be^{i\omega t} + b^*e^{-i\omega t}) & \text{with} \quad b = Be^{i\varphi_B}, \end{cases} \tag{4.9}$$

where A represents the pressure amplitude, and B the velocity amplitude, and φ_A and φ_B their phase. This averaging approach can only be applied if the oscillation amplitudes and phases vary slowly with respect to the acoustic period, which is satisfied in the present problem, and which corresponds to damping and coupling terms that are small compared to the inertial and stiffness terms of the two oscillator equations. Assuming that the first derivative of the acoustic pressure can be written as

$$\dot{p} = \frac{i\omega}{2}(ae^{i\omega t} - a^*e^{-i\omega t}), \tag{4.10}$$

which implies, as explained by Balanov *et al.* [5], that $\dot{a}e^{i\omega t} + \dot{a}^*e^{-i\omega t} = 0$, one can express the second time derivative of the acoustic velocity as

$$\ddot{p} = i\omega\dot{a}e^{i\omega t} - \frac{\omega^2}{2}(ae^{i\omega t} + a^*e^{-i\omega t}). \tag{4.11}$$

Following the same procedure for p, substituting these expressions into the first oscillator equation of (4.7), multiplying by $e^{-i\omega t}/i\omega$, integrating over one cycle, dividing by $e^{i\varphi_A}$ and taking the real and imaginary part of the equation yields

$$\begin{cases} \dot{A} = -\beta_1 A - \beta_2\dfrac{4}{3\pi}A^2 + \left(\dfrac{\mu_1}{2} + \dfrac{\mu_3}{8}B^2\right)B\cos(\varphi_A - \varphi_B) - \dfrac{\sigma}{2\omega}B\sin(\varphi_A - \varphi_B), \\ \dot{\varphi}_A = \dfrac{\omega_r^2 - \omega^2}{2\omega} - \left(\dfrac{\mu_1}{2} + \dfrac{\mu_3}{8}B^2\right)\dfrac{B}{A}\sin(\varphi_A - \varphi_B) - \dfrac{\sigma}{2\omega}\dfrac{B}{A}\cos(\varphi_A - \varphi_B). \end{cases} \tag{4.12}$$

Similar treatment of the second oscillator equation in (4.7) yields:

$$\begin{cases} \dot{B} = -\alpha B - \dfrac{\gamma}{2}A\cos(\varphi_A - \varphi_B), \\ \dot{\varphi}_B = \dfrac{\omega_a^2 - \omega^2}{2\omega} - \dfrac{\gamma}{2}\dfrac{A}{B}\sin(\varphi_A - \varphi_B). \end{cases} \tag{4.13}$$
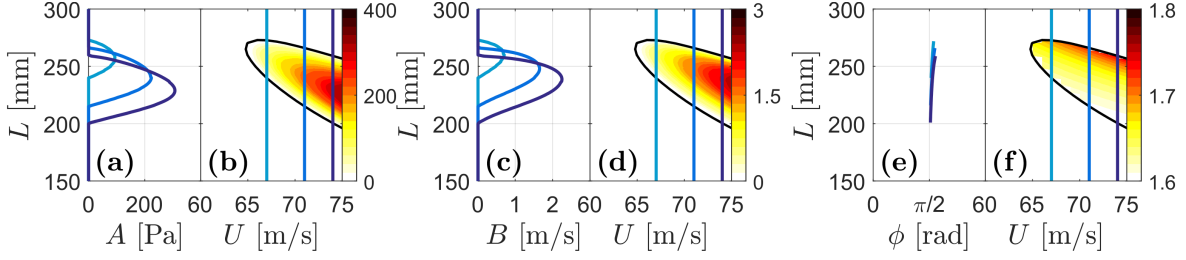
Figure 4.11: **(b)**, **(d)** and **(f)**: Limit cycle amplitudes A and B and phase difference ϕ as function of L and U. They are fixed points of the slow-flow equations (4.14) and they were obtained by searching the zeros of the right-hand-side of these equations. The origin is the only fixed point in the white region delimited by the stability border presented in Figure 4.7. **(a)**, **(c)** and **(e)**: Cuts showing the limit cycle amplitude for $U = 67$, 70 and 74 m/s as function of L.

Defining the phase difference $\phi = \varphi_A - \varphi_B$ yields the following system of three coupled equations for the slowly varying amplitudes and the phase of the coupled oscillators:

$$\begin{cases} \dot{A} = -\beta_1 A - \beta_2 \dfrac{4}{3\pi} A^2 + \left(\dfrac{\mu_1}{2} + \dfrac{\mu_3}{8} B^2 \right) B \cos \phi - \dfrac{\sigma}{2\omega} B \sin \phi, \\[2mm] \dot{B} = -\alpha B - \dfrac{\gamma}{2} A \cos \phi, \\[2mm] \dot{\phi} = \Delta\omega + \left(\dfrac{\gamma}{2} \dfrac{A}{B} - \left(\dfrac{\mu_1}{2} + \dfrac{\mu_3}{8} B^2 \right) \dfrac{B}{A} \right) \sin \phi - \dfrac{\sigma}{2\omega} \dfrac{A}{B} \cos \phi, \end{cases} \tag{4.14}$$

with $\Delta\omega = (\omega_r^2 - \omega_a^2)/2\omega \simeq \omega_r - \omega_a$ the detuning constant. The fixed points of this system of first order differential equations are found by searching for amplitudes and phase difference that cancel the right-hand-side expressions of (4.14) and that thus lead to $\dot{A} = \dot{B} = \dot{\phi} = 0$. For a few combinations of L and U, this search is initialised from the amplitudes A and B and phase difference ϕ of limit cycles that were computed by integrating the second order system (4.7). The fixed points of the slow-flow system (4.14) are then obtained for the full range of L and U by continuation of the local minimum search from neighbouring solutions.

The results are presented in Figure 4.11, which shows the acoustic pressure amplitude A, the acoustic velocity amplitude B that is afterward compared with experimental data, and their phase difference ϕ at conditions featuring aeroacoustic limit cycles. These results show that, according to this deterministic model, the deep cavity subject to turbulent grazing flow undergo *supercritical* Hopf bifurcations only. This is further illustrated in Figure 4.11**(a)** and 4.11**(b)** for three values of the bulk velocity U. One can see that over the entire range of combinations of L and U leading to limit cycles, the phase difference between the acoustic pressure p and the acoustic velocity u is nearly constant and slightly above $\pi/2$, which is typical of standing mode oscillations in quarter wave resonators.

In Figure 4.12**(a)**, the limit cycle amplitude A, which is predicted from the slow-flow
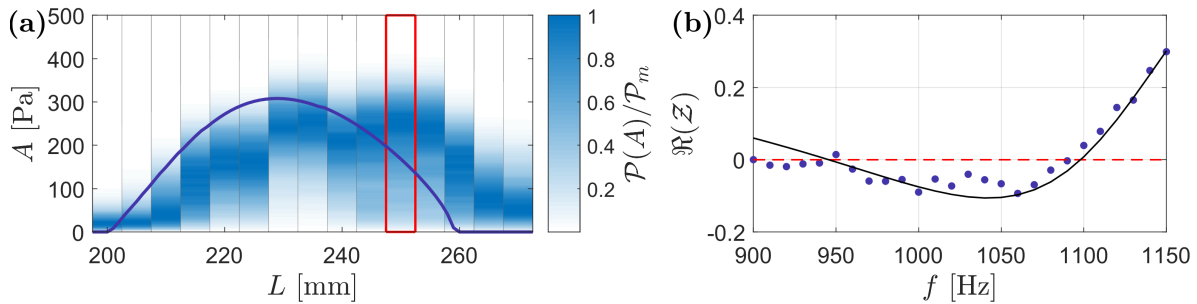
Figure 4.12: **(a)** PDFs of the envelope of the band-pass-filtered acoustic pressure for several cavity lengths L, compared to the predicted bifurcation diagram of the slow-flow system (4.14), which shows the limit cycle amplitude A for $U = 74$ m/s as function of L. For each L, the PDF is normalized by its maximum $\mathcal{P}_m$. The one in the red rectangle is also shown in Figure 4.10**(d)**. **(b)** Comparison between the measured and modeled specific resistance of the opening for $U = 74$m/s and excitation amplitude 20Pa. This is a close-up view of data presented in Figure 4.8 in order to highlight the smoothness of the modelled $\Re(\mathcal{Z})$.

system (4.14) for $U = 74$m/s and for several cavity lengths L, is compared to the probability density function (PDF) of the band-pass-filtered acoustic pressure envelope measured with the experimental setup shown in Figure 4.1. The overall agreement between model predictions and most probable amplitude from the experiments is very good, albeit the former displays a smoother dependance on the cavity length L, with bifurcation points shifted by about 10 mm. These differences are due to the fact that the actual specific impedance is not as smooth as the second order transfer function adopted here to model it (see Figure 4.12**(b)** showing $\Re(\mathcal{Z})$ for $U = 74$ m/s). Indeed, the details of the system dynamics are not fully retrieved by the model (4.7) and its corresponding slow-flow dynamics (4.14), but on the other hand, it gives a good estimate of the most probable limit-cycle amplitude over the full range of cavity length L and channel velocity U with a single set of parameters.

4.5   Intermittently unstable aeroacoustic feedback

In this section, the model complexity is further increased by adding stochastic forcing to the deterministic dynamic system (4.7), in order to capture the random fluctuations of the limit cycle amplitude, the intermittently unstable aeroacoustic feedback and the associated PDFs of the acoustic pressure. As shown in Figure 4.10**(c)** with the time trace of the band-pass filtered acoustic pressure signal, these fluctuations can have significant amplitudes. As shown in Figure 4.10**(d)**, they lead to broad distributions $\mathcal{P}(A)$ of the acoustic pressure amplitude A, which contrasts with the Dirac distributions that are found, for each combination of L and U, in the deterministic description of the problem. This is also illustrated in Figure 4.13 that presents the PDFs of the
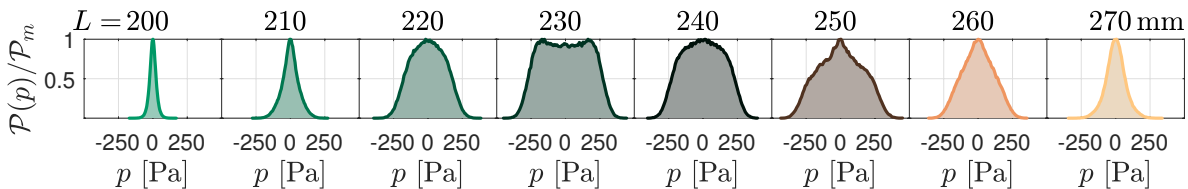
Figure 4.13: PDFs of the band-pass-filtered acoustic pressure $\mathcal{P}(p)$ for $U = 74$ m/s and several cavity length L. The corresponding PDFs of the signal envelope are given in Figure 4.12**(a)** with colour gradients.

band-pass-filtered acoustic pressure $\mathcal{P}(p)$ for $U = 74$ m/s and several cavity length L.

In a deterministic scenario, the PDFs would be (i) the Dirac distribution $\delta(p)$ for $L = 200$ mm and 270 mm, for which the aeroacoustic system is presumably linearly stable, and (ii) the distribution of pure sine waves (i.e. $\mathcal{P}(p) = 1/(\pi\sqrt{1 - (p/a)^2})$ with $p = a\sin\omega t$ and a constant) for the other lengths, for which the system apparently exhibits stable limit cycles. The actual distributions in Figure 4.13 are obviously significantly different from the latter ones, indicating that stochastic forcing from the turbulence should be added to the model.

4.5.1 Intermittency modelled with randomly-forced coupled oscillators

The Gaussian-like PDFs of the presumably aeroacoustically stable cases ($L = 200$ and 270 mm in Figure 4.13) can justify incorporating additive stochastic forcing to the deterministic model (4.7). Indeed, linearly stable oscillators that are subject to additive white noise forcing display such Gaussian-like PDFs. Furthermore, the PDFs of the acoustic pressure for $L = 220$ and 230 mm are typical of marginally stable oscillators and weakly nonlinear self-sustained oscillators subject to additive white noise forcing [22]. This random additive forcing at the side-branch cavity opening can be attributed to the broadband noise generated by the highly turbulent flow in the wind channel and its air supply line. Therefore, we add a Gaussian additive white noise $\xi(t)$ of intensity Γ_ξ to the right hand side of the equation for u in the system of coupled oscillators (4.7).

Now, when L is decreased from 270 mm to 260 and then to 250 mm, the base of the PDF thickens. It indicates that the mean acoustic pressure amplitude increases, which can be explained by the crossing of the supercritical Hopf bifurcation that was discussed in the previous sections. However, these two PDFs present distinct features that clearly differ from the ones of weakly nonlinear self-oscillators subject to additive random forcing only. Indeed, there is a central peak remaining, which is the marker of high probability of low acoustic amplitude periods. In fact this is the signature of intermittency between low and high amplitude acoustic oscillations.

As a first remark, the intermittency at play in the present system differs from the one

found in systems that are governed by combined *subcritical*-Hopf and saddle-node bifurcations, and that are subject to purely additive stochastic forcing. A thermoacoustic example of the latter systems was investigated by Bonciolini *et al.* [14] for quasi-steady and finite-rate ramping of the bifurcation parameter. These systems exhibit, for a range of bifurcation parameter values, two basins of attraction between which intermittent jumps can be triggered by the additive random forcing, with resulting PDFs having also a prominent central peak. In contrast, the deterministic model derived in the previous sections on the basis of specific impedance measurements clearly show that the present aeroacoustic system features a *supercritical*-Hopf bifurcation. Consequently, the only possible explanation for the observed intermittency is the presence of parametric noise in the system, which can be linked to the theoretical investigation of Mohamad & Sapsis [118].

Therefore, considering the intense turbulence of the channel flow as well as the low-frequency three-dimensional dynamics of the recirculation region, we propose to include a stochastic component to our bifurcation parameter U, which leads to several terms with stochastic multiplicative forcing. One can note that the low-frequency random fluctuations of the flow at the opening of the deep cavity probably share several features with the ones that were investigated by Basley *et al.* [6] in the case of shallow cavities. Their detailed analysis shows that the broadband slow-fluctuations of the re-circulating flow in *shallow* cavities, which results from centrifugal instabilities, interfere with the (fast) Rossiter modes. In the present *deep* cavity configuration, similar three-dimensional structures may alter the strength of the aeroacoustic coupling at time scales that are long compared to the period of the three-quarter wave acoustic eigenmode. We therefore express the bulk velocity in our low-order model (4.7) and (4.8) as

$$U = \bar{U}(1 + \chi), \tag{4.15}$$

where χ is an Ornstein-Uhlenbeck process obeying the Langevin equation

$$\dot{\chi} = -\frac{\chi}{\tau_\chi} + \zeta_\chi, \tag{4.16}$$

with τ_χ the correlation time of the bifurcation parameter fluctuations and ζ_χ a Gaussian white noise of intensity Γ_χ/τ_χ^2. By incorporating this unsteady formulation of the bulk velocity U, with a mean value $\bar{U}$ and a standard deviation σ_U, into the system of coupled oscillators, the parameters β_1, β_2, μ_1, μ_3, σ and ω_r become time dependent. Using the model coefficients given in subsection 4.4.2, considering $\bar{U} = 74$ m/s and setting $\Gamma_\xi = 5 \times 10^9$ m^2 s^{-6}, $\Gamma_\chi = 5 \times 10^{-3}$ and $\tau_\chi = 0.05$ s, which corresponds to $\sigma_U = \bar{U}\sqrt{\Gamma_\chi/2\tau_\chi} \approx 16$ m s^{-1}, time domain simulations of (4.7) are performed for $L = 245$ and 250 mm. In Figure 4.14, these simulations are compared to the experimental results obtained $L = 255$ and 260 mm. We consider this 10 mm cavity length offset for the comparison because, as it can be seen in Figure 4.12, the predicted bifurcation diagram is staggered by about 10 mm from the experimental data. The parameters defining the additive and multiplicative stochastic forcing, i.e. Γ_ξ, Γ_χ and τ_χ, were
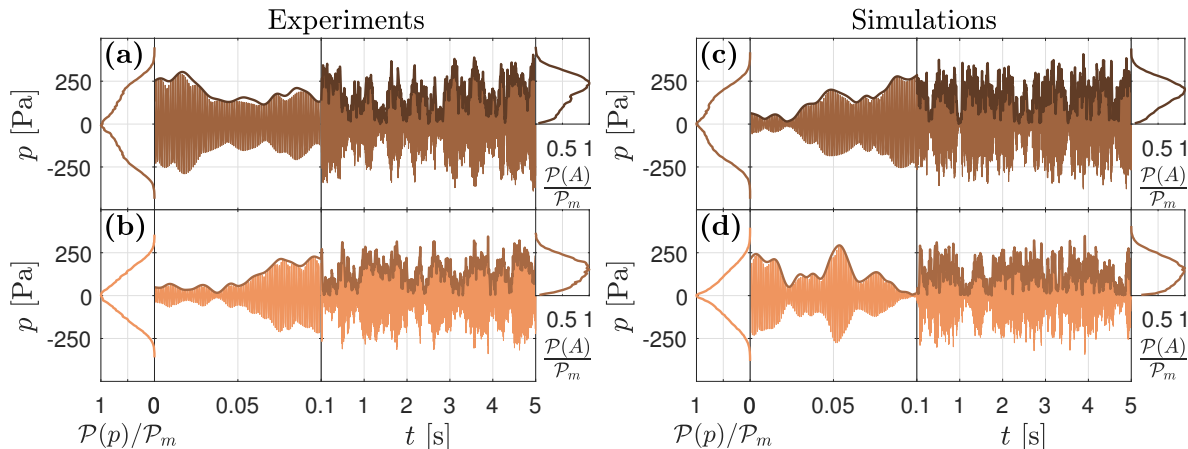
Figure 4.14: Comparison of time traces and PDFs of the acoustic pressure p and its envelope A between experiments (left) and simulations using the coupled stochastic differential equations presented in subsection 4.5.1 (right). The considered mean channel velocity is $\bar{U} = 74$ m/s, and the cavity lengths are $L = 255$, 260, 245 and 250 mm in **(a)**, **(b)**, **(c)** and **(d)** respectively. A 10 mm offset is chosen for this comparison because as shown in Figure 4.12, the predicted bifurcation diagram is staggered by about 10 mm from the experimental data.

empirically adjusted in order to best match the main features of the experimental time traces.

One can see in Figure 4.14 that the model reproduces very well the PDFs of the acoustic pressure p and its envelope B, and especially the central peak of $\mathcal{P}(p)$. The underlying intermittency between periods of low amplitudes and bursts of high amplitude is thus well captured by the model.

It is important to mention that the intensity of the fluctuating component of the bifurcation parameter U is high enough, such that the instantaneous bulk velocity alternately take values in the range for which our model of the aeroacoustic system is linearly stable, and in the one for which it is linearly unstable. Another important point is that the correlation time τ_χ of the bifurcation parameter fluctuations is long enough for the system to adapt to the variations of U. Otherwise, we cannot reproduce with this model the experimentally observed intermittency.

In order to shed light on the conditions leading to these intermittent high amplitude bursts or low-amplitude periods, a simplified model is scrutinized in the following section.

4.5.2 Intermittency modelled with a randomly-forced Van der Pol oscillator

We have established in the previous sections (i) that the present aeroacoustic system is linearly unstable for sufficiently large bulk flow velocity U and for a range of cavity length L, (ii) that at the border of the region corresponding to the limit cycles (red line in Figure 4.7(a)), only supercritical Hopf bifurcations occur, and (iii) that intermittency is induced by parametric noise. To get further insight in the conditions that lead to intermittency, rather than carrying on with the model of coupled oscillators, it is convenient to consider a simpler version of the supercritical Hopf bifurcation with parametric noise. Reckoning with the fact that one of the eigenvalues of (4.7) is very stable (see Figure 4.7(b)), it can be shown that in the vicinity of the Hopf bifurcation, our model of two coupled oscillators for describing the aeroacoustic system can be approximated by a single Van der Pol oscillator subject to additive and multiplicative stochastic forcing. This Van der Pol model is

$$\ddot{\eta} + \left(-2\left[\bar{\nu} + \chi(t)\right] + \kappa\eta^2\right)\dot{\eta} + \omega_0^2\eta = \xi(t), \tag{4.17}$$

where η is a new state variable that represents the aeroacoustic oscillations, ω_0 is the natural frequency of the oscillator, $\nu(t) = \bar{\nu} + \chi(t)$ is the instantaneous linear growth rate, $\kappa > 0$ is the saturation constant, and, as in the previous section, ξ is a Gaussian additive white noise of intensity Γ_ξ, and χ is a coloured Gaussian multiplicative noise, with correlation time τ_χ and equilibrium variance $\sigma_\nu^2 = \Gamma_\chi/2\tau_\chi$, and whose Langevin equation is (4.16).

Time marching of this equation is performed for various combinations of mean linear growth rate $\bar{\nu}$, multiplicative noise correlation time τ_χ and standard deviation σ_ν, in order to illustrate the conditions required for high probability of intermittency. These conditions are set by two non-dimensional parameters: $\bar{\nu}/\sigma_\nu$, which is related to the probability of crossing the stability border, and $\bar{\nu}\tau_\chi$ which compares the characteristic growth or decay time of the oscillation amplitude with the correlation time of the instantaneous growth or decay rate.

The natural frequency of the oscillator is set to $f_0 = \omega_0/2\pi = 1050$ Hz, which is typical of the present aeroacoustic instability. The mean linear growth rate $\bar{\nu}$ is successively set to -30, -8, -4, 4, 8 and 30 rad/s, which are also typical values of the present system in the vicinity of the supercritical Hopf bifurcation, as shown in subsection 4.3.2. The saturation constant is set to $\kappa = 0.01$ s^{-1} for all the simulations such that the resulting oscillation amplitude is of the same order of magnitude as the acoustic pressure in the cavity. The intensity of the additive noise is set to $\Gamma_\xi = 10^{12}$, such that the variance of η for $\bar{\nu} = -30$ rad/s is similar to the variance of the band-pass-filtered acoustic signal for $U \simeq 64$ m/s and $L = 250$ mm. The correlation time τ_χ and variance σ_ν^2 of the multiplicative random forcing χ are changed for each simulation in order to obtain converged PDFs for $\bar{\nu}/\sigma_\nu = -10$, -1, -0.2, 0.2, 1 and 10, and for $|\tau_\chi\bar{\nu}| = 0.1$, 1 and
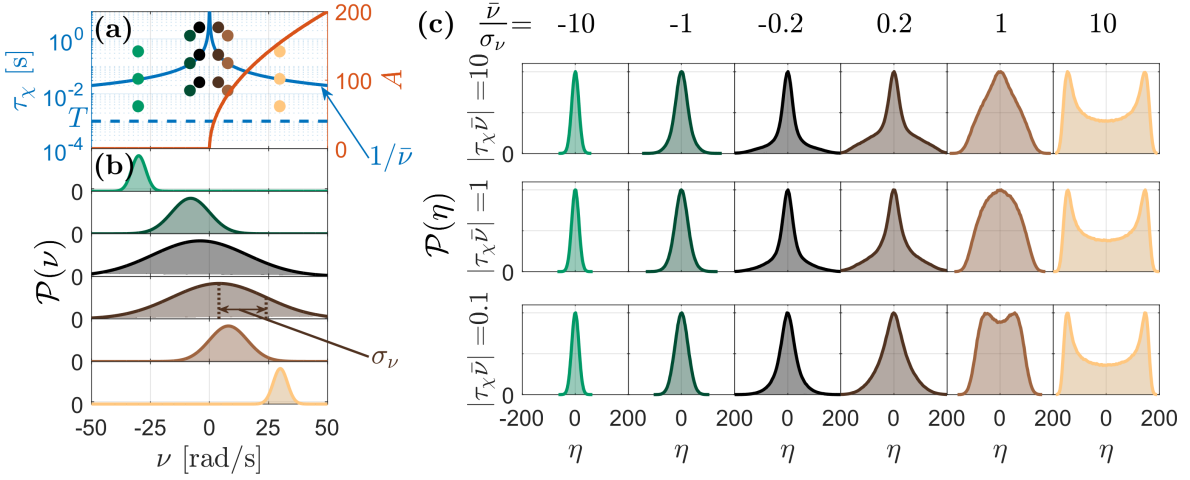
Figure 4.15: **(a)** Bifurcation diagram of the deterministic problem (right axis, red curve), and characteristic times of the stochastic problem (left axis). These characteristic times are (i) the inverse of the mean growth or decay rate of the oscillation amplitude $1/\bar{\nu}$ indicated as a solid blue line, (ii) the oscillation period $T = 2\pi/\omega_0$ indicated as a dashed blue line and (iii) the correlation time τ_χ of the fluctuations of the instantaneous linear growth rate ν. The coloured dots indicate the combinations of τ_χ and $\bar{\nu}$ which were used for the temporal simulations of (4.17), whose PDFs are presented in **(b)** and **(c)**. **(b)** PDFs of the linear growth rate. These Gaussians have a mean $\bar{\nu}$ and a standard deviation σ_ν. **(c)** PDFs of the oscillations for several combinations of $\bar{\nu}/\sigma_\nu$ and $|\tau_\chi\bar{\nu}|$. Rare events are associated to heavy tails indicating high amplitude bursts (e.g. for $\bar{\nu}/\sigma_\nu = -0.2$ and $|\tau_\chi\bar{\nu}| = 10$), or to pronounced central peak indicating sporadic quiet periods (e.g. for $\bar{\nu}/\sigma_\nu = 1$ and $|\tau_\chi\bar{\nu}| = 10$). They reflect the intermittency of the system and they are very likely when $|\tau_\chi\bar{\nu}| \geq O(1)$ and $|\bar{\nu}/\sigma_\nu| \leq O(1)$.

10. The simulated time is 500 s for $|\tau_\chi\bar{\nu}| = 10$ and $\bar{\nu}/\sigma_\nu = -0.2$ and 0.2, and 240 s for the other simulated cases, which is sufficiently long to get converged statistics.

The results of these temporal simulations are gathered in Figure 4.15, which shows the converged PDFs of the state variable η. In this system, the parametric noise adds upon the additive forcing, and its effect is scrutinised in the next paragraphs.

The first necessary condition for intermittency is that the standard deviation σ_ν of the fluctuations of ν is sufficiently large to have ν penetrating in $\mathbb{R}^+$ (resp. $\mathbb{R}^-$) when $\bar{\nu} < 0$ (resp. $\bar{\nu} > 0$). Indeed, for negative (resp. positive) mean growth rate, if the instantaneous growth rate experiences deep excursions in $\mathbb{R}^+$ (resp. in $\mathbb{R}^-$), rare events in the form of amplitude bursts (resp. intermittent quiet period) can occur. This necessary condition is fulfilled for $|\bar{\nu}/\sigma_\nu| \leq O(1)$. It corresponds to the four middle columns of Figure 4.15**(c)**, where heavy-tailed PDFs. and pronounced central peaks can be observed.

However, the condition $|\bar{\nu}/\sigma_\nu| \leq O(1)$ is not sufficient for intermittency to occur. In

fact, sporadic excursions of ν in $\mathbb{R}^+$ or $\mathbb{R}^-$ must last sufficiently long for the dynamic system to react to this change of stability, i.e. for having a system intermittently unstable (fat tailed PDF) or intermittently stable (marked central peak). Therefore, there is a second necessary condition for observing intermittency: the characteristic relaxation time of the system $1/\bar{\nu}$ must be shorter than the correlation time of the parametric stochastic forcing τ_χ. This condition is satisfied when $|\bar{\nu}\tau_\chi| \geq O(1)$, which corresponds to the two upper rows in 4.15(**c**). When $|\bar{\nu}\tau_\chi| \gg O(1)$, the system is subject to slow random fluctuations of the instantaneous linear growth rate ν, which corresponds to quasi-steady change of the bifurcation parameter. When $|\bar{\nu}\tau_\chi| = O(1)$, rare events can still occur but the intermittence is less marked. Finally, if $|\bar{\nu}\tau_\chi| \ll O(1)$, the fluctuations of the instantaneous growth rate exhibit a correlation that is smaller than the charateristic relaxation time of the oscillation amplitude, i.e. they are two fast to allow the system to adapt to them and the instantaneous attractor cannot be reached.

In summary, the rare events happen (PDFs with fat tails or marked central peak) when the correlation time of the fluctuations of instantaneous linear growth rate is of the order of, or longer than the inverse of the mean linear growth rate, and when the standard deviation of these fluctuations is larger than the mean linear growth rate.

4.5.3 Amplitude dynamics: Langevin and Fokker-Planck equations

In order to complement the analysis of carried out in subsection 4.5.2, the amplitude equation associated to the stochastic differential equations (4.17) is derived by performing deterministic and stochastic averaging [95, 176]. The derivation is based on the fact that the aeroacoustic system is weakly nonlinear, which implies that the limit cycle is quasi-sinusoidal, and on the fact that the mean linear growth rate satisfies $\bar{\nu} \ll \omega_0$, which means that the amplitude and phase drift of the oscillation slowly vary with respect to the acoustic period $T = 2\pi/\omega_0$. It is therefore convenient to investigate the system dynamics using the coordinate system (A, φ), with

$$\eta = A\cos(\omega_0 t + \varphi) \quad \text{and} \quad \dot{\eta} = -A\omega_0\sin(\omega_0 t + \varphi), \tag{4.18}$$

and $A = \sqrt{\eta^2 + (\dot{\eta}/\omega_0)^2}$ and $\varphi = -\arctan(\dot{\eta}/\omega_0\eta) - \omega_0 t$. Furthermore, we make the assumption that the multiplicative Ornstein-Ulhenbeck noise χ, which is governed by the Langevin equation (4.16), exhibits a correlation time τ_χ that is significantly longer than the acoustic period. In other words, when $\omega_0\tau_\chi/2\pi \gg 1$, χ can be considered as constant during one oscillation period and one can apply the averaging process described by e.g. Noiray [129]. For most of the cases considered in subsection 4.5.2, τ_χ is at least one order of magnitude longer than T (see coloured circles in Figure 4.15(**a**)) and this condition is well satisfied. The stochastic averaging procedure leads to a system of equations for the amplitude A, the phase drift φ and the parametric noise χ of the form

$$\dot{\boldsymbol{Y}} = \boldsymbol{F}(\boldsymbol{Y}) + \boldsymbol{B}(\boldsymbol{Y})\boldsymbol{N}. \tag{4.19}$$

In this equation, the dynamics of the system state-vector $\boldsymbol{Y} = (A, \varphi, \chi)^T$ is defined by a deterministic contribution $\boldsymbol{F}(\boldsymbol{Y})$ and by a stochastic forcing term $\boldsymbol{B}(\boldsymbol{Y})\boldsymbol{N}$, where $\boldsymbol{N} = (\zeta_A, \zeta_\varphi, \zeta_\chi)^T$ is a vector of independent white gaussian noises. The intensity of ζ_A and ζ_φ is $\Gamma_\xi / 2\omega_0^2$, and the one of ζ_χ is $\Gamma_\chi / \tau_\chi^2$. The deterministic components of this coupled system of Langevin equations are

$$F_A(\boldsymbol{Y}) = (\bar{\nu} + \chi)\, A - \frac{\kappa}{8} A^3 + \frac{\Gamma_\xi}{4\omega_0^2 A}, \quad F_\varphi(\boldsymbol{Y}) = 0, \quad F_\chi(\boldsymbol{Y}) = -\frac{\chi}{\tau_\chi}, \tag{4.20}$$

and the stochastic components are given by

$$\boldsymbol{B}(\boldsymbol{Y})\boldsymbol{N} = \begin{pmatrix} 1 & 0 & 0 \\ 0 & A^{-1} & 0 \\ 0 & 0 & 1 \end{pmatrix} \begin{pmatrix} \zeta_A \\ \zeta_\varphi \\ \zeta_\chi \end{pmatrix}. \tag{4.21}$$

One can notice that the equation for A does not depend on φ and one can therefore focus on the independent system of Langevin equations

$$\dot{A} = (\bar{\nu} + \chi)\, A - \frac{\kappa}{8} A^3 + \frac{\Gamma_\xi}{4\omega_0^2 A} + \zeta_A, \tag{4.22}$$

$$\dot{\chi} = -\frac{\chi}{\tau_\chi} + \zeta_\chi, \tag{4.23}$$

and write its corresponding two dimensional Fokker-Planck equation

$$\frac{\partial \mathcal{P}}{\partial t} = -\frac{\partial}{\partial A}(F_A \mathcal{P}) - \frac{\partial}{\partial \chi}(F_\chi \mathcal{P}) + \frac{\partial^2}{\partial A^2}\left(\frac{\Gamma_\xi \mathcal{P}}{4\omega_0^2}\right) + \frac{\partial^2}{\partial \chi^2}\left(\frac{\Gamma_\chi \mathcal{P}}{2\tau_\chi^2}\right), \tag{4.24}$$

which describes the time evolution of the joint PDF $\mathcal{P}(A, \chi; t)$. This Fokker-Planck equation is solved in the domain bounded by $A \in [0, 250]$ and $\chi \in [-200, 200]$ by using finite differences for the partial derivatives with respect to A and χ, and explicit Euler integration for the time derivative. A Dirichlet boundary condition $\mathcal{P}(A, \chi; t) = 0$ is imposed for $A = 0$, while the other boundaries assumes Neumann boundary with no flux. The initial conditions $\mathcal{P}(A, \chi; 0) = \mathcal{P}_{\text{init}}(A, \chi)$ is arbitrarily set for $\bar{\nu}\tau_\chi = 0.1$ to the theoretical joint PDF of the bivariate problem when the two random processes A and χ are assumed independent, i.e. when χ is removed from Eq. (4.22):

$$\mathcal{P}_{\text{init}}(A, \chi) \propto \exp\left(-\frac{4\omega_0}{\Gamma_\xi}\left[\frac{\bar{\nu} A^2}{2} - \frac{\kappa A^4}{32}\right]\right) \exp\left(-\frac{\chi^2}{\Gamma_\chi / \tau_\chi}\right). \tag{4.25}$$

The converged steady solutions of this Fokker-Planck for $\bar{\nu}\tau_\chi = 0.1$ and $\bar{\nu}\tau_\chi = 1$ are presented in Figures 4.16(i) and 4.16(j) respectively. Note that for $\bar{\nu}\tau_\chi = 1$, the initial condition is not defined by (4.25), but it is set as the converged solution of the case $\bar{\nu}\tau_\chi = 0.1$ in order to avoid numerical instabilities. Note also that these two cases corresponds to the same set of parameters as the one used to generate the PDFs presented in the second last column of Figure 4.15(c). In this figure, for the sake
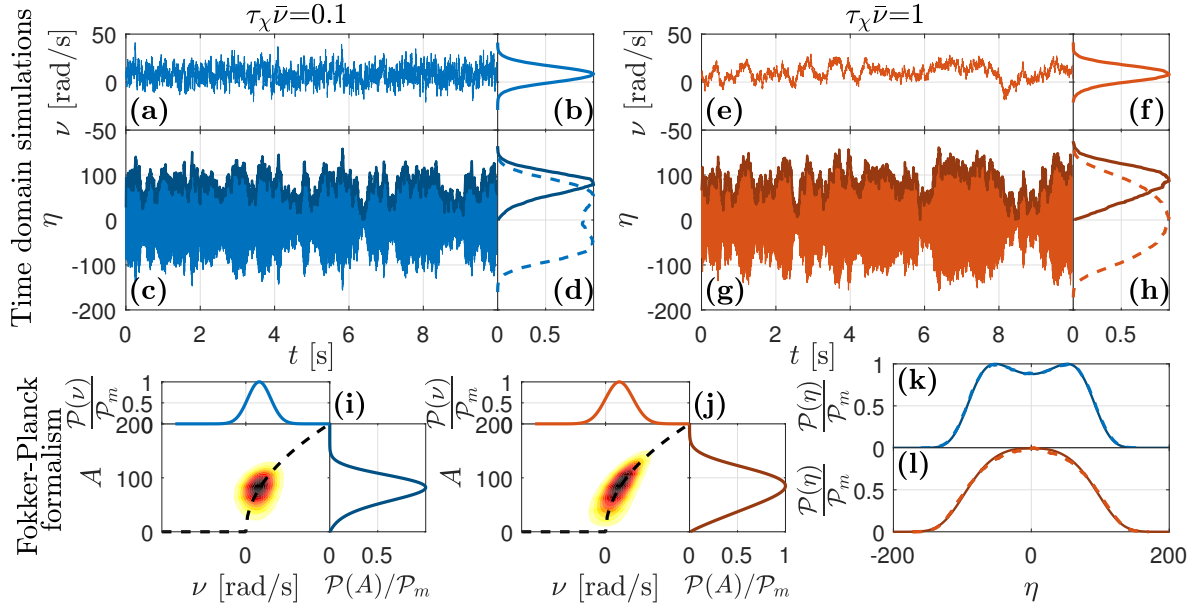
Figure 4.16: Time domain simulations of the Van der Pol oscillator (4.17) subject to additive and multiplicative stochastic forcing and stationary solutions of the Fokker-Planck equation (4.24) for $\tau_\chi \bar{\nu} = 0.1$ (**(a)**, **(b)**, **(c)**, **(d)**, **(i)** and **(k)**) and for $\tau_\chi \bar{\nu} = 1$ (**(e)**, **(f)**, **(g)**, **(h)**, **(j)** and **(l)**). **(a)** and **(e)**: Time traces of ν which is governed by Eq. (4.16). **(b)** and **(f)**: PDFs of ν computed from the time domain simulations of (4.16). **(c)** and **(g)**: Time traces of η and its envelope. **(d)** and **(h)**: PDFs of η and its envelope, which are computed from the time domain simulations of (4.17). **(i)** and **(j)**: stationary solutions $\mathcal{P}(A, \nu)$ of the Fokker-Planck equation (4.24) for $\tau_\chi \bar{\nu} = 0.1$ and for $\tau_\chi \bar{\nu} = 1$ respectively. The deterministic bifurcation diagram is superimposed as a dashed line, with $A = (8\nu/\kappa)^{1/2}$ for $\nu > 0$. The marginal PDFs $\mathcal{P}(A) = \int_{-\infty}^{\infty} \mathcal{P}(A, \nu) d\nu$ and $\mathcal{P}(\nu) = \int_0^\infty \mathcal{P}(A, \nu) dA$ are also shown as solid lines on the top and the side of the contour plot of $\mathcal{P}(A, \nu)$. **(k)** and **(l)**: Comparison of $\mathcal{P}(\eta)$ obtained from the time domain simulations of (4.16) and (4.17), and from the time domain simulations of (4.24), respectively shown as dashed and solid lines.

89

of clarity, we show $\mathcal{P}(A, \nu)$, which is identical to $\mathcal{P}(A, \chi)$ in the coordinate system $(A, \nu = \bar{\nu} + \chi)$.

From now on, we refer to stationary PDFs when the time variable t is not indicated as argument of $\mathcal{P}$. The marginal PDFs for A and ν are also presented on the side and on the top of the joint distribution in Figures 4.16(**i**) and 4.16(**j**). One can note that instead of computing $\int_0^\infty \mathcal{P}(A, \nu) dA$ to find $\mathcal{P}(\nu)$, this marginal distribution could be directly found analytically: it is given by the Gaussian solution of the Fokker-Planck equation associated to the univariate Ornstein-Uhlenbeck process (4.23), which is proportional to the second exponential term in Eq. (4.25). One can clearly see that, when the correlation time τ_χ of the parametric noise is increased from 12.5 ms to 125 ms, while the mean and the standard deviation of the growth rate are kept constant ($\bar{\nu} = \sigma_\nu = 8$ rad/s), the peak of the joint PDF contracts and adopts a more elongated shape that follows the bifurcation diagram of the deterministic system. This behaviour is due to an increased intermittency which is well captured by this Fokker-Planck formalism.

Moreover, these PDFs are compared to the ones deduced from time domain simulations of the stochastically forced Van der Pol oscillator governed by Eq. (4.17), and of its coloured multiplicative noise obeying Eq. (4.16). The simulated time traces of ν and η are presented in Figures 4.16(**a**), 4.16(**c**), 4.16(**e**) and 4.16(**g**) for $\bar{\nu}\tau_\chi = 0.1$ and $\bar{\nu}\tau_\chi = 1$. One can clearly see that the correlation time of the instantaneous growth rate is larger for the case of $\bar{\nu}\tau_\chi = 1$. From these time traces, the histograms of ν, η and its envelope are computed to get the PDFs shown in Figures 4.16(**b**), 4.16(**d**), 4.16(**f**) and 4.16(**h**). One can see that for $\bar{\nu}\tau_\chi = 1$, at $t \approx 8$ s, the instantaneous growth rate makes a sufficiently deep and sufficiently long excursion in $\mathbb{R}^-$ to induce a noticeable decrease of the oscillation amplitude in Figure 4.16(**g**). This is an example of sporadic quiet periods, which is typical of intermittently stable dynamics, and which leads to an increased probability density function $\mathcal{P}(A)$ at low amplitude compared to the case $\bar{\nu}\tau_\chi = 0.1$.

Finally, it is interesting to compare the PDFs of η obtained from the time domain simulations of the Van der Pol oscillator (4.17) and the ones deduced from the Fokker-Planck equations describing the slow-flow dynamics of this stochastically forced Van der Pol oscillator. To that end, one has to deduce $\mathcal{P}(\eta)$ from the numerical solution of the Fokker-Planck equation (4.24), which requires a few steps. First, one assumes that the joint PDF of the multivariate process (A, φ, χ) is separable and can be written $\mathcal{P}(A, \varphi, \chi) = \mathcal{P}(A, \chi)\mathcal{P}(\varphi)$ in order to deduce the univariate stationary PDF for φ.

By injecting this ansatz into the Fokker-Planck equation of the trivariate process, considering the stationary solution and the fact that $\mathcal{P}(A, \chi)$ satisfies Eq. (4.24), we can deduce that $d^2\mathcal{P}(\varphi)/d\varphi^2 = 0$, which implies that $\mathcal{P}(\varphi) = c_1\varphi + c_2$ with c_1 and c_2 the integration constants. Considering that $\mathcal{P}(\varphi)$ must be periodic, one can deduce that $c_1 = 0$, which means that φ is uniformly distributed between 0 and 2π. Second, we consider the projection of the oscillatory dynamics onto the slowly varying amplitude, phase and linear growth rate that is used to derive the above analytical expressions. With

the mapping $(A, \varphi) \to (\eta, \dot{\eta})$ given in (4.18), one can write that $\mathcal{P}(\eta, \dot{\eta}) \propto J^{-1}\mathcal{P}(A, \varphi)$, where the $J = A\omega_0$ is the absolute value of the determinant of the Jacobian matrix associated with this mapping. Then, considering that $\mathcal{P}(\varphi) = 1/2\pi$, one can write that $\mathcal{P}(A, \varphi) \propto \int_{-\infty}^{\infty} \mathcal{P}(A, \chi)d\chi$, and therefore, that $\mathcal{P}(\eta, \dot{\eta}) \propto A^{-1} \int_{-\infty}^{\infty} \mathcal{P}(A, \chi)d\chi$.

Finally, the univariate PDF for η can be obtained from the marginal PDF for A that is deduced from the numerical solution of (4.24) by using $\mathcal{P}(\eta) = \int_{-\infty}^{\infty} \mathcal{P}(\eta, \dot{\eta})d\dot{\eta}$. The PDFs obtained in that way for $\bar{\nu}\tau_\chi = 0.1$ and $\bar{\nu}\tau_\chi = 1$ are is shown in Figures 4.16(**k**) and 4.16(**l**) as solid lines. As expected, there is an excellent overlap between these PDFs and the ones from the histograms of the time domain simulations of (4.17) shown as dashed lines.

For the case shown in Figure 4.16(**l**), the two necessary conditions for intermittency presented in subsection 4.5.2 are fulfilled. Indeed, one has $|\bar{\nu}/\sigma_\nu| \leq O(1)$ and $|\bar{\nu}\tau_\chi| \geq O(1)$, which leads to a significant change of the shape of $\mathcal{P}(\eta)$ compared to the case where $|\bar{\nu}\tau_\chi| = 0.1$, and this change can be predicted using the Fokker-Planck description of the slow-flow dynamics.

4.6   Conclusions

This chapter deals with the classic problem of whistling of deep cavities subject to low-Mach turbulent grazing flow, which arises from the constructive interaction between the shear layer at the cavity opening and the acoustic modes of the cavity. It occurs for certain ranges of cavity depth and grazing flow velocity. Acoustic measurements and particle image velocimetry are performed to systematically characterise the instability of the present experimental setup.

Then, the specific acoustic admittance of the cavity (resp. the specific acoustic impedance of its opening) is measured for a range of depths (resp. bulk flow velocities) by using the multi-microphone method, and subsequently fitted using second order transfer functions. The latter are used to construct a model of two coupled oscillators that allows us to perform a linear stability analysis of the system, which is in very close agreement with the experimental measurements of the whistling conditions.

The specific impedance of the cavity opening subject to grazing flow is also measured for higher acoustic forcing amplitudes. From these measurements, it is possible to establish scaling laws for all the parameters of the model, which are non-dimensionalized using the grazing flow velocity, the cavity width and the cavity depth. With this information, the amplitude of the aeroacoustic limit cycle is first estimated by performing a describing function analysis, and then by using the amplitude and phase equations derived from the model of nonlinear oscillators with resistive and reactive coupling. These estimates are in good agreement with the experimental measurements.

It should be noted that a single set of model parameters allow to predict the bifurcation diagram for any combination of grazing flow velocity and cavity depth. Furthermore,

this deterministic analysis of the problem allows us i) to demonstrate that for such aeroacoustic instability problem, the root loci topology differs from the one of flow-induced vibration problems with frequency lock-in, and that the instability arises from the resistive and reactive coupling of the two linearly stable oscillators, and ii) to identify the nonlinearities at play in the system and to demonstrate that our system features Hopf bifurcations that are always supercritical.

In the last part of this chapter, we identify the origin of the intermittency observed in the vicinity of these supercritical Hopf bifurcations. We show that the system can be intermittently stable or intermittently unstable for certain combinations of grazing flow velocity and cavity depth, as a result of the parametric stochastic forcing induced by the turbulent fluctuations of the flow. We successfully reproduce the corresponding acoustic time traces and their probability density functions by incorporating an additive white noise and a multiplicative coloured noise into the model of coupled oscillators.

Then, considering the fact that in the vicinity of the Hopf bifurcation, the system of coupled nonlinear oscillators can be simplified to a randomly-forced Van der Pol oscillator, we identify two necessary conditions for intermittency in this type of system: the correlation time of the fluctuations of the linear growth rate must be of the order or longer than the inverse of the mean growth rate, and their standard deviation must be of the order or larger than the mean linear growth rate. This intermittency manifest itself by sporadic intervals of low amplitude oscillations, which lead to a marked central peak in the probability density function of the acoustic pressure, or by intermittent bursts of high amplitude, which lead to heavy tails. Lastly, we present a complementary analysis based on the Fokker-Planck equation for the slow-flow dynamics, which offers an alternative treatment of such problem of weakly nonlinear self-oscillator. As a final remark, it is worth mentioning that these findings are also relevant for the problem of thermoacoustic instabilities in turbulent combustors.

Chapter 5

General conclusion and outlook

Noise pollution is a critical issue for the well-being of human societies and ecosystems. Most of the noise disturbance stems from high-amplitude tonal noise, which can originate either in acoustic *resonance* or in an *instability*. The instability can occur when an acoustic system is coupled to a source term, under certain conditions allowing constructive feedback. The focus of this thesis is on thermoacoustic (where the source term is an unsteady flame) and aeroacoustic instabilities (where the source term is an unsteady shear layer).

This thesis uses the harmonic oscillator approximate solution in order to model the different blocks of the system. This coupled oscillator system modelling approach is used for highlighting the coupling between cavity and source term as the mechanism of instability (chapter 4, for an aeroacoustic instability), or for modelling the stabilization potential of additional acoustic cavities coupled to a system experiencing a thermoacoustic instability (chapters 2 and 3). This approach allows for the analysis of a variety of characteristics of the studied system (unstable range, bifurcation diagram, limit-cycle amplitude estimation, hysteresis and intermittency) without the need to model any flow physics in detail. The main contributions of the thesis and suggestions for future research are detailed below, in order of appearance in the thesis.

Quarter-Wave resonator modelling: the modelling of the deep cavity – shaped acoustic cavity introduced in section 2.2.1 is one of the novelty of this thesis: indeed, such acoustic cavities are usually represented using a cotangent function, whereas the approach introduced in this thesis allows the modelling of such cavities as a 2nd order transfer function or 2nd order differential equation. This modelling, verified against experiments, was proven to be accurate. It can also be applied for any mode in the cavity, not only the fundamental quarter-wave mode: this versatility was shown by using the model on the quarter-wave mode in chapter 2 and on the three-quarter-wave mode in chapter 4. Some improvements that could be made to the modelling of the damping term, since even with the addition of visco-thermal losses in the acoustic boundary layers, the model resistance does not match the experimental one at low purge flows

(Figure 2.5).

Exceptional point as best stabilization of an unstable acoustic mode by a cooled damper: The linear stability analysis and study of the coupled systems eigenvalues gave an analytical criteria for optimizing the damper cooling flow, in order to achieve best stabilization of a certain unstable acoustic mode. It turns out that the best stabilization occurs at the exceptional point, i.e. the set of parameters such that the 4th order system has 2 complex conjugate double eigenvalues. The ideal damping can easily be expressed as function of the frequency and growth rate of the instability, as well as the efficiency factor. This analysis can be performed for both Helmholtz and Quarter-Wave damper thanks to the modelling mentioned in the previous paragraph.

Maximization of acoustic absorption per unit area *versus* **Stabilization of an unstable mode in a volume**: There seems to be some confusion on the method to determine best damping (i.e. best purge flow) for an acoustic damper that will be added to a chamber featuring an unstable acoustic mode. Indeed, reflection coefficient measurements are often used as a mean of estimating the damper *performance*. This can be misleading, because the best performance of the damper is then determined when anechoic conditions are reached (i.e. impedance matching at the damper opening), which does not give any information on how the damper is going to perform when coupled to a chamber featuring an unstable acoustic mode. In Fig. 2.19 we clarified that the two "ideal" purge mass flows have nothing to do with each other: one of them depends on the porosity, i.e. the damper opening area over total surface area, while the other one depends on the efficiency factor, which depends on the damper-chamber volume ratio and on the damper location with respect to the acoustic mode shape.

Helmholtz damper nonlinearity: the effect of the Helmholtz damper nonlinearity due to reverse flow on the bifurcation diagram of the coupled system has been analytically derived and experimentally proven in chapter 3. The nonlinearity itself had already been highlighted in the literature, by measuring the damper acoustic response under high amplitude, but its effect when the damper is coupled to a chamber with an unstable acoustic mode was not yet investigated. The work done in this thesis highlighted the occurrence of hysteretic behaviour, which can be potentially dangerous, with the system suddenly jumping to a very high oscillation amplitude. One limitation of this work is that it highlights the effect of the nonlinearity only, whereas in the real occurrence of reverse flow in the case of thermouacoustic instability stabilization, some hot gas from the combustion chamber would enter the damper neck and change its density. The effects of this hot gas ingestion are still not well understood and should be further studied.

Shear layer describing function: In chapter 4, the occurence of aeroacoustic instability has been predicted as function of deep cavity length and mean flow velocity based on shear layer acoustic response. The deep cavity using the Quarter-Wave resonator modelling mentioned above.The frequency- and amplitude-dependent shear layer impedance was measured and fitted with a 2nd order transfer function in order to ac-

curately reproduce the system stability and limit cycle amplitudes. Future work could involve the extension of the model to multiple modes of both the deep cavity and the shear layer, in order to cover a bigger range of cavity lengths and mean flow velocities in the channel. Another possible line of future work would be to develop a framework for determining the acoustic response based on canonical experiments and various system parameters, in order to make this applicable in cases where direct measurements of the acoustic response is not possible.

Intermittency: The use of a well-designed coloured noise with the model described in the previous paragraph allowed the reproduction of the experimentally-observed intermittency on the studied aeroacoustic instability. The effect of the coloured noise was then demonstrated on a simpler model (the Van der Pol oscillator) and this allowed for the derivation of simple criteria for the occurrence of intermittency under multiplicative noise excitation. Indeed, for a coloured noise applied to the system's growth rate to induce some intermittency, the correlation time of the noise needs to be at least of the order of magnitude of the inverse of the mean growth rate (i.e. the oscillation amplitude correlation time), and the variance of the noise needs to be at least of the order of magnitude of the mean growth rate.

Frequency ramp rate for sweep measurements: The appendix offers a simple criterion for determining what is the critical ramp rate that one must not exceed, in order to measure the resonance frequency and corresponding damping of a simple damped harmonic oscillator using sweep measurements. This critical ramp rate differs from the one already highlighted in the literature for measuring the amplitude of the quasi-steady response accurately, which is significantly lower (i.e. significantly slower sweeps are needed). By extension, this criterion can be used for any linearly stable system exhibiting sufficiently spaced separate modes.

Over the course of this thesis, the system of coupled oscillators model, although representing a projected approximation of the system, has proven very useful to analyse a variety of features of thermo- and aeroacoustic instabilities, from a qualitative and quantitative point of view. In order to accurately and quantitatively model the system, the current approach is semi-empirical and relies on experiments to be performed for determining crucial parameters. This limitation can be bypassed by using parameters from canonical measurements that flourish in the literature, and still allows for the accurate representation of the system dynamics, at least from a qualitative point of view.

Appendix: critical frequency ramp rate for sweep measurements

This appendix is based on the comment *Comment on "Slow passage through resonance"* by Claire Bourquard and Nicolas Noiray published in Physical Review E **100**, 047001 (2019).

In this appendix, the slow passage through resonance for a damped harmonic oscillator is reviewed, by looking at previous studies investigating this problem. The difference between the critical frequency ramp rate for resonance amplitude measurement and the critical frequency ramp rate for resonance frequency and damping measurement is also underlined.

As a first introductory comment, it is important to mention that i) this problem of "slow passage through resonance", for which the frequency of the harmonic forcing is ramped, is restricted to stable linear oscillators, i.e. with α being a real positive constant, and that ii) this problem differs from the "slow passage through Hopf bifurcations", for which one ramps at a finite rate the damping coefficient from a positive to a negative value (e.g. [3, 10, 15, 16]).

The first report on the dynamics of a mechanical oscillator excited by a force whose frequency depends linearly on time, and the first attempt at modelling the discrepancy between stationary and non-stationary amplitude response dates back to the 30's [100]. In a subsequent study, Hok [71] derived partial analytical solutions for the amplitude of a general oscillator during sweep excitations using Fresnel functions. A few years later Fearn and Millsaps [56] derived a complete analytical expression for the amplitude in the undamped harmonic oscillator. A NASA report from Reed et. al. [146] quantifies experimentally the discrepancy in amplitude and frequency at which resonance occurs as function of the frequency ramp rate. Kevorkian [88] later used the method of multiple scales to derive asymptotic expansions close to and at a distance from resonance, for a similar problem, where the excitation frequency of the harmonic forcing is fixed while the resonance frequency of the system varies with time. As was underlined by Hok [71], this problem is equivalent to the problem considered here. A more recent study on a

similar problem was conducted by Kaczmarczyk [81]. Collinge and Ockendon [30] also used the method of multiple scales for deriving analytical approximations, additionally using it to underline a relevant time scale for the choice of the frequency ramp rate. An analytical study by Sung and Stevens [179] also discussed a criterion for the maximum frequency ramp rate allowed for accurate resonance frequency measurements.

A number of empirical formulae were derived over the years to approximate the discrepancy between resonance amplitude and frequency obtained by harmonic forcing or frequency chirp, which are summarized in the paper by Markert and Seidler [110]. A study by Torvik [185], also identified the threshold frequency ramp rate for which one achieves the correct resonating amplitude, claiming the same threshold holds for damping prediction. Some articles also extend the study to lightly nonlinear oscillators [30, 53, 77, 185].

Usually, to correctly capture the resonance frequency and quality factor of the damped harmonic oscillator from sweep measurements, one has to use a frequency ramp rate which is slow enough so that the envelope of the time trace of the response does not exhibit modulation. In a previous study by White [190], a "vector technique" and a fit of the frequency response in the complex plane (equivalent to the transfer function fit done in the present appendix) allows the resonance frequency and damping measurements from "rapid frequency sweeps", although the actual chirp rate was not specified. This suggests that higher frequency ramp rates can be used for the characterization of the resonant mode (frequency and damping), as will be shown subsequently.

Several studies have been specifically undertaken to establish analytical exact and approximate solutions to the problem of harmonic oscillators forced with chirps, in the undamped [56, 71, 138] and the damped case [30, 81, 88]. The following part of this appendix aims to provide an exhaustive picture of the problem based on numerical solutions of the following ordinary differential equation:

$$\frac{d^2x}{d\tau^2} + 2\alpha_\mathrm{n}\frac{dx}{d\tau} + \omega_\mathrm{n}^2 x = F\sin\left(\left[\omega_\mathrm{i} + \frac{\epsilon_r}{2}\tau\right]\tau\right) \tag{A.1}$$

With α_n the damping rate, ω_n the undamped natural angular frequency, F the amplitude of the forcing, ω_i the initial frequency of the chirp and ϵ_r the frequency ramp rate. Using the nondimensional time $t = \omega_\mathrm{n}\tau$, this equation becomes:

$$\ddot{x} + \alpha\dot{x} + x = \sin(\omega_f t) \qquad \text{with} \quad \omega_f = \omega_0 + \frac{\epsilon t}{2}, \tag{A.2}$$

and with $\alpha = 2\alpha_\mathrm{n}/\omega_\mathrm{n}$, $\omega_0 = \omega_\mathrm{i}/\omega_\mathrm{n}$ and $\epsilon = \epsilon_r/\omega_\mathrm{n}^2$. Note that we also assume $\dfrac{F}{\omega_\mathrm{n}^2} = 1$. The instantataneous forcing frequency then reads:

$$\omega_\mathrm{inst}(t) = \frac{d}{dt}\left[\left(\omega_0 + \frac{\epsilon t}{2}\right)t\right] = \omega_0 + \epsilon t. \tag{A.3}$$

For steady harmonic excitation at angular frequency ω, the response amplitude is:

$$A(\omega) = \frac{1}{\sqrt{\omega^2 \alpha^2 + (1 - \omega^2)^2}}. \tag{A.4}$$

For the chirp excitation of Eq. (A.2), with instantaneous frequency given by Eq. (A.3), the responses for three different values of ϵ can be seen in Figure A1(b): for a very slow frequency ramp rate (green), the shape of the envelope of the response approaches the response amplitude. For increasing frequency ramp rates (blue and red), the resonance is delayed and reaches a lower maximum amplitude. In these cases, although resonance occurs at an excitation frequency higher than the natural frequency, the frequency response is still dominated by the natural frequency. This explains the low-frequency oscillation postresonance, which assimilates to a beating between oscillations at the system's natural frequency and oscillations at the excitation frequency, as was underlined by Markert and Seidler in [110].

The effect of frequency ramp rate upon the instantaneous frequency at which maximum response occurs is displayed in Figure A1(c) for different oscillator damping: the quasi-steady chirp asymptotes exhibit instantaneous frequencies at maximum response that are lower than 1, which corresponds to the expected resonance frequency for harmonic forcing $\omega = \sqrt{1 - \alpha^2/2}$. The later frequency is different from the frequency of the pseudo-harmonic free damped oscillations $\omega = \sqrt{1 - \alpha^2/4}$. Figure A1(c) also underlines the delay in resonance for fast chirps, where the maximum amplitude is reached at a higher instantaneous frequency than the resonance frequency. This effect is accentuated when the damping α decreases. The effect of frequency ramp rate upon the maximum reached amplitude for different damping coefficients is presented in Figure A1(d) (similar to Figure 4a in [138] with a modified x-axis). One can see that for increasing oscillator damping, the critical chirp rate, above which the steady-state resonance amplitude is not attained any more, increases. This critical ramp rate is $\epsilon_A \approx \alpha^2/4$, which is consistent with [30, 179, 185].

If one is interested in the actual oscillation amplitude (during rampup of an engine to nominal condition for example [100]), then this criterion holds and one indeed needs very slow frequency ramp rates. However, for identifying the natural frequency ω_n and the damping α of a linear oscillator, one should not look at the transient amplitude response, but at the frequency content of the response to the linear chirp, by computing from data the transfer function:

$$\mathcal{H}(\omega) = \frac{S_{xy}(\omega)}{S_{yy}(\omega)}, \tag{A.5}$$

where S_{xy} is the cross-spectral density of the response $x(t)$ and of the chirp excitation $y(t) = \sin[\phi(t)] = \sin[(\omega_0 + \epsilon t/2)t]$, and S_{yy} is the power spectral density of $y(t)$. The transfer functions corresponding to the three examples of Figure A1b are displayed in Figure A1(e) , where all three are almost perfectly superimposed onto the transfer

function for steady harmonic excitation. In order to obtain the resonance frequency and damping of the oscillator, one can then simply fit a second order transfer function to this data. The effect of frequency ramp rate and system damping on the identified damping α_{fit} is shown in Figure A1($\mathbf{f}$). One can see that the critical chirp rate for this measure to be accurate is higher than the critical ramp rate needed to attain the maximum response amplitude. The critical frequency ramp rate for an accurate damping measurement is $\epsilon_\alpha \approx \alpha/10$. Since the damping α is by definition not known when one needs to choose the damping rate, this formula can still help by using an estimation of α.
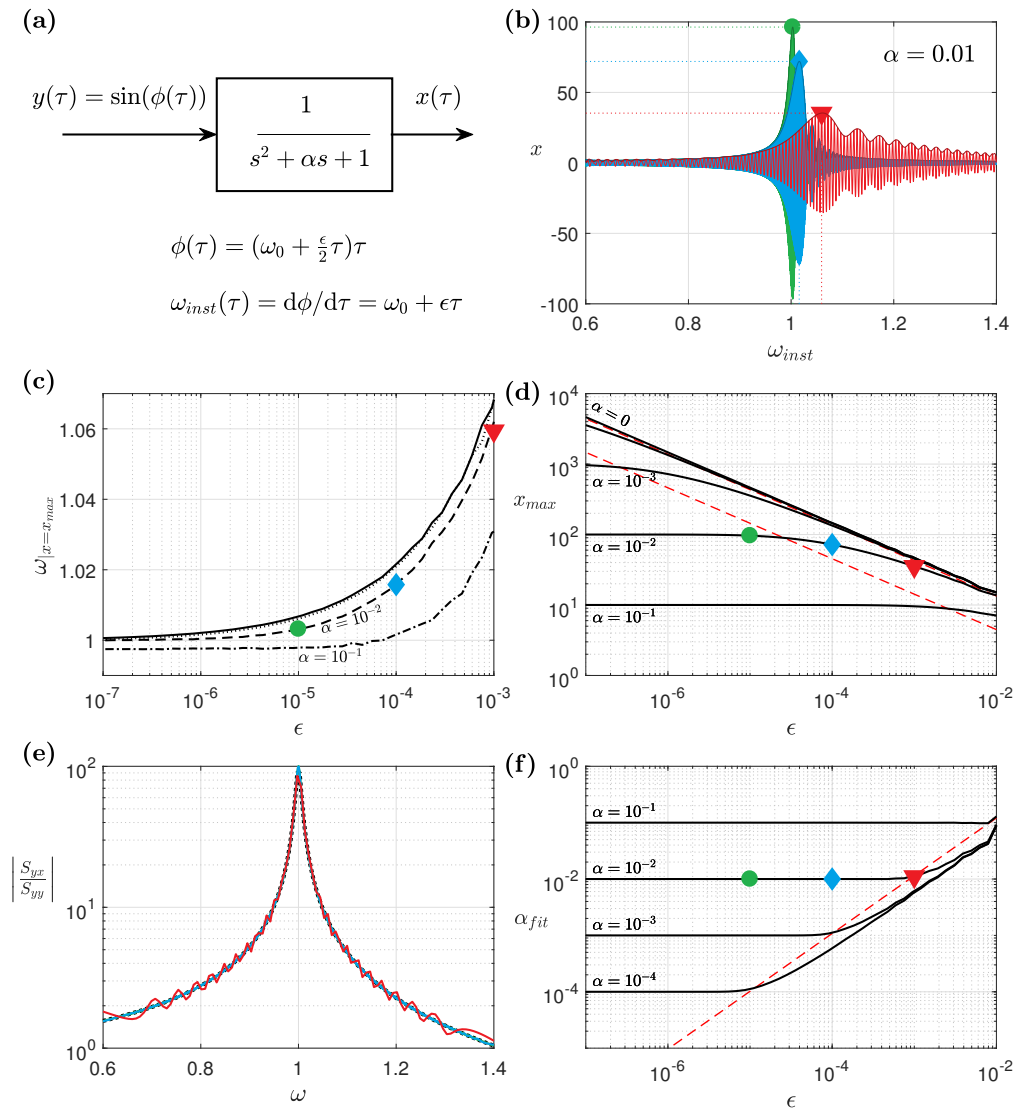
Figure A1: **(a)** Transfer function of the studied system with s the Laplace variable **(b)** Time traces of $x(t)$ as function of instantaneous angular frequency ω_{inst} for $\alpha = 10^{-2}$ and $\epsilon = 10^{-5}$ (green), 10^{-4} (blue), 10^{-3} (red) **(c)** Influence of damping α and frequency ramp rate ϵ on the instantaneous frequency at which the maximum amplitude is attained (black lines). Superimposed markers correspond to the time traces on top. **(d)** Influence of damping α and frequency ramp rate ϵ on the maximum amplitude reached by the oscillator (black lines). Superimposed markers correspond to the time traces on top. Red dashed line: limit of the maximum ϵ to be used for staying within 10% error on the maximum amplitude, given by $\epsilon_A = \alpha^2/4$. **(e)** Steady-state transfer function (blacked dashed) line, with almost perfectly superimposed transfer functions from the green, blue and red sweep signals on top. **(f)** Influence of damping α and frequency ramp rate ϵ on the damping α_{fit} obtained from a fit on the transfer function (black lines). Superimposed markers correspond to the time traces on top. Red dashed line: limit of the maximum ϵ to be used for staying within 10% error on α_{fit}, given by $\epsilon_\alpha = \alpha/10$.

The difference in these critical ramp rate is quite explicit when one looks closer at the red curves in subfigures A1(**d**) and A1(**f**) : considering the case of $\epsilon = 10^{-3}$, one has a maximum amplitude and corresponding instantaneous frequency that significantly differ from the corresponding steady harmonic forcing values. In contrast, the frequency response is very similar in terms of peak frequency, amplitude and width.
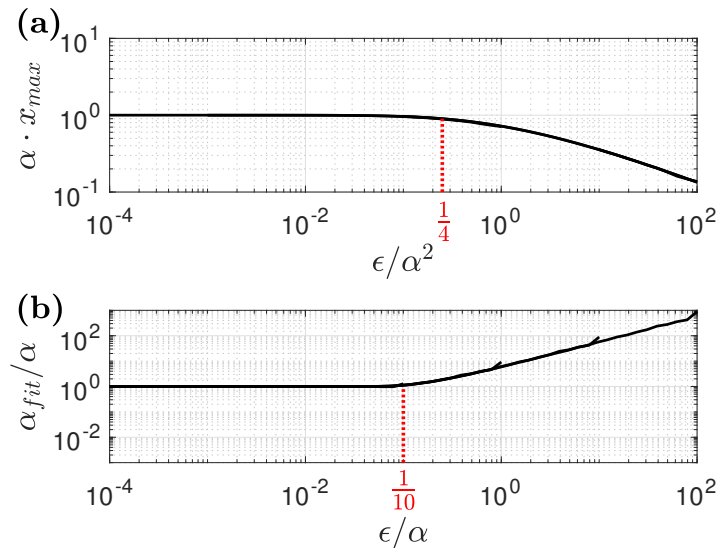

Figure A2: (**a**) Scaled $\alpha \cdot x_{max}$ as function of ϵ/α^2 (**b**) Scaled $\alpha_{\text{fit}}/\alpha$ as function of ϵ/α. In both cases, the curves of Figure A1 (**d**) and A1 (**f**) respectively collapse and the critical ramp rates can be easily estimated.

These results are summarized in Figure A2(**a**) and A2(**b**) where the axis have been rescaled such that the curves of A1(**d**) and A1(**f**) collapse and the critical linear chirp rates ϵ_{a} and ϵ_{d} become evident. These thresholds hold for linear damped harmonic oscillators excited by linear chirps in absence of significant random additive or multiplicative forcing. Regarding the later point and the influence of stochastic additive forcing, one can, for instance, refer to the early investigation of Kandianis [82].

List of Publications

First author journal publications

1. C. Bourquard, N. Noiray, "Stability and limit cycles of a nonlinear damper acting on a linearly unstable thermoacoustic mode", *Journal of Engineering for Gas Turbines and Power*, 141(5), 051012, (2019).

2. C. Bourquard, N. Noiray, "Stabilization of acoustic modes using Helmholtz and Quarter-Wave resonators tuned at exceptional points", *Journal of Sound and Vibration*, 445, 288-307, (2019).

3. C. Bourquard, N. Noiray, "Comment on *Slow passage through resonance*", *Physical Review E*, 100(4), 047001, (2019).

4. C. Bourquard, A. Faure-Beaulieu, N. Noiray, "Whistling of deep cavities subject to turbulent grazing flow: intermittently unstable aeroacoustic feedback", submitted to *Journal of Fluid Mechanics*, (2020).

Other journal publications

1. O. Schulz, U. Doll, D. Ebi, J. Droujko, C. Bourquard, N. Noiray, "Thermoacoustic instability in a sequential combustor: large eddy simulation and experiments", *Proceedings of the Combustion Institute*, 37(4), 5325-5332, (2019).

2. Y. Xiong, O. Schulz, C. Bourquard, M. Weilenmann, N. Noiray, "Plasma enhanced auto-ignition in a sequential combustor", *Proceedings of the Combustion Institute*, 37(4), 5587-5594, (2019).

3. E. Boujo, C. Bourquard, Y. Xiong, N. Noiray, "Processing time-series of randomly forced self-oscillators: The example of beer bottle whistling". *Journal of Sound and Vibration*, 464, 114981, (2020).

Curriculum Vitae

Personal details

Name	Claire Bourquard
Nationality	French
Birth	01/01/1991 in Mulhouse (France)

Education

2015-2020	Doctoral student - ETH Zürich, Mechanical and Process Engineering Department (D-MAVT), Institute of Energy Technology, Combustion and Acoustics for Power & Propulsion Systems (CAPS) Laboratory
2010-2015	Diplôme d'Ingénieur SUPAERO in Aerospace engineering - Institut Supérieur de l'Aéronautique et de l'Espace (ISAE), Toulouse (France)
2014-2015	Master Thesis - Alstom Power, Gas Turbine Research Burner Department Baden (Switzerland)
2012-2014	Exchange student in the Mechanical Engineering Masters Technische Universität Berlin (Germany)
2008-2010	Two-year program for preparing competitive entry exam to top French Engineering Schools, Lycée Kléber, Strasbourg (France)

Bibliography

[1] ACHILLEOS, V., THEOCHARIS, G., RICHOUX, O., AND PAGNEUX, V. Non-Hermitian acoustic metamaterials: Role of exceptional points in sound absorption. *Phys. Rev. B 95*, 14 (2017), 144303. (Cited on page 14.)

[2] ACKER, T., AND MITCHELL, C. Combustion zone–acoustic cavity interactions in rocket combustors. *J. Propuls. Power 10*, 2 (1994), 235–243. (Cited on page 12.)

[3] BAER, S., ERNEUX, T., AND RINZEL, J. The slow passage through a Hopf bifurcation: delay, memory effects, and resonance. *SIAM J. Appl. Math. 49*, 1 (1989), 55–71. (Cited on page 97.)

[4] BALACHANDRAN, R., AYOOLA, B., KAMINSKI, C., DOWLING, A., AND MASTORAKOS, E. Experimental investigation of the nonlinear response of turbulent premixed flames to imposed inlet velocity oscillations. *Combust. Flame 143*, 1-2 (2005), 37–55. (Cited on page 7.)

[5] BALANOV, A., JANSON, N., POSTNOV, D., AND SOSNOVTSEVA, O. *Synchronization: from simple to complex.* Springer, 2009. (Cited on pages 48 and 79.)

[6] BASLEY, J., PASTUR, L. R., LUSSEYRAN, F., SORIA, J., AND DELPRAT, N. On the modulating effect of three-dimensional instabilities in open cavity flows. *J. Fluid Mech. 759* (2014), 546–578. (Cited on page 83.)

[7] BELLUCCI, V. *Modeling and control of gas turbine thermoacoustic pulsations.* PhD thesis, TU Berlin, 2009. (Cited on page 39.)

[8] BELLUCCI, V., FLOHR, P., PASCHEREIT, C., AND MAGNI, F. On the Use of Helmholtz Resonators for Damping Acoustic Pulsations in Industrial Gas Turbines. *J. Eng. Gas Turbines Power 126*, 2 (2004), 271. (Cited on pages 2, 4, 8, 9, 12, 15, 44, 48, and 53.)

[9] BERGLUND, B., HASSMEN, P., AND JOB, R. Sources and effects of low-frequency noise. *J. Acoust. Soc. Am. 99*, 5 (1996), 2985–3002. (Cited on page 1.)

[10] BERGLUND, N. Control of dynamic Hopf bifurcations. *Nonlinearity 13*, 1 (2000), 225. (Cited on page 97.)

[11] Bilanin, A., and Covert, E. Estimation of possible excitation frequencies for shallow rectangular cavities. *AIAA Journal 11*, 3 (1973), 347–351. (Cited on page 3.)

[12] Björk, E. Laboratory annoyance and skin conductance responses to some natural sounds. *J. Sound Vib. 109*, 2 (1986), 339–345. (Cited on page 1.)

[13] Bonciolini, G., Boujo, E., and Noiray, N. Output-only parameter identification of a colored-noise-driven Van-der-Pol oscillator: Thermoacoustic instabilities as an example. *Phys. Rev. E 95*, 6 (2017), 062217. (Cited on page 8.)

[14] Bonciolini, G., Ebi, D., Boujo, E., and Noiray, N. Experiments and modelling of rate-dependent transition delay in a stochastic subcritical bifurcation. *R. Soc. Open Sci. 5*, 3 (2018), 172078. (Cited on pages 7, 8, 64, and 83.)

[15] Bonciolini, G., Ebi, D., Doll, U., Weilenmann, M., and Noiray, N. Effect of wall thermal inertia upon transient thermoacoustic dynamics of a swirl-stabilized flame. *Proc. Combust. Inst. 37*, 4 (2019), 5351–5358. (Cited on page 97.)

[16] Bonciolini, G., and Noiray, N. Bifurcation dodge: avoidance of a thermoacoustic instability under transient operation. *Nonlinear Dyn. 96*, 1 (2019), 703–716. (Cited on page 97.)

[17] Bothien, M., Noiray, N., and Schuermans, B. A novel damping device for broadband attenuation of low-frequency combustion pulsations in gas turbines. *J. Eng. Gas Turbines Power 136*, 4 (2014), 041504. (Cited on pages 2, 12, and 44.)

[18] Bothien, M., Penelli, D., Zajadatz, M., and Döbbeling, K. On key features of the AEV burner engine implementation for operational flexibility. In *Proc. ASME Turbo Expo 2013* (2013), p. V01BT04A051. (Cited on page 12.)

[19] Bothien, M., and Wassmer, D. Impact of density discontinuities on the resonance frequency of helmholtz resonators. *AIAA Journal 53*, 4 (2015), 877–887. (Cited on pages 13 and 44.)

[20] Boujo, E., Bauerheim, M., and Noiray, N. Saturation of a turbulent mixing layer over a cavity: response to harmonic forcing around mean flows. *J. Fluid Mech. 853* (2018), 386–418. (Cited on pages 63, 68, 70, and 75.)

[21] Boujo, E., Bourquard, C., Xiong, Y., and Noiray, N. Processing time-series of randomly forced self-oscillators: The example of beer bottle whistling. *J. Sound Vib. 464* (2020), 114981. (Cited on pages 3, 6, 64, and 71.)

[22] Boujo, E., and Noiray, N. Robust identification of harmonic oscillator parameters using the adjoint Fokker–Planck equation. *Proc. R. Soc. A 473* (2017), 20160894. (Cited on page 82.)

[23] Brandstetter, M., Liertzer, M., Deutsch, C., Klang, P., Schöberl, J., Türeci, H. E., Strasser, G., Unterrainer, K., and Rotter, S.

Reversing the pump dependence of a laser at an exceptional point. *Nat. Commun. 5*, May (2014), 4034. (Cited on page 14.)

[24] BRUGGEMAN, J., HIRSCHBERG, A., DONGEN, M. V., WIJNANDS, A., AND GORTER, J. Self-sustained aero-acoustic pulsations in gas transport systems: experimental study of the influence of closed side branches. *J. Sound Vib. 150*, 3 (1991), 371–393. (Cited on page 63.)

[25] BURAK, M., BILLSON, M., ERIKSSON, L.-E., AND BARALON, S. Validation of a time-and frequency-domain grazing flow acoustic liner model. *AIAA Journal 47*, 8 (2009), 1841–1848. (Cited on page 12.)

[26] BURGIO, L., SCILLEY, K., HARDIN, J., HSU, C., AND YANCEY, J. Environmental "white noise": An intervention for verbally agitated nursing home residents. *J. Gerontol. B Psychol. Sci. Soc. Sci. 51*, 6 (1996), P364–P373. (Cited on page 1.)

[27] CAMPA, G., AND CAMPOREALE, S. Influence of nonlinear effects on the limit cycle in a combustion chamber equipped with Helmholtz resonator. In *ASME Turbo Expo* (2014). (Cited on page 44.)

[28] CÁRDENAS-MIRANDA, A., AND POLIFKE, W. Combustion stability analysis of rocket engines with resonators based on Nyquist plots. *J. Propuls. Power 30*, 4 (2014), 962–977. (Cited on page 12.)

[29] CLAVIN, P., KIM, J., AND WILLIAMS, F. Turbulence-induced noise effects on high-frequency combustion instabilities. *Combust. Sci. Technol. 96*, 1-3 (1994), 61–84. (Cited on pages 8 and 64.)

[30] COLLINGE, I., AND OCKENDON, J. Transition through resonance of a Duffing oscillator. *SIAM J. Appl. Math. 37*, 2 (1979), 350–357. (Cited on pages 98 and 99.)

[31] COMMISSION, E. *What are the health costs of environmental pollution?*, vol. 21 of *Science for Environment Policy*. Publications Office of the European Union, 2018. (Cited on page 1.)

[32] ĆOSIĆ, B., REICHEL, T., AND PASCHEREIT, C. Acoustic response of a Helmholtz resonator exposed to hot-gas penetration and high amplitude oscillations. *J. Eng. Gas Turbines Power 134*, 10 (2012), 101503. (Cited on pages 13 and 44.)

[33] ĆOSIĆ, B., WASSMER, D., TERHAAR, S., AND PASCHEREIT, C. Acoustic response of Helmholtz dampers in the presence of hot grazing flow. *J. Sound Vib. 335* (2015), 1–18. (Cited on page 44.)

[34] COSSALTER, V., DORIA, A., AND GIUSTO, F. Control of acoustic vibrations inside refrigerator compressors by means of resonators. *Int. Compress. Eng. Conf. Paper No. 1036* (1994). (Cited on page 12.)

[35] CROCCO, L. Theoretical studies on liquid-propellant rocket instability. *Symp. (Int.) Combust. 10*, 1 (1965), 1101–1128. (Cited on page 5.)

[36] CROCCO, L. Research on combustion instability in liquid propellant rockets. *Symp. Combust. 12*, 1 (1969), 85–99. (Cited on page 12.)

[37] CULICK, F. Unsteady motions in combustion chambers for propulsion systems. Tech. Rep. AG-AVT-039, RTO AGARDograph, 2006. (Cited on page 41.)

[38] CUMMINGS, A. Effects of a resonator array on the sound field in a cavity. *J. Sound Vib. 154*, 1 (1992), 25–44. (Cited on page 39.)

[39] DAI, X. Flow–acoustic resonance in a cavity covered by a perforated plate. *J. Fluid Mech. 884* (2020), A4. (Cited on page 62.)

[40] DAI, X., AND AURÉGAN, Y. A cavity-by-cavity description of the aeroacoustic instability over a liner with a grazing flow. *J. Fluid Mech. 852* (2018), 126–145. (Cited on page 62.)

[41] DEBUT, V., ANTUNES, J., AND MOREIRA, M. Flow-acoustic interaction in corrugated pipes: Time-domain simulation of experimental phenomena. In *9th Int. Conf. Flow-Induced Vibr.* (2008). (Cited on page 6.)

[42] DEQUAND, S., HULSHOFF, S., AND HIRSCHBERG, A. Self-sustained oscillations in a closed side branch system. *J. Sound Vib. 265*, 2 (2003), 359–386. (Cited on pages 3, 63, and 70.)

[43] DING, K., MA, G., XIAO, M., ZHANG, Z., AND CHAN, C. Emergence, coalescence, and topological properties of multiple exceptional points and their experimental realization. *Phys. Rev. X 6* (2016), 021007. (Cited on page 14.)

[44] DOLCI, D., AND CARMO, B. Bifurcation analysis of the primary instability in the flow around a flexibly mounted circular cylinder. *J. Fluid Mech. 880* (2019). (Cited on page 74.)

[45] DORIA, A. Control of acoustic vibrations of an enclosure by means of multiple resonators. *J. Sound Vib. 181*, 4 (1995), 673–685. (Cited on page 39.)

[46] DUCRUIX, S., SCHULLER, T., DUROX, D., AND CANDEL, S. Combustion dynamics and instabilities: Elementary coupling and driving mechanisms. *J. Propul. Power 19*, 5 (2003), 722–734. (Cited on pages 2 and 5.)

[47] DUPÈRE, I., AND DOWLING, A. The use of Helmholtz resonators in a practical combustor. *J. Eng. Gas Turbines Power 127*, 2 (2005), 268–275. (Cited on pages 2, 12, 13, and 44.)

[48] DUROX, D., SCHULLER, T., NOIRAY, N., AND CANDEL, S. Experimental analysis of nonlinear flame transfer functions for different flame geometries. *Proc. Combust. Inst. 32*, 1 (2009), 1391–1398. (Cited on page 7.)

[49] EAST, L. Aerodynamically induced resonance in rectangular cavities. *J. Sound Vib. 3*, 3 (1966), 277–287. (Cited on page 3.)

[50] ELDER, S. Self-excited depth-mode resonance for a wall-mounted cavity in turbulent flow. *J. Acoust. Soc. Am. 64*, 3 (1978), 877–890. (Cited on pages 6 and 62.)

[51] EMMERT, T., BOMBERG, S., AND POLIFKE, W. Intrinsic thermoacoustic instability of premixed flames. *Combust. Flame 162*, 1 (2015), 75–85. (Cited on page 5.)

[52] ESTÈVE, S., AND JOHNSON, M. Reduction of sound transmission into a circular cylindrical shell using distributed vibration absorbers and Helmholtz resonators. *J. Acoust. Soc. Am. 112*, 6 (2002), 2840–2848. (Cited on page 12.)

[53] EVAN-IWANOWSKI, R. *Resonance oscillations in mechanical systems.* North-Holland, 1976. (Cited on page 98.)

[54] FABRE, B., GILBERT, J., HIRSCHBERG, A., AND PELORSON, X. Aeroacoustics of musical instruments. *Annu. Rev. Fluid Mech. 44* (2011), 1–25. (Cited on page 62.)

[55] FAHY, F., AND SCHOFIELD, C. A note on the interaction between a Helmholtz resonator and an acoustic mode of an enclosure. *J. Sound Vib. 72*, 3 (1980), 365–378. (Cited on page 39.)

[56] FEARN, R., AND MILLSAPS, K. Constant acceleration of an undamped simple vibrator through resonance. *Aeronaut. J. 71*, 680 (1967), 567–569. (Cited on pages 97 and 98.)

[57] FLEIFIL, M., ANNASWAMY, A., GHONEIM, Z., AND GHONIEM, A. Response of a laminar premixed flame to flow oscillations: A kinematic model and thermoacoustic instability results. *Combust. Flame 106*, 4 (1996), 487–510. (Cited on page 5.)

[58] FÖRNER, K., CÁRDENAS-MIRANDA, A., AND POLIFKE, W. Mapping the influence of acoustic resonators on rocket engine combustion stability. *J. Propul. Power* (2015). (Cited on page 44.)

[59] FÖRNER, K., TOURNADRE, J., POLIFKE, W., AND MARTÍNEZ-LERA, P. Characterization of the nonlinear response of a Helmholtz resonator. *SFB/TRR40 Annu. Rep. 2015* (2015). (Cited on page 44.)

[60] GAO, T., ESTRECHO, E., BLIOKH, K. Y., LIEW, T. C., FRASER, M. D., BRODBECK, S., KAMP, M., SCHNEIDER, C., HÖFLING, S., YAMAMOTO, Y., NORI, F., KIVSHAR, Y. S., TRUSCOTT, A. G., DALL, R. G., AND OSTROVSKAYA, E. A. Observation of non-Hermitian degeneracies in a chaotic exciton-polariton billiard. *Nature 526*, 7574 (2015), 554–558. (Cited on page 14.)

[61] GARRISON, G., AND LEWIS, G. The role of acoustic absorbers in preventing combustion instability. *7th Propuls. Jt. Spec. Conf.* (1971). (Cited on page 12.)

[62] GIKADI, J., FÖLLER, S., AND SATTELMAYER, T. Impact of turbulence on the prediction of linear aeroacoustic interactions: Acoustic response of a turbulent shear layer. *J. Sound Vib. 333*, 24 (2014), 6548–6559. (Cited on page 63.)

[63] GLOERFELT, X., BAILLY, C., AND JUVÉ, D. Direct computation of the noise radiated by a subsonic cavity flow and application of integral methods. *J. Sound Vib. 266*, 1 (2003), 119–146. (Cited on page 62.)

[64] GRAF, H., AND ZIADA, S. Excitation source of a side-branch shear layer. *J. Sound Vib. 329*, 14 (2010), 2825–2842. (Cited on pages 6 and 63.)

[65] GUAN, Y., GUPTA, V., AND LI, L. Intermittency route to self-excited chaotic thermoacoustic oscillations. *J. Fluid Mech. 894* (2020). (Cited on page 8.)

[66] GYSLING, D., COPELAND, G., MCCORMICK, D., AND PROSCIA, W. Combustion system damping augmentation with Helmholtz resonators. *J. Eng. Gas Turbines Power 122*, 2 (2000), 269–274. (Cited on page 12.)

[67] HARDING, A.-H., FROST, G., TAN, E., TSUCHIYA, A., MASON, H., ET AL. The cost of hypertension-related ill-health attributable to environmental noise. *Noise and Health 15*, 67 (2013), 437. (Cited on page 1.)

[68] HARRJE, D., AND REARDON, F. Liquid propellant rocket combustion instability. Tech. Rep. SP-194, NASA, 1972. (Cited on pages 2 and 12.)

[69] HERSH, A., WALKER, B., AND CELANO, J. Helmholtz resonator impedance model, part 1: Nonlinear behavior. *AIAA Journal 41*, 5 (2003), 795–808. (Cited on page 44.)

[70] HOFFMANN, N., AND GAUL, L. Effects of damping on mode-coupling instability in friction induced oscillations. *ZAMM Zeitschrift für Angew. Math. und Mech. 83*, 8 (2003), 524–534. (Cited on page 14.)

[71] HOK, G. Response of linear resonant systems to excitation of a frequency varying linearly with time. *J. Appl. Phys. 19*, 3 (1948), 242–250. (Cited on pages 97 and 98.)

[72] HONG, Z., DAI, X., ZHOU, N., SUN, X., AND JING, X. Suppression of Helmholtz resonance using inside acoustic liner. *J. Sound Vib. 333*, 16 (2014), 3585–3597. (Cited on page 62.)

[73] HOWE, M. The dissipation of sound at an edge. *J. Sound Vib. 70*, 3 (1980), 407–411. (Cited on pages 3, 63, and 71.)

[74] HOWE, M. Low strouhal number instabilities of flow over apertures and wall cavities. *J. Acoust. Soc. Am. 102*, 2 (1997), 772–780. (Cited on pages 63 and 67.)

[75] HUGHES, I., AND DOWLING, A. The absorption of sound by perforated linings. *J. Fluid Mech. 218* (1990), 299–335. (Cited on pages 12 and 38.)

[76] ILLINGWORTH, S., MORGANS, A., AND ROWLEY, C. Feedback control of cavity flow oscillations using simple linear models. *J. Fluid Mech. 709* (2012), 223–248. (Cited on page 62.)

[77] IRRETIER, H., AND BALASHOV, D. Transient resonance oscillations of a slow-variant system with small nonlinear damping - modelling and prediction. *J. Sound Vib. 231*, 5 (2000), 1271–1287. (Cited on page 98.)

[78] ISHIKAWA, K., TANIGAWA, R., YATABE, K., OIKAWA, Y., ONUMA, T., AND NIWA, H. Simultaneous imaging of flow and sound using high-speed parallel phase-shifting interferometry. *Opt. Lett. 43*, 5 (2018), 991–994. (Cited on page 64.)

[79] JANG, S.-H., AND IH, J.-G. On the multiple microphone method for measuring in-duct acoustic properties in the presence of mean flow. *J. Acoust. Soc. Am. 103*, 3 (1998), 1520–1526. (Cited on page 53.)

[80] JOSHI, N., MONGIA, H., LEONARD, G., STEGMAIER, J., AND VICKERS, E. Dry low emissions combustor development. In *Proc. ASME Turbo Expo 1998* (1998), p. V003T06A027. (Cited on page 12.)

[81] KACZMARCZYK, S. The passage through resonance in a catenary–vertical cable hoisting system with slowly varying length. *J. Sound Vib. 208*, 2 (1997), 243–269. (Cited on page 98.)

[82] KANDIANIS, F. Frequency response of structures and the effects of noise on its estimates from the transient response. *J. Sound Vib. 15*, 2 (1971), 203–215. (Cited on page 102.)

[83] KARLSSON, M., AND ÅBOM, M. Aeroacoustics of T-junctions − an experimental investigation. *J. Sound Vib. 329*, 10 (2010), 1793–1808. (Cited on pages 63 and 70.)

[84] KATO, T. *Perturbation theory for linear operators*, vol. 132. Springer Science & Business Media, 2013. (Cited on page 34.)

[85] KELLER, J. Thermoacoustic oscillations in combustion chambers of gas turbines. *AIAA Journal 33*, 12 (1995), 2280–2287. (Cited on page 44.)

[86] KELLER, J., AND ZAUNER, E. On the use of Helmholtz resonators as sound attenuators. *ZAMP Zeitschrift für Angew. Math. und Phys. 46*, 3 (1995), 297–327. (Cited on pages 8, 9, 44, 48, and 53.)

[87] KELLER, R. Liquid rocket engine combustion stabilization devices. Tech. Rep. SP-8113, NASA, 1974. (Cited on page 12.)

[88] KEVORKIAN, J. Passage through resonance for a one-dimensional oscillator with slowly varying frequency. *SIAM J. Appl. Math. 20*, 3 (1971), 364–373. (Cited on pages 97 and 98.)

[89] KIGHT, C., AND SWADDLE, J. How and why environmental noise impacts animals: an integrative, mechanistic review. *Ecology letters 14*, 10 (2011), 1052–1061. (Cited on page 1.)

[90] KIM, K., AND HOCHGREB, S. Measurements of triggering and transient growth in a model lean-premixed gas turbine combustor. *Combust. Flame 159*, 3 (2012), 1215–1227. (Cited on page 7.)

[91] KING, J., BOYLE, P., AND OGLE, J. Instability in slotted wall tunnels. *J. Fluid Mech. 4* (1958), 283–305. (Cited on page 3.)

[92] KLAUS, J., BORK, I., GRAF, M., AND OSTERMEYER, G. P. On the adjustment of Helmholtz resonators. *Appl. Acoust. 77* (2014), 37–41. (Cited on pages 12 and 32.)

[93] KOOK, H., AND MONGEAU, L. Analysis of the periodic pressure fluctuations induced by flow over a cavity. *J. Sound Vib. 251*, 5 (2002), 823–846. (Cited on pages 6 and 63.)

[94] KRISHNAMURTY, K. *Sound radiation from surface cutouts in high speed flow.* PhD thesis, California Institute of Technology, 1956. (Cited on page 3.)

[95] KRYLOV, N., AND BOGOLIUBOV, M. M. *Introduction to Non-linear Mechanics.* Izd. Akad. Nauk Ukr. SSR, Kyïv (English translation: Princeton University Press, Princeton, 1947), 1936. (Cited on pages 79 and 87.)

[96] LAHIRI, C., AND BAKE, F. A review of bias flow liners for acoustic damping in gas turbine combustors. *J. Sound Vib. 400* (2017), 564–605. (Cited on page 12.)

[97] LANGRE, E. D. Frequency lock-in is caused by coupled-mode flutter. *J. Fluids Struct. 22*, 6-7 (2006), 783–791. (Cited on page 74.)

[98] LAUDIEN, E., PONGRATZ, R., PIERRO, R., AND PRECLIK, D. Experimental procedures aiding the design of acoustic cavities. *Prog. Astronaut. Aeronaut. 169* (1995), 377–402. (Cited on page 12.)

[99] LEI, S., AND TURAN, A. Nonlinear/chaotic behaviour in thermo-acoustic instability. *Combust. Theor. Model. 13*, 3 (2009), 541–557. (Cited on page 8.)

[100] LEWIS, F. Vibration during acceleration through a critical speed. *Trans. ASME 54*, 3 (1932), 253–261. (Cited on pages 97 and 99.)

[101] LI, D., AND CHENG, L. Acoustically coupled model of an enclosure and a Helmholtz resonator array. *J. Sound Vib. 305*, 1-2 (2007), 272–288. (Cited on page 39.)

[102] Li, D., Cheng, L., Yu, G., and Vipperman, J. Noise control in enclosures: Modeling and experiments with T-shaped acoustic resonators. *J. Acoust. Soc. Am. 122*, 5 (2007), 2615. (Cited on page 27.)

[103] Li, X., Wang, Y., Wang, N., and Zhao, D. Stochastic properties of thermoacoustic oscillations in an annular gas turbine combustion chamber driven by colored noise. *J. Sound Vib.* (2020), 115423. (Cited on page 8.)

[104] Lieuwen, T., and Yang, V. *Combustion instabilities in gas turbine engines: operational experience, fundamental mechanisms, and modeling.* American Institute of Aeronautics and Astronautics, 2005. (Cited on page 2.)

[105] Lieuwen, T. C. Experimental investigation of limit-cycle oscillations in an unstable gas turbine combustor. *J. Propul. Power 18*, 1 (2002), 61–67. (Cited on page 44.)

[106] Lieuwen, T. C. Statistical characteristics of pressure oscillations in a premixed combustor. *J. Sound Vib. 260*, 1 (2003), 3–17. (Cited on page 7.)

[107] Liliedahl, D., Carpenter, F., and Cizmas, P. Prediction of aeroacoustic resonance in cavities of hole-pattern stator seals. *J. Eng. Gas Turbines Power 133*, 2 (2011), 022504. (Cited on page 3.)

[108] Lipatnikov, A., and Sathiah, P. Effects of turbulent flame development on thermoacoustic oscillations. *Combust. Flame 142*, 1-2 (2005), 130–139. (Cited on page 5.)

[109] Ma, R., Slaboch, P., and Morris, S. Fluid mechanics of the flow-excited helmholtz resonator. *J. Fluid Mech. 623* (2009), 1–26. (Cited on page 63.)

[110] Markert, R., and Seidler, M. Analytically based estimation of the maximum amplitude during passage through resonance. *Int. J. Solids Struct. 38*, 10 (2001), 1975–1992. (Cited on pages 98 and 99.)

[111] Martínez-Lera, P., Schram, C., Föller, S., Kaess, R., and Polifke, W. Identification of the aeroacoustic response of a low Mach number flow through a T-joint. *J. Acoust. Soc. Am. 126*, 2 (2009), 582–586. (Cited on page 63.)

[112] Mast, T., and Pierce, A. Describing-function theory for flow excitation of resonators. *J. Acoust. Soc. Am. 97*, 1 (1995), 163–172. (Cited on pages 6 and 63.)

[113] Matsuura, K., and Nakano, M. Disorganization of a hole tone feedback loop by an axisymmetric obstacle on a downstream end plate. *J. Fluid Mech. 757*, 4 (2014), 908–942. (Cited on page 62.)

[114] McManus, K., Poinsot, T., and Candel, S. A review of active control of combustion instabilities. *Prog. Energy Combust. Sci. 19*, 1 (1993), 1–29. (Cited on pages 2 and 5.)

[115] MENSAH, G., MAGRI, L., SILVA, C., BUSCHMANN, P., AND MOECK, J. Exceptional points in the thermoacoustic spectrum. *J. Sound Vib. 433* (2018), 124–128. (Cited on pages 5 and 14.)

[116] MENSAH, G., AND MOECK, J. Acoustic damper placement and tuning for annular combustors: An adjoint-based optimization study. *J. Eng. Gas Turbines Power 139*, 6 (2017), 061501. (Cited on pages 13 and 44.)

[117] MIKHLIN, S. *Variational methods in mathematical physics*, vol. 50. Pergamon Press, distributed by Macmillan, New York, 1964. (Cited on page 4.)

[118] MOHAMAD, M., AND SAPSIS, T. Probabilistic description of extreme events in intermittently unstable dynamical systems excited by correlated stochastic processes. *SIAM/ASA J. Uncertainty Quantif. 3*, 1 (2015), 709–736. (Cited on pages 8, 64, and 83.)

[119] MOHANY, A., ARTHURS, D., BOLDUC, M., HASSAN, M., AND ZIADA, S. Numerical and experimental investigation of flow-acoustic resonance of side-by-side cylinders in a duct. *J. Fluids Struct. 48* (2014), 316–331. (Cited on page 74.)

[120] MONGIA, H., HELD, T., HSIAO, G., AND PANDALAI, R. Challenges and progress in controlling dynamics in gas turbine combustors. *J. Propuls. Power 19*, 5 (2003), 822–829. (Cited on page 12.)

[121] MORRIS, S. Shear-layer instabilities: Particle image velocimetry measurements and implications for acoustics. *Annu. Rev. Fluid Mech. 43* (2011), 529–550. (Cited on page 66.)

[122] MORSE, P., AND INGARD, K. *Theoretical acoustics*. Princeton university press, 1968. (Cited on pages 1, 4, 15, 16, 22, and 39.)

[123] MUKHERJEE, N., AND SHRIRA, V. Intrinsic flame instabilities in combustors: analytic description of a 1-D resonator model. *Combust. Flame 185* (2017), 188–209. (Cited on page 5.)

[124] NAIR, V., THAMPI, G., AND SUJITH, R. Intermittency route to thermoacoustic instability in turbulent combustors. *J. Fluid Mech. 756* (2014), 470–487. (Cited on page 64.)

[125] NAUDASCHER, E., AND ROCKWELL, D. Oscillator-model approach to the identification and assessment of flow-induced vibrations in a system. *J. Hydraul. Res. 18*, 1 (1980), 59–82. (Cited on page 2.)

[126] NELSON, P., HALLIWELL, N., AND DOAK, P. Fluid dynamics of a flow excited resonance, Part II: Flow acoustic interaction. *J. Sound Vib. 91*, 3 (1983), 375–402. (Cited on page 63.)

[127] NICOUD, F., BENOIT, L., SENSIAU, C., AND POINSOT, T. Acoustic modes in combustors with complex impedances and multidimensional active flames. *AIAA Journal 45*, 2 (2007), 426–441. (Cited on page 18.)

[128] NOBLE, A., KING, G., LAURENDEAU, N., GORD, J., AND ROY, S. Nonlinear thermoacoustic instability dynamics in a Rijke tube. *Combust. Sci. Technol. 184*, 3 (2012), 293–322. (Cited on page 8.)

[129] NOIRAY, N. Linear growth rate estimation from dynamics and statistics of acoustic signal envelope in turbulent combustors. *J. Eng. Gas Turbines Power 139*, 4 (2017), 041503. (Cited on pages 7 and 88.)

[130] NOIRAY, N., AND DENISOV, A. A method to identify thermoacoustic growth rates in combustion chambers from dynamic pressure time series. *Proc. Combust. Inst. 36*, 3 (2017), 3843–3850. (Cited on page 46.)

[131] NOIRAY, N., DUROX, D., SCHULLER, T., AND CANDEL, S. A unified framework for nonlinear combustion instability analysis based on the flame describing function. *J. Fluid Mech. 615* (2008), 139–167. (Cited on pages 7 and 76.)

[132] NOIRAY, N., AND SCHUERMANS, B. Theoretical and experimental investigations on damper performance for suppression of thermoacoustic oscillations. *J. Sound Vib. 331*, 12 (2012), 2753–2763. (Cited on pages 13, 23, 28, 29, 39, 40, and 44.)

[133] NOIRAY, N., AND SCHUERMANS, B. Deterministic quantities characterizing noise driven Hopf bifurcations in gas turbine combustors. *Int. J. Non Linear Mech. 50* (2013), 152–163. (Cited on pages 23, 25, and 55.)

[134] OSCHWALD, M., FARAGO, Z., SEARBY, G., AND CHEURET, F. Resonance frequencies and damping of a combustor acoustically coupled to an absorber. *J. Propuls. Power 24*, 3 (2008), 524–533. (Cited on page 12.)

[135] OSCHWALD, M., AND MARPERT, M. On the acoustics of rocket combustors equipped with quarter wave absorbers. *Prog. Propuls. Phys. 2* (2011), 339 – 350. (Cited on page 12.)

[136] PARK, I., AND SOHN, C. Nonlinear acoustic damping induced by a half-wave resonator in an acoustic chamber. *Aerosp. Sci. Technol. 14*, 6 (2010), 442–450. (Cited on page 44.)

[137] PARK, S., AND SEO, S. Low-frequency noise reduction in an enclosure by using a Helmholtz resonator array. *Trans. Korean Soc. Noise Vib. Eng. 22*, 8 (2012), 756–762. (Cited on pages 12 and 27.)

[138] PARK, Y., DO, Y., AND LOPEZ, J. Slow passage through resonance. *Phys. Rev. E 84*, 5 (2011), 056604. (Cited on pages 98 and 99.)

[139] PAWLACZYK-ŁUSZCZYŃSKA, M., DUDAREWICZ, A., WASZKOWSKA, M., AND ŚLIWIŃSKA-KOWALSKA, M. Assessment of annoyance from low frequency and

broadband noises. *Int. J. Occup. Environ. Med. 16* (2003), 337–43. (Cited on page 1.)

[140] PETERS, M., AND HOEIJEMAKERS, H. A vortex sheet method applied to unsteady flow separation from sharp edges. *J. Comput. Phys. 120*, 1 (1995), 88–104. (Cited on page 63.)

[141] PIETRZKO, S., AND MAO, Q. New results in active and passive control of sound transmission through double wall structures. *Aerosp. Sci. Technol. 12*, 1 (2008), 42–53. (Cited on pages 12 and 27.)

[142] PIRRERA, S., DE VALCK, E., AND CLUYDTS, R. Nocturnal road traffic noise: A review on its assessment and consequences on sleep and health. *Environ. Int. 36*, 5 (2010), 492–498. (Cited on page 1.)

[143] PUTNAM, A. *Combustion driven oscillations in industry.* Elsevier, 1971. (Cited on page 38.)

[144] RAUSCH, V., BAUCH, E., AND BUNZECK, N. White noise improves learning by modulating activity in dopaminergic midbrain regions and right superior temporal sulcus. *J. Cogn. Neurosci. 26*, 7 (2014), 1469–1480. (Cited on page 1.)

[145] RAYLEIGH, J. *The theory of sound. vol. 2*, vol. II. MacMillan and Co., London, 1878. (Cited on page 2.)

[146] REED III, W., HALL, A., AND BARKER JR, L. Analog techniques for measuring the frequency response of linear physical systems excited by frequency-sweep inputs. Tech. rep., NASA Langley Research Center, 1960. (Cited on page 97.)

[147] REES, E. L. Graphical discussion of the roots of a quartic equation. *Am. Math. Mon. 29*, 2 (1922), 51–55. (Cited on page 32.)

[148] RICHARDS, G., STRAUB, D., AND ROBEY, E. Passive control of combustion dynamics in stationary gas turbines. *J. Propuls. Power 19*, 5 (2003), 795–810. (Cited on page 12.)

[149] RIENSTRA, S., AND HIRSCHBERG, A. An Introduction to Acoustics. *Eindhoven University of Technology* (2004). (Cited on page 15.)

[150] ROCKWELL, D., AND NAUDASCHER, E. Self-sustaining oscillations of flow past cavities. *J. Fluids Eng., Trans. ASME 100*, 2 (1978), 152–165. (Cited on page 62.)

[151] RONNEBERGER, D. The acoustical impedance of holes in the wall of flow ducts. *J. Sound Vib. 24*, 1 (1972), 133–150. (Cited on page 6.)

[152] ROSSITER, J. Wind tunnel experiments on the flow over rectangular cavities at subsonic and transonic speeds. Tech. Rep. 3438, Royal Aircraft Establishment, Aeronautical Research Council Reports and Memoranda No., 1964. (Cited on pages 3 and 62.)

[153] ROWLEY, C., COLONIUS, T., AND BASU, A. On self-sustained oscillations in two-dimensional compressible flow over rectangular cavities. *J. Fluid Mech. 455* (2002), 315–346. (Cited on page 62.)

[154] ROWLEY, C., AND WILLIAMS, D. Dynamics and control of high-Reynolds-number flow over open cavities. *Annu. Rev. Fluid Mech. 38*, 1 (2006), 251–276. (Cited on pages 3 and 62.)

[155] RYU, J., SON, W., HWANG, D., LEE, S., AND KIM, S. Exceptional points in coupled dissipative dynamical systems. *Phys. Rev. E 91*, 5 (2015), 052910. (Cited on pages 14 and 31.)

[156] SCARPATO, A., DUCRUIX, S., AND SCHULLER, T. Optimal and off-design operations of acoustic dampers using perforated plates backed by a cavity. *J. Sound Vib. 332*, 20 (2013), 4856–4875. (Cited on page 38.)

[157] SCARPATO, A., TRAN, N., DUCRUIX, S., AND SCHULLER, T. Modeling the damping properties of perforated screens traversed by a bias flow and backed by a cavity at low Strouhal number. *J. Sound Vib. 331*, 2 (2012), 276–290. (Cited on page 19.)

[158] SCHLEIN, B., ANDERSON, D., BEUKENBERG, M., MOHR, K., LEINER, H., AND TRÄPTAU, W. Development history and field experiences of the first FT8 gas turbine with dry low NOx combustion system. In *Proc. ASME Turbo Expo 1999* (1999), p. V002T02A039. (Cited on page 12.)

[159] SCHUERMANS, B., BELLUCCI, V., GUETHE, F., MEILI, F., FLOHR, P., AND PASCHEREIT, C. O. A detailed analysis of thermoacoustic interaction mechanisms in a turbulent premixed flame. In *Proc. ASME Turbo Expo 2004* (2004), vol. 1, pp. 539–551. (Cited on pages 19 and 69.)

[160] SCHULLER, T., DUROX, D., AND CANDEL, S. A unified model for the prediction of laminar flame transfer functions: comparisons between conical and v-flame dynamics. *Combust. Flame 134*, 1-2 (2003), 21–34. (Cited on page 5.)

[161] SCHULLER, T., POINSOT, T., AND CANDEL, S. Dynamics and control of premixed combustion systems based on flame transfer and describing functions. *J. Fluid. Mech. 894* (2020). (Cited on page 5.)

[162] SCHULZE, M., KATHAN, R., AND SATTELMAYER, T. Impact of Absorber Ring Position and Cavity Length on Acoustic Damping. *J. Spacecr. Rockets 52 (3)*, 3 (2015), 917–927. (Cited on page 12.)

[163] SEARBY, G., HABIBALLAH, M., NICOLE, A., AND LAROCHE, E. Prediction of the efficiency of acoustic damping cavities. *J. Propuls. Power 24*, 3 (2008), 516–523. (Cited on page 16.)

[164] Seyranian, A., and Mailybaev, A. *Multiparameter stability theory with mechanical applications*, vol. 13. World Scientific, 2003. (Cited on page 34.)

[165] Seyranian, A. P., Kirillov, O. N., and Mailybaev, A. A. Coupling of eigenvalues of complex matrices at diabolic and exceptional points. *J. Phys. A. Math. Gen. 38*, 8 (2005), 1723–1740. (Cited on page 31.)

[166] Shaaban, M., and Mohany, A. Passive control of flow-excited acoustic resonance in rectangular cavities using upstream mounted blocks. *Exp. Fluids 56* (2015), 72. (Cited on page 3.)

[167] Shi, C., Dubois, M., Chen, Y., Cheng, L., Ramezani, H., Wang, Y., and Zhang, X. Accessing the exceptional points of parity-time symmetric acoustics. *Nat. Commun. 7* (2016), 11110. (Cited on page 14.)

[168] Shoshani, O. Deterministic and stochastic analyses of the lock-in phenomenon in vortex-induced vibrations. *J. Sound Vib. 434* (2018), 17–27. (Cited on page 74.)

[169] Singh, D., and Rienstra, S. Nonlinear asymptotic impedance model for a Helmholtz resonator liner. *J. Sound Vib. 333*, 15 (2014), 3536–3549. (Cited on page 44.)

[170] Singh, N., and Davar, S. Noise pollution-sources, effects and control. *J. Human Ecol. 16*, 3 (2004), 181–187. (Cited on page 1.)

[171] Söderlund, G., Sikström, S., Loftesnes, J., and Sonuga-Barke, E. The effects of background white noise on memory performance in inattentive school children. *Behav. Brain Funct. 6*, 1 (2010), 55. (Cited on page 1.)

[172] Sohn, C., and Park, J. A comparative study on acoustic damping induced by half-wave, quarter-wave, and Helmholtz resonators. *Aerosp. Sci. Technol. 15*, 8 (2011), 606–614. (Cited on page 12.)

[173] Stansfeld, S., and Matheson, M. Noise pollution: non-auditory effects on health. *British Medical Bulletin 68*, 1 (2003), 243–257. (Cited on page 1.)

[174] Stow, S., and Dowling, A. Low-order modelling of thermoacoustic limit cycles. *ASME Paper No. GT2004-54245* (2004). (Cited on page 44.)

[175] Stow, S., and Dowling, A. A time-domain network model for nonlinear thermoacoustic oscillations. In *ASME Turbo Expo 2008: Power for Land, Sea, and Air* (2008), American Society of Mechanical Engineers, pp. 539–551. (Cited on page 44.)

[176] Stratonovich, R. *Topics in the theory of random noise*, vol. 2. CRC Press, 1967. (Cited on pages 48 and 87.)

[177] Su, J., Rupp, J., Garmory, A., and Carrotte, J. Measurements and computational fluid dynamics predictions of the acoustic impedance of orifices. *J. Sound Vib. 352* (2015), 174–191. (Cited on pages 4 and 6.)

[178] Sun, Y., Taira, K., Cattafesta, L., and Ukeiley, L. Biglobal instabilities of compressible open-cavity flows. *J. Fluid Mech. 826* (2017), 270–301. (Cited on page 62.)

[179] Sung, L., and Stevens, K. Response of linear discrete and continuous systems to variable frequency sinusoidal excitations. *J. Sound Vib. 71*, 4 (1980), 497–509. (Cited on pages 98 and 99.)

[180] Tam, C., and Block, P. On the tones and pressure oscillations induced by flow over rectangular cavities. *J. Fluid Mech. 89*, 2 (1978), 373–399. (Cited on page 3.)

[181] Tam, C., Kurbatskii, K., Ahuja, K., and Gaeta, R. A numerical and experimental investigation of the dissipation mechanisms of resonant acoustic liners. *J. Sound Vib. 245*, 3 (2001), 545–557. (Cited on pages 4, 15, and 44.)

[182] Terrien, S., Vergez, C., and Fabre, B. Flute-like musical instruments: A toy model investigated through numerical continuation. *J. Sound Vib. 332*, 15 (2013), 3833–3848. (Cited on page 63.)

[183] Tonon, D., Hirschberg, A., Golliard, J., and Ziada, S. Aeroacoustics of pipe systems with closed branches. *Int. J. Aeroacoust. 10*, 2-3 (2011), 201–275. (Cited on page 62.)

[184] Tonon, D., Willems, J., and Hirschberg, A. Self-sustained oscillations in pipe systems with multiple deep side branches: Prediction and reduction by detuning. *J. Sound Vib. 330*, 24 (2011), 5894–5912. (Cited on page 62.)

[185] Torvik, P. On estimating system damping from frequency response bandwidths. *J. Sound Vib. 330*, 25 (2011), 6088–6097. (Cited on pages 98 and 99.)

[186] Tournadre, J., Förner, K., Martínez-Lera, P., Polifke, W., and Desmet, W. Determination of Acoustic Impedance for Helmholtz Resonators Through Incompressible Unsteady Flow Simulations. *22nd AIAA/CEAS Aeroacoustics Conf.* (2016). (Cited on page 44.)

[187] Verge, M., Hirschberg, A., and Caussé, R. Sound production in recorder-like instruments. ii. a simulation model. *J. Acoust. Soc. Am. 101*, 5 I (1997), 2925–2939. (Cited on page 63.)

[188] Wang, P., He, L., and Liu, Y. Acoustics-driven vortex dynamics in channel branches with round intersections: Flow mode transition and three-dimensionality. *Phys. Fluids 32*, 2 (2020). (Cited on page 62.)

[189] Weaver, D., and Ainsworth, P. Flow-induced vibrations in bellows. *J. Pressure Vessel Technol. 111*, 4 (1989), 402–406. (Cited on page 3.)

[190] White, R. Evaluation of the dynamic characteristics of structures by transient testing. *J. Sound Vib. 15*, 2 (1971), 147–161. (Cited on page 98.)

[191] Xiong, L., Nennig, B., Aurégan, Y., and Bi, W. Sound attenuation optimisation using metaporous materials tuned on exceptional points. *J. Acoust. Soc. Am. 142*, 4 (2017), 2288–2297. (Cited on page 14.)

[192] Yamouni, S., Sipp, D., and Jacquin, L. Interaction between feedback aeroacoustic and acoustic resonance mechanisms in a cavity flow: a global stability analysis. *J. Fluid Mech. 717* (2013), 134–165. (Cited on page 62.)

[193] Yang, D., and Morgans, A. A semi-analytical model for the acoustic impedance of finite length circular holes with mean flow. *J. Sound Vib. 384* (2016), 294–311. (Cited on pages 4, 6, and 15.)

[194] Yang, D., and Morgans, A. Acoustic models for cooled helmholtz resonators. *AIAA Journal 55*, 9 (2017), 3120–3127. (Cited on pages 13 and 44.)

[195] Yang, D., and Morgans, A. The acoustics of short circular holes opening to confined and unconfined spaces. *J. Sound Vib. 393* (2017), 41–61. (Cited on pages 4 and 6.)

[196] Yokoyama, H., and Kato, C. Fluid-acoustic interactions in self-sustained oscillations in turbulent cavity flows. i. fluid-dynamic oscillations. *Phys. Fluids 21*, 10 (2009). (Cited on page 62.)

[197] Yu, G., and Cheng, L. Location optimization of a long T-shaped acoustic resonator array in noise control of enclosures. *J. Sound Vib. 328*, 1-2 (2009), 42–56. (Cited on page 12.)

[198] Yu, G., Li, D., and Cheng, L. Effect of internal resistance of a Helmholtz resonator on acoustic energy reduction in enclosures. *J. Acoust. Soc. Am. 124*, 6 (2008), 3534–3543. (Cited on pages 12 and 27.)

[199] Zahn, M., Betz, M., Wagner, M., Stadlmair, N., Schulze, M., Hirsch, C., and Sattelmayer, T. Impact of Damper Parameters on the Stability Margin of an Annular Combustor Test Rig. In *Proc. ASME Turbo Expo 2017* (2017), p. V04BT04A001. (Cited on pages 12 and 44.)

[200] Zahn, M., Schulze, M., Hirsch, C., and Sattelmayer, T. Impact of quarter-wave tube arrangement on damping of azimuthal modes. In *Proc. ASME Turbo Expo 2016* (2016), p. V04AT04A025. (Cited on page 12.)

[201] Zalluhoglu, U., and Olgac, N. Analytical and Experimental Study on Passive Stabilization of Thermoacoustic Dynamics in a Rijke Tube. *J. Dyn. Syst. Meas. Control 140*, 2 (2017), 021007. (Cited on page 12.)

[202] ZHAO, D., AND LI, X. A review of acoustic dampers applied to combustion chambers in aerospace industry. *Prog. Aerosp. Sci. 74* (2015), 114–130. (Cited on pages 2, 12, and 44.)

[203] ZHONG, Z., AND ZHAO, D. Time-domain characterization of the acoustic damping of a perforated liner with bias flow. *J. Acoust. Soc. Am. 132*, 1 (2012), 271–281. (Cited on page 13.)

[204] ZHU, X., RAMEZANI, H., SHI, C., ZHU, J., AND ZHANG, X. PT-symmetric acoustics. *Phys. Rev. X 4*, 3 (2014), 031042. (Cited on page 14.)

[205] ZIADA, S. A flow visualization study of flow-acoustic coupling at the mouth of a resonant side-branch. *J. Fluids Struct. 8*, 4 (1994), 391–416. (Cited on page 8.)

[206] ZIADA, S. Flow-excited acoustic resonance in industry. *J. Pressure Vessel Technol. 132*, 1 (2010), 015001. (Cited on page 3.)

[207] ZIADA, S., AND LAFON, P. Flow-excited acoustic resonance excitation mechanism, design guidelines, and counter measures. *Applied Mech. Rev. 66* (2014), 010802. (Cited on page 62.)

[208] ZINN, B. A theoretical study of non-linear damping by Helmholtz resonators. *J. Sound Vib. 13*, 3 (1970), 347–356. (Cited on pages 8, 9, 44, 48, and 53.)